INFORMATION TO USERS

This manuscript has been reproduced from the microfilm master. UMI films the text directly from the original or copy submitted. Thus, some thesis and dissertation copies are in typewriter face, while others may be from any type of computer printer.

The quality of this reproduction is dependent upon the quality of the copy submitted. Broken or indistinct print, colored or poor quality illustrations and photographs, print bleedthrough, substandard margins, and improper alignment can adversely affect reproduction.

In the unlikely event that the author did not send UMI a complete manuscript and there are missing pages, these will be noted. Also, if unauthorized copyright material had to be removed, a note will indicate the deletion.

Oversize materials (e.g., maps, drawings, charts) are reproduced by sectioning the original, beginning at the upper left-hand corner and continuing from left to right in equal sections with small overlaps. Each original is also photographed in one exposure and is included in reduced form at the back of the book.

Photographs included in the original manuscript have been reproduced xerographically in this copy. Higher quality 6" x 9" black and white photographic prints are available for any photographs or illustrations appearing in this copy for an additional charge. Contact UMI directly to order.

UMI®

Bell & Howell Information and Learning
300 North Zeeb Road, Ann Arbor, MI 48106-1346 USA
800-521-0600

Toward a Measurement of Atomic Parity Nonconservation Using a Single, Trapped Barium Ion

Kristi R. G. Hendrickson

A dissertation submitted in partial fulfillment of
the requirements for the degree of

Doctor of Philosophy

University of Washington

1999

Program Authorized to Offer Degree: Physics Department

In presenting this dissertation in partial fulfillment of the requirements for the Doctoral degree at the University of Washington, I agree that the Library shall make its copies freely available for inspection. I further agree that extensive copying of this dissertation is allowable only for scholarly purposes, consistent with "fair use" as prescribed in the U.S. Copyright Law.

Requests for copying or reproduction of this dissertation may be referred to University Microfilms, 1490 Eisenhower Place, P.O. Box 975, Ann Arbor, MI 48106, to whom the author has granted "the right to reproduce and sell (a) copies of the manuscript in microform and/or (b) printed copies of the manuscript made from microform."

Signature Christi Hendrickson

Date 13 August 1999

University of Washington
Graduate School

This is to certify that I have examined this copy of a doctoral dissertation by

Kristi R. G. Hendrickson

and have found that it is complete and satisfactory in all respects,
and that any and all revisions required by the final
examining committee have been made.

Chair of Supervisory Committee:

E. Norval Fortson

Reading Committee:

Warren Nagourney

Ann E. Nelson

Date: 8/13/99

University of Washington

Abstract

Toward a Measurement of Atomic Parity Nonconservation Using a Single, Trapped Barium Ion

by Kristi R. G. Hendrickson

Chair of Supervisory Committee

Professor E. Norval Fortson
Physics

A single, trapped barium ion presents an excellent opportunity to make a precise atomic parity nonconservation measurement. The relatively perturbation-free single-ion trapping environment and high efficiency shelving techniques can in principle be used to achieve an experimental precision at the 0.3% level or better. This accuracy range would permit us to make statements about the existence of new physics beyond the Standard Model. The weak interaction in Ba^+ modifies the light shift induced in the ground state by an intense laser beam, adding a parity-violating contribution to the Larmor precession frequency of the electron spin in the Ba^+ ground state. This thesis presents and describes the apparatus and techniques for completing the intended measurement and also presents the results of several, successful, preliminary measurements using this system.

TABLE OF CONTENTS

List of Figures vi

List of Tables x

Chapter 1: Introduction 1

1.1 First suggestions and observations of parity nonconservation in Nature 3
1.2 Atomic experiments as tests for parity nonconservation in the weak interaction 4
1.3 Weak-interaction information from atomic parity-nonconserving observables 5
1.4 Radiative corrections and new tree-level physics 6
  1.4.1 Radiative corrections 7
  1.4.2 Direct exchange of new particles 10
1.5 Atomic PNC experiments 10
  1.5.1 Recent atomic experiments 10
  1.5.2 General remarks 13
1.6 Isotope comparisons 13
1.7 Atomic and high-energy electroweak data 15
  1.7.1 Current analysis of electroweak data 17
  1.7.2 Evidence for the direct exchange of new particles 18
  1.7.3 New physics suggested by the 1999 Cs result 19

1.8 Concluding remarks 20

Chapter 2: A trapped barium ion and atomic parity nonconservation 23

2.1 Why use ion traps? 23
2.2 Why use barium? 25
  2.2.1 Heavy atom 26
  2.2.2 Trappable ion 27
  2.2.3 Available light sources 27
  2.2.4 Atomic theory 27
  2.2.5 Isotopic comparisons 28
  2.2.6 Nuclear uncertainties 28
2.3 Inherent statistical accuracy 29
2.4 Concluding remarks 31

Chapter 3: Electroweak theory in the barium ion 32

3.1 Z^0 and the neutral current 32
3.2 Atomic parity-nonconserving Hamiltonian 34
3.3 Parity-mixed atomic states 37
3.4 Parity-induced electric-dipole amplitude 38
3.5 PNC observable in Ba$^+$ 40
  3.5.1 The shift 41
  3.5.2 Larmor precession 44
  3.5.3 Size of the effect 45
  3.5.4 The measurement 47
3.6 Concluding remarks 49

Chapter 4: Apparatus **50**

4.1 The trap 50

4.2 Laser cooling 57

4.3 Ion signal 60

4.3.1 Light-collection system: physical description 60

4.3.2 Electronics modules 63

4.3.3 Alignment procedures 63

4.3.4 Possible improvements 65

4.4 Trapping systems 65

4.4.1 Classic system 65

4.4.2 System 97 73

4.4.3 Vacuum preparation 75

4.4.4 The trap voltage 78

4.5 Trapping elements 80

4.5.1 Ovens 81

4.5.2 Filaments 82

4.5.3 Compensation plates 82

4.6 Magnetic shielding 83

4.7 The lasers 83

4.7.1 Light sources 84

4.7.2 Laser locking 91

4.8 Focusing optics system 93

4.9 Computer control 94

Chapter 5: Systematics **96**

5.1 Fake PNC effects 96
5.1.1 Dipole field effects 97
5.1.2 Quadrupole field effects 98
5.1.3 Quadrupole-quadrupole field effects 98
5.2 Decoherence effects 101
5.3 Magnetic field problems 103
5.4 Concluding remarks 103

Chapter 6: Experiments and techniques **104**

6.1 Shelving 105
6.2 Shelving probability and branching fractions 107
6.3 Lifetime experiments 113
6.3.1 Lifetime of the $5D_{5/2}$ metastable state 115
6.3.2 Lifetime of the $5D_{3/2}$ state 124
6.3.3 Lifetime of the $6S_{1/2}$ state 126
6.4 2-μm quadrupole transition 130
6.5 Measurements in progress 134
6.5.1 Magnetic sublevel state selection 134
6.5.2 Magnetic resonance experiments 135
6.5.3 Spin state lifetimes 136
6.5.4 Light shifts 136
6.5.5 Standing-wave system 137

Chapter 7: Conclusions **138**

Bibliography **139**

Appendix A: Schematics 150

LIST OF FIGURES

1.1 Feynman diagram of possible radiative corrections. 7

1.2 Feynman diagrams of possible new tree-level interactions. 9

1.3 Allowed ranges of S and T. 16

1.4 Plot illustrating the different sensitivities of high-energy and atomic experiments to a hypothetical new Z′. 18

3.1 Feynman diagram of the exchange of the Z^0. 33

3.2 Ba^+ energy-level diagram with parity-mixed ground state. 39

3.3 Diagram distinguishing between the pure quadrupole and PNC-induced light shifts. 44

3.4 Sketch of the standing-wave field pattern for the PNC measurement. . 46

3.5 Diagram showing the level splitting due to PNC added to that due to the applied external magnetic field of $\sim 10^{-4}$ Gauss. 47

3.6 Measurement sequence used to determine the PNC light shift. 48

4.1 Photograph of the experimental apparatus. 51

4.2 Hyperbolic electrode structure of the Paul trap. 52

4.3 Calculated ion trajectory in a Paul trap. 53

4.4 Sketch of a twisted-wire trap. 56

4.5 Energy-level diagram for Ba^+ showing the cooling cycle. 59

4.6 Real-time read out of photons/s scattered by a trapped ion exposed to blue (493-nm) and red (650-nm) radiation as it cycles among the $6S_{1/2} \leftrightarrow 6P_{1/2} \leftrightarrow 5D_{3/2}$ levels. 61
4.7 Sketch of the light-collection system 62
4.8 Classic system main chamber design. 67
4.9 Photograph of the Classic trap header. 68
4.10 Beam arrangement diagram for the Classic system. 69
4.11 Sketch of the trap assembly. 71
4.12 Sketch of the mirror holder assembly. 72
4.13 Mechanical sketch of the modified six-way cross vacuum chamber. . . 74
4.14 Beam arrangement in System 97. 76
4.15 Proposed mirror assembly for System 97. 76
4.16 Pi network circuit used to step up the trap voltage. 79
4.17 Tapped coil step-up trap circuit. 80
4.18 Schematic of the frequency-doubling cavity. 85
4.19 Sketch of the 2-μm laser. 88
4.20 Pumping diagram for the 2-μm laser. 89
4.21 Energy-level diagram for Ba^+ showing shelving and deshelving transitions. 90

5.1 Energy-level diagram of Ba^+ showing the energy shifts of the $6S_{1/2}$ and $5D_{3/2}$ levels due to nonresonant dipole effects caused by the PNC electric field. 100
5.2 Decrease of the lifetime of the $5D_{3/2}$ due to nonresonant dipole coupling. 102

6.1 Ba$^+$ energy-level diagrams indicating the difference in scattered blue light when the ion is shelved. 105
6.2 Allowed transitions during shelving and deshelving. 106
6.3 Indirect shelving transitions. 107
6.4 Measurement cycle used to determine the branching fractions and hence the shelving efficiency of the indirect shelving method. 109
6.5 Shelving probability data with the red laser blocked during shelving. . 111
6.6 Measurement cycle used to determine the lifetime of the $5D_{5/2}$ metastable state. 115
6.7 Histogram of the data used to determine the lifetime of the $5D_{5/2}$ state. 116
6.8 Log plot of the data used to determine the lifetime of the $5D_{5/2}$ state. 116
6.9 Energy-level diagram showing the allowed process in the decay of the $5D_{5/2}$ state. 117
6.10 Processes possibly involved in shortening the lifetime of the $5D_{5/2}$ state. 119
6.11 Measurement sequence used to explore resonant and nonresonant coupling effects on the lifetime of the $5D_{5/2}$ state. 120
6.12 Plot of the effects of the red laser that shortens the lifetime of the $5D_{5/2}$ state. 120
6.13 Plot of 1 - the detection probability versus the wait time interval used to determine the effects of the red and blue lasers on the lifetime of the $5D_{5/2}$ state. 122
6.14 Final measurement sequence for the $5D_{5/2}$ lifetime. 123
6.15 Measurement cycle for determining the $5D_{3/2}$ lifetime. 124
6.16 $5D_{3/2}$ lifetime-altering effects due to leaking resonant light. 125

6.17 Measurement cycle to explore the effect on the $5D_{3/2}$ lifetime due to resonant light leaking into the system. 126
6.18 Normalized plot of $5D_{3/2}$ lifetime data. 127
6.19 Measurement cycle used to explore the ground-state lifetime. 128
6.20 Processes affecting measurement of the ground-state lifetime. 128
6.21 Shelving probability versus the wait time interval used to explore the ground-state lifetime. 129
6.22 Process of driving the quadrupole transition. 130
6.23 Measurement cycle used to determine the 2-μm quadrupole transition rate. 131
6.24 Shelving probability data used to see the quadrupole transition. . . . 132
6.25 Cumulative shelving probability data for various wait time intervals used to determine the quadrupole transition rate. 133

A.1 Circuit schematic of the bipolar current supply for the magnetic field coils. 151
A.2 Circuit schematic of the 2-μm pump and red laser controllers. 152

LIST OF TABLES

1.1 Recent atomic PNC experimental and theoretical precisions. 11

1.2 Electroweak observables used in the fit in Figure 1.3. 22

2.1 Comparison of the enhancement factors of heavy atoms used in atomic PNC experiments. 26

2.2 Stable and long-lived isotopes of barium. 29

2.3 Comparison of the statistical power of various atomic PNC experiments. 30

6.1 Data used to determine the branching ratio $f_{D_{3/2}}/f_{D_{5/2}}$. 112

6.2 Table of determinations of the lifetime of the $5D_{5/2}$ state. 118

6.3 Table of data used to determine how the lifetime of the $5D_{5/2}$ state is affected by the red and blue laser light. 121

ACKNOWLEDGMENTS

The author wishes to express sincere appreciation to Michael Schacht, Norval Fortson, Warren Nagourney, Steve Lamoreaux, Steve Parker, Bruce Warrington, Roy B. Pettus, Jr., Ann Nelson, Blayne Heckel, Xin Xin Zhao, Nan Yu, Diane Markoff, Alex Cronin, Reina Maruyama, Amar Andalkar, Justin Torgerson, Mike Romalis, Bob Morley, John Rose, Ron Musgrave, Tiku Majumder, and Barium.

DEDICATION

This Ph.D. thesis is dedicated to my mother.

Chapter 1

INTRODUCTION

Parity nonconservation (PNC) in atoms arises from the exchange of the Z^0 boson between atomic electrons and quarks in the nucleus. Precise measurement of atomic PNC can provide an exacting test of electroweak theory complementary to information from high-energy accelerators. The most recent measurements probe for certain kinds of new physics more precisely than any other experiment. One possible new step would be to measure PNC in a single ion such as Ba^+ with a well understood atomic structure permitting exact comparison of the results with particle theory.

The work presented in this thesis is the first step toward a precision PNC measurement in a single, trapped ion. The conclusion of this first step includes proof in practice of several key steps necessary for the success of this technically challenging precision experiment. First, we report the first successful barium ion trap using completely solid-state laser systems. Second, we describe the success of the developed methods and techniques for polarizing, manipulating, and analyzing the trapped barium ion in general and its spin direction in particular. Third, we report the first direct observation of the 2-μm quadrupole transition in Ba^+. Fourth, we report preliminary success in observing and measuring Zeeman transitions in the ground and excited states.

Following these successes, a few major questions vital to a precision PNC measurement in Ba^+ remain to be answered. The first iteration of the system that will produce a stable standing-wave pattern needed to drive the PNC and quadrupole transitions has been designed and constructed but not tested completely. The refinement and control of the standing-wave optics needed for an accurate PNC measurement will present a formidable challenge. The 2-μm laser used in the experiments presented in this and the next ([Sch00]) thesis appears to have insufficient power and stability for the PNC measurement. It is not yet clear if mere alterations to the existing laser will solve all of these problems. A different 2-μm laser system may be necessary, and there exists a constant vigilance to identify new 2-μm laser technology. It is encouraging that the frequency stability of a few kHz needed for a PNC measurement has been achieved at 2 μm with existing technology. A stable and small applied magnetic field is needed to produce a small Zeeman splitting that adds to the PNC-induced splitting between the ground-state magnetic sublevels, which requires shielding from ambient magnetic fields. The level of magnetic shielding that the final measurement requires was not necessary for any of the measurements presented in this thesis and therefore was not designed or built. The level of magnetic shielding ultimately required is high but not extreme and is achievable with known materials and strategies.

In the following chapters I discuss the history, background, and motivation for this measurement of the weak interaction in a single, trapped barium ion. I outline the electroweak theory that pertains to the measurement. I describe fully the apparatus and experimental methods used to interrogate Ba^+ and present a series of measurements with analysis that establish many of the techniques required for the PNC measurement and that determine interesting atomic data. I discuss the major anticipated systematic difficulties and suggest how these problems can be reduced or eliminated. I conclude with a discussion of the work remaining to complete the PNC measurement in Ba^+.

1.1 First suggestions and observations of parity nonconservation in Nature

During the mid-1950s, particle physicists were pondering the "$\tau - \theta$" puzzle; the neutral K meson was observed to decay via two separate channels, one leading to two π mesons and the other leading to three π mesons as the decay products. Each π meson was known to possess odd parity, and the composite particle was inferred to have the parity of its parts and their relative angular momentum. It seemed apparent that there were two neutral K meson particles with nearly identical masses and lifetimes and opposite parities, although it might be more "natural" to say that a single particle was being observed. But to claim that a single neutral K meson existed was also to claim that parity was not conserved in the weak-decay process.

C. N. Yang and T. D. Lee, two theorists at Brookhaven National Laboratory and at Columbia University, respectively, carefully surveyed all known experiments and found that, while all evidence clearly proved that parity is conserved in all strong and electromagnetic interactions to a high degree of accuracy, there was no evidence for parity conservation in weak interactions. It was merely an extrapolated hypothesis based on evidence and experience with the other known forces. In their paper reporting their findings, they proposed experiments that would provide definitive tests of whether or not parity is conserved in the weak interaction [LY56].

C.-S. Wu at Columbia University planned and successfully completed the first of these suggested experiments. Cold atoms of radioactive cobalt 60 aligned in the presence of a strong electromagnetic field emit electrons from their north and south poles during beta decay. Wu and coworkers at the National Bureau of Standards in Washington, D.C., where a ^{60}Co source existed, found in their experiments that the atoms preferentially emitted more electrons from one of these poles, proving that parity was not conserved in this weak-decay process [WAH+57]. These results were announced in 1957, the same year that Yang and Lee were awarded the Nobel Prize in physics for their theoretical work in the parity-nonconserving properties of the weak interaction.

1.2 Atomic experiments as tests for parity nonconservation in the weak interaction

Lee and Yang stated in their paper that if parity is not strictly conserved in weak interactions, then all nuclear and atomic states become mixtures consisting mainly of the usual pure parity state with a small percentage of an opposite parity state. The fractional weight of the latter characterizes the degree of parity nonconservation. Since parity selection rules exist and are well obeyed in atomic and nuclear physics, the degree of mixing must not be very large. This parity mixing in an atom results from the weak coupling between a valence electron and the nucleus and leads to effects in the optical properties of atoms.

Theoretical work by Zel'dovich in 1959, closely following Yang, Lee, and Wu, examined the question of PNC in atoms and calculated the size of an optical rotation effect in atomic hydrogen to be too small to be feasibly measured [Zel59]. Much later in 1974, Bouchiat and Bouchiat pointed out with detailed and comprehensive theoretical analysis that parity nonconservation should be large enough to be observable in heavy atoms [BB74a, BB74a, BB75]. They showed that heavy atoms are preferred candidates for atomic PNC measurements because the size of the PNC interaction between atomic valence electrons and the nucleus scales as Z^3 and is further enhanced by relativistic effects that increase with Z.

The Z^3 enhancement of the PNC effect can be summarized as follows. First, the weak interaction is short-range, producing a contact potential that is proportional to the probability density of the electron at the nucleus, where screening due to the other electrons is negligible. Thus for a valence electron we write $|\psi(0)|^2 \sim Z/a_0^3$, where a_0 is the Bohr radius, and pick up a factor of Z. Second, the same lack of screening causes the electron's momentum at the nucleus to increase, and we write $|\mathbf{p}| \sim Z\alpha m_e$. As derived in Section 3.2, the PNC interaction Hamiltonian is proportional to the momentum of the electron and therefore proportional to another factor of Z. Third, as we learn in the next section, the weak charge Q_{W} that also appears in the PNC interaction Hamiltonian is roughly proportional to Z.

In all atomic experiments that are sensitive to the parity-nonconserving nature of the weak interaction, measurements are based on a pseudoscalar quantity built from parameters of the experiment such as the external fields. A pseudoscalar is invariant under space rotation but changes sign under space inversion and can exist as an observable only if there is a parity-nonconserving interaction. For example, in the beta-decay experiment of Wu *et al.* on ^{60}Co, the pseudoscalar observable is $\langle \mathbf{I} \cdot \mathbf{p} \rangle$, where $\mathbf{I}$ is the nuclear spin oriented in the applied magnetic field $\mathbf{B}$ and $\mathbf{p}$ is the momentum of the emitted electron. The nuclear spin is an angular momentum and hence an axial vector, which does not change sign under a space inversion. The electron momentum is a vector, which does change sign under a space inversion. The resulting dot product is an observable pseudoscalar.

1.3 Weak-interaction information from atomic parity-nonconserving observables

In all atomic PNC experiments, the measured quantity is $\mathcal{E}_{\mathrm{PNC}}$, which can be written as

$$\mathcal{E}_{\mathrm{PNC}} = C(Z) Q_{\mathrm{W}}, \tag{1.1}$$

where $C(Z)$ is an atomic proportionality factor and Q_{W} is the weak charge [BB74b]. The PNC weak information is contained in Q_{W}, which is a measure of the vector coupling of the Z^0 to the nucleus, a neutral-current process. Charged-current processes cannot be observed in stable atoms to first order because they involve a change in the charge state of the atomic constituents. The atomic proportionality factor $C(Z)$ contains the atomic-structure information and can be determined using calculated values of the electronic wave functions evaluated at the nucleus. Inserting these calculations into Equation 1.1, one can extract a value for Q_W from the measured quantity.

In the Standard Model at tree level, without additions or radiative corrections, we can write the weak charge as

$$\begin{aligned} Q_W &= -N + Z(1 - 4\sin^2\theta_W) \qquad (1.2) \\ &= -N + Z(1 - 4\bar{x}^0), \qquad (1.3) \end{aligned}$$

where θ_W is the weak-mixing angle, the free parameter that quantifies the mixing between the Z^0 and the photon. In principle, a value of $\sin^2\theta_W$ can be extracted from an experimental determination of Q_W and then compared with high-energy measurements of the weak interaction that use complementary techniques to test the consistency of the Standard Model. See Section 1.7 for more details on comparisons with high-energy experiments.

1.4 Radiative corrections and new tree-level physics

Low-energy atomic physics experiments can and do play an important role in the verification of the Standard Model and exploration of alternatives to it. Two classes of additions to the Standard Model contribute at the few-percent level and are relevant to atomic PNC experiments with precisions at the sub-percent level. While parameterizing corrections to the Standard Model in terms of S and T is not the most general approach and does not include all new physics to which atomic PNC

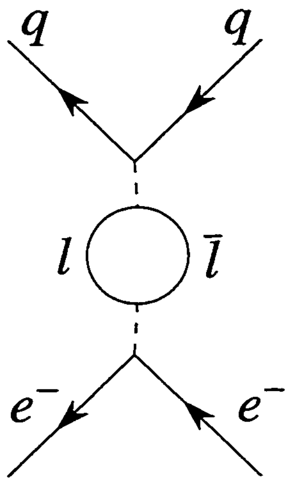

Figure 1.1: Feynman diagram of possible radiative corrections to the minimal Standard Model to which atomic PNC experiments are sensitive.

experiments are sensitive, it is the familiar formulation for atomic experiments and for that reason is used here. At low energies where atomic experiments operate, any new physics contribution to Q_{W} has the same structure as the dominant term in the weak-interaction and will fit into our formulation.

1.4.1 Radiative corrections

Oblique radiative corrections include higher order interactions with the known quarks, leptons, and bosons and with unknown new particles. The weak charge can be rewritten to include these processes [MR90, Ros98];

$$Q_{\mathrm{W}}^{\mathrm{rad}} = \rho(0)(-N + Z[1 - (4.012 \pm 0.010)\bar{x}]), \tag{1.4}$$

where

$$\rho(0) \;=\; \rho(0)^{\mathrm{SM}}\rho(0)^{\mathrm{new}},$$

$$\begin{aligned}
\rho(0)^{\mathrm{SM}} &= (0.9857 \pm 0.0004), \\
\rho(0)^{\mathrm{new}} &= 1 + 0.00782T, \\
\bar{x} &= \bar{x}^0 + \bar{x}^{\mathrm{new}}, \\
\bar{x}^0 &= 0.23166 \pm 0.00064, \\
\bar{x}^{\mathrm{new}} &= 0.00365S - 0.00261T,
\end{aligned}$$

using the latest reported average measurement for $\bar{x}^0$ from LEP and SLAC. The parameter ρ relates the neutral and charged currents. In the Standard Model at tree level and without radiative corrections, $\rho(0)^{\mathrm{SM}}=1$, as one can see by comparing Equations 1.2 and 1.4. The zero argument refers to the low-energy scale of the atomic experiments. The corrections are written in terms of the parameters S and T, the weak isospin-conserving and -breaking parameters, respectively [PT92]. Note that any nonzero values for S and/or T represent deviations from the Standard Model (when S and T are defined with the nominal values $m_{\mathrm{top}}=$ 175 GeV/c^2 and m_{Higgs} = 300 GeV/c^2 [Pes, Ros98]). Figure 1.1 contains a Feynman diagram of possible radiative corrections.

For the heavy atoms used in atomic PNC experiments, $Z \approx \frac{2}{3}N$. Inserting this approximation into Equation 1.4, we find that

$$Q_{\mathrm{W}}^{\mathrm{rad}} \approx N(-0.94 - 0.0096S - 0.00046T). \tag{1.5}$$

The T-dependence almost completely cancels out such that atomic PNC measurements at current accuracies of 0.35-3% in heavy atoms report results only for S. An earlier alternative formulation by Sandars clarifies the origin of this near cancellation [San90].

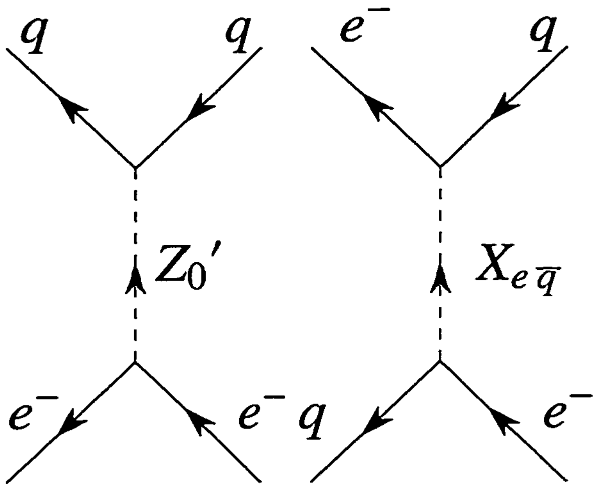

Figure 1.2: Feynman diagrams of possible new tree-level interactions. The diagram on the left represents the exchange of a new neutral vector boson Z′. The diagram on the right represents the exchange of a leptoquark.

1.4.2 Direct exchange of new particles

Atomic PNC is especially sensitive to new heavy particles that produce effects at tree level; that is, particles that can be exchanged directly between atomic electrons and the nucleus just as the Z^0 is exchanged. New tree-level physics can be included simply by adding a term to Equation 1.4, yielding

$$Q_{\mathrm{W}} = Q_{\mathrm{W}}^{\mathrm{rad}} + Q_{\mathrm{new}}^{\mathrm{tree}}. \tag{1.6}$$

$Q_{\mathrm{new}}^{\mathrm{tree}}$ allows for atomic sensitivity to new heavy particles like additional Z bosons or leptoquarks that contribute at tree level. These possibilities are shown in Feynman diagrams in Figure 1.2 and discussed in more detail in Section 1.7.

1.5 Atomic PNC experiments

In atomic experiments, the measurable PNC effect stems from the interference between two transitions that exhibit an observable pseudoscalar. The sign of the interference term reverses with the vectors in the observable, specifying the handedness of the experimental arrangement and revealing the pseudoscalar nature.

1.5.1 Recent atomic experiments

Atomic PNC has been measured in optical transitions in a number of elements. The first generations of the experiments used optical-rotation and Stark-interference methods; both techniques involve a search for an asymmetry in the atomic susceptibility of atoms interacting with left and right circularly polarized light. Heavy elements used for optical-rotation work include bismuth, lead, and thallium. Stark-interference experiments have been completed in cesium and thallium. Table 1.1 lists these experiments and includes the precisions of the results of these experiments and references to the actual results.

Table 1.1: Recent atomic PNC experimental and theoretical precisions.

Element	Method	Experimental group	Experimental precision	Atomic structure precision
Cs	Stark	Colorado [WBC$^+$97, BW99]	0.39%	0.47% [BJS90, BJS92],
	interference	Paris [BGP84]	12%	[DFS89, BW99]
Tl		Berkeley [DC85]	19%	3% [DFSS87]
Tl	optical	Seattle [VMM$^+$95]	0.5%-1%	3% [DFSS87]
	rotation	Oxford [EPBN95]	3%	
Pb		Seattle [MVM$^+$93]	1%	8% [DFSS88]
		Oxford [PEBN96]	3%	
Bi (876 nm)		Oxford [MZW$^+$91]	2%	11% [DFS89]
		Seattle [HAL$^+$81]	16%	
Bi (648 nm)		Oxford [WTS93]	9%	16%% [KPF96]
		Moscow [BBK$^+$84]	23%	
		Novosibirsk [BZ79, BZ80]	13%,13%	

Optical-rotation experiments

Optical-rotation experiments use a cell of atomic vapor. The transition of interest is an allowed $M1$ transition between states of the same parity. A beam of light with frequency ω near the resonance ω_0 of the $M1$ transition passes through a linear polarizer and then propagates through the cell. As the light interacts with the atoms in the vapor, the light's plane of polarization is rotated because, due to the parity-nonconserving nature of the interaction, the indices of refraction $n_\pm$ for the positive and negative helicity components (right and left circular polarizations) of the polarized light are different;

$$n_\pm - 1 \propto |M1|^2 \pm 2\ \mathrm{Im}(E1_{\mathrm{PNC}} \cdot M1), \tag{1.7}$$

where $E1_{\mathrm{PNC}}$ is an induced electric-dipole transition that exists between the $M1$ transition states as a result of parity mixing in those states (see Chapter 3 for more details concerning how the weak interaction mixes the parity of the atomic states). The rotation angle ϕ_{PNC} that is measured is given by

$$\phi_{\mathrm{PNC}} = -\frac{4\pi}{\lambda}(n-1)l \ \mathrm{Im}\left(\frac{E1_{\mathrm{PNC}}}{M1}\right), \tag{1.8}$$

where n is the ordinary real index of refraction due to $M1$, λ is the wavelength of the light, and l is the interaction length through the vapor. The line shape of the rotation follows the dispersive real part of the index of refraction. The pseudoscalar is $\vec{\sigma} \cdot \mathbf{k}$, where $\vec{\sigma}$ is the circular polarization of the light and $\mathbf{k}$ is the propagation vector of the light.

Stark-interference experiments

Stark-interference experiments completed in Cs and Tl use vapor cells or atomic beams. An external electric field $\mathbf{E}$ is applied to Stark mix the atomic levels, creating Stark-induced $E1$ transitions. The weak interaction also parity mixes, creating an $E1_{\mathrm{PNC}}$ transition between the same pair of states. Light polarized parallel to the electric field yields a transition amplitude βE, where β is the vector Stark-transition polarizability. The measured quantity is

$$\mathcal{R} = \mathrm{Im}\left(\frac{E1_{\mathrm{PNC}}}{\beta E}\right) \tag{1.9}$$

and requires a precise and independent determination of β. Various measurement schemes are used in the several Stark-interference experiments, yielding slightly different pseudoscalar terms in the observed transition probability. For example, the Boulder Cs experiment searches for the pseudoscalar quantity $\vec{\sigma} \cdot (\mathbf{E} \times \mathbf{B})$ in the absorption cross section of the excitation light beam with the circular polarization of the light, where $\mathbf{E}$ and $\mathbf{B}$ are the applied static fields.

1.5.2 General remarks

All atomic PNC experiments require very careful and deliberate control of systematic effects to eliminate or to understand possible errors. Common themes of these experiments include deliberate symmetry in the experimental design and auxiliary experiments to measure directly residual effects that arise from stray and imperfect fields.

The precisions in Table 1.1 display the current status of atomic PNC measurements. The techniques used and the experiments themselves represent meticulous and Herculean efforts to achieve precise measurements of $\mathcal{E}_{\mathrm{PNC}}$. The Boulder cesium experiment has set a new and impressive precedent for precision and enjoys an accurately determined atomic-structure theory. Other experiments are challenged to press their techniques any further without new innovations, and some suffer from difficult atomic-structure calculations that cannot be determined with current computational techniques to even the present accuracies of their experiments.

1.6 Isotope comparisons

A PNC measurement in a single isotope can set limits on the weak isospin-conserving parameter S in Equation 1.4. Comparisons of measurements of Q_{W} on two or more isotopes of the same element can yield different weak-force information and can offer improved precisions in the extracted result for Q_{W}.

An isotopic difference comparison provides information on the T parameter [DFK86, LS94];

$$\frac{\Delta \hat{Q}_{\mathrm{W}}}{\Delta N} = -\frac{\Delta Q_{\mathrm{W}}}{\Delta N} = -\frac{Q_{\mathrm{W}}(N_1) - Q_{\mathrm{W}}(N_2)}{N_1 - N_2} = \rho(0)^{\mathrm{new}}. \tag{1.10}$$

Much higher experimental accuracy is required for comparisons of isotopes in general because deviations from the Standard Model enter as a fractional difference in Q_{W}

between isotopes ($\Delta Q_{\mathrm{W}}/\Delta N$).

As can be noted from Table 1.1, the atomic-theory calculations that determine $C(Z)$ dominate the overall uncertainty in the best PNC results. A suggested method for circumventing the uncertainty due to the atomic theory is to make a measurement of PNC in a series of isotopes of the same element [DFK86]. Atomic theory is essentially the same from isotope to isotope, but weak effects vary as the number of neutrons varies.

Several possible ratios can be constructed from separate determinations of Q_{W} using two or more different isotopes of the same element [Ros96]. All ratios that cancel the atomic uncertainty will yield a determination of $\bar{x}$. One example is the ratio of the difference of Q_{W} to the average given by

$$\frac{\Delta Q_{\mathrm{W}}}{\bar{Q}_{\mathrm{W}}} = \frac{Q_{\mathrm{W}}(N_1) - Q_{\mathrm{W}}(N_2)}{[Q_{\mathrm{W}}(N_1) + Q_{\mathrm{W}}(N_2)]/2} = r. \tag{1.11}$$

The $\rho(0)$ dependence cancels out, yielding a determination of $\bar{x}$, which contains a nearly balanced linear combination of S and T (recall Equation 1.5). The precision of this ratio is given by

$$\frac{\delta r}{r} \approx \frac{4Z}{Z - \bar{N} - 4Z\bar{x}} \delta\bar{x}, \tag{1.12}$$

where $\bar{N}$ is $(N_1 + N_2)/2$. Again, a much higher experimental accuracy is required for comparisons of isotopes.

In the ratio, the dominating atomic-theory uncertainties can be eliminated; however, nuclear-structure uncertainties remain at some level and should be considered when choosing an appropriate element for study [FPW90, BDCZ93]. The proton distribution is well known from electric probes, but the neutron distribution is difficult to determine to the same accuracy. In intermediate-Z nuclei like Cs and Ba for single-isotope measurements, uncertainties in nuclear structure probably can be ignored compared to current uncertainties in atomic theory [PFW92].

Several high-energy experiments already measure $\bar{x}$ directly and very precisely while sitting at the Z^0 pole. However, the important sensitivity of atomic experiments to new tree-level interactions remains in this ratio and would be revealed through a comparison of atomic and high-energy results.

An experiment to cancel atomic-theory uncertainties by measuring PNC on a string of isotopes is in progress in dysprosium [DBCZ94] and is proposed in ytterbium [DeM95].

Another way to avoid the atomic-theory uncertainties is to measure atomic PNC in hydrogenic or helium-like ions with well-known atomic structure. Experiments in relativistic hydrogenic ions and in high-Z helium-like ions have been proposed [ZB97, Dun96]. Note that these types of experiments move beyond the low-energy table-top style of atomic experiments to accelerators with high-brightness ion sources and laser-cooled ion storage rings.

1.7 Atomic and high-energy electroweak data

Regardless of its current success, the Standard Model is not regarded as a complete or a final theory. Two of the many reasons are mentioned here. First, gravity is not yet included in the model. Second, the Standard Model contains numerous free parameters, not only the ideal three for an SU(3)×SU(2)×U(1) theory, that can be related only through a theory of grand unification. These extra free parameters are the masses, coupling constants, and mixing angles of the fundamental fermions that in the absence of a complete theory must be determined experimentally [Pes].

Several authors have interpreted atomic, high-energy, and nuclear weak-interaction results and have graphically compared these results to Standard Model predictions using a global fit of the electroweak parameters. A recent report by Rosner is presented and discussed here [Ros98]. The Standard Model is largely successful in that all

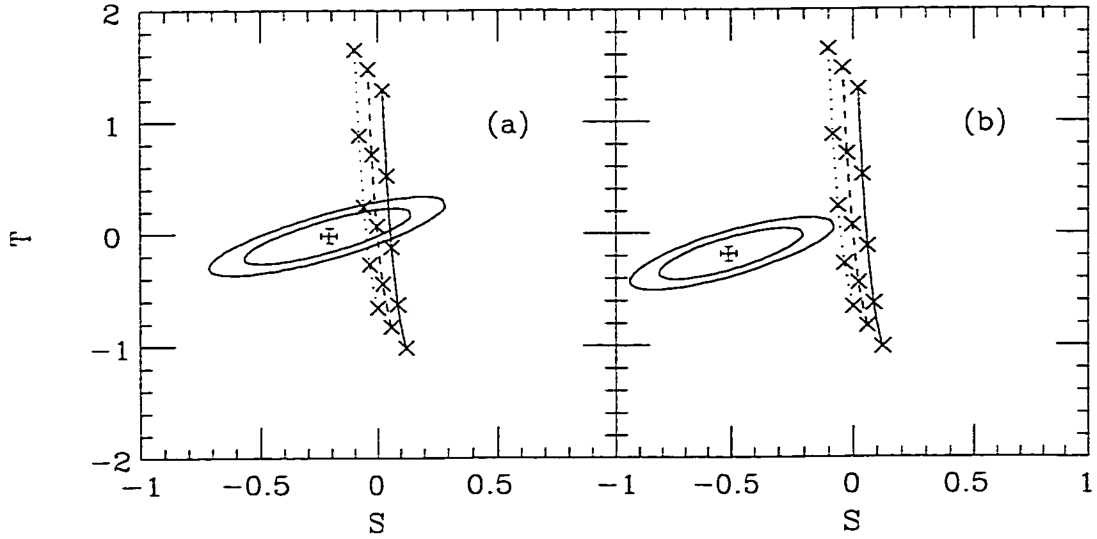

Figure 1.3: Allowed ranges of S and T at 68% (inner ellipses) and 90% (outer ellipses) confidence levels. Dotted, dashed, and solid lines correspond to Standard Model predictions for m_{Higgs}=100, 300, and 1000 GeV/c^2. Symbols ×, from bottom to top, denote predictions for m_{top}=100, 140, 180, 220, and 260 GeV/c^2. A top quark mass of 175.5±5.5 GeV/c^2 [Tip, D0] is compatible with all Higgs boson masses between 100 and 1000 GeV/c^2. Analysis includes the 1997 Boulder Cs result [WBC$^+$97] but not the 1999 reinterpretation [BW99]. Table 1.2 lists all data included in this plot. (a) Fit including atomic PNC experiments with present errors (Cs and Tl exclusively). (b) Fit with atomic PNC errors reduced from $\Delta Q_W = \pm 0.93$ (present value) to ±0.3 (hypothetical improvement), with present central values of Q_W retained. Plot taken from [Ros98].

experiments with one notable exception have determined $S = 0 = T$. In this section we discuss this one significant deviation and what new physics it may suggest.

1.7.1 Current analysis of electroweak data

In Figure 1.3, Rosner uses the data summarized in Table 1.2 to calculate ellipses of allowed S and T ranges. The analysis does not include the constraint due to the top quark mass. Each observable included in the plot specifies a band in the $S - T$ plane with a different slope, as expected from the ratios of the coefficients of S and T presented in Table 1.2.

Recall from Section 1.4 and note from the table the unique sensitivity of single-isotope atomic PNC experiments to S compared to the high-energy experiments. Predictions of S are highly model independent, unlike predictions of T.

Current determinations of S are negative, but most models including the Standard Model expect S to be zero or positive. Independent of the Standard Model predictions, values of S between -0.5 and 0.3 are permitted at the 90% confidence level. Note that a 1% overall accuracy in a measurement plus theory determines S to an accuracy of ± 1.0.

Parts (a) and (b) of the figure illustrate the possible effect of higher precision in atomic PNC experiments by assuming a hypothetical $\sim 0.1\%$ uncertainty in Q_{W} but retaining the same Q_{W} result. Under these circumstances, S is primarily determined by the atomic result. With the same Q_{W} result, the central value of S shifts negatively, further away from zero, and suggests new physics. There is no reason to assume that the Q_{W} result would be the same. The important point is that the smaller uncertainty allows the atomic result, with its unique sensitivity, to dominate the central value of S, possibly revealing new physics.

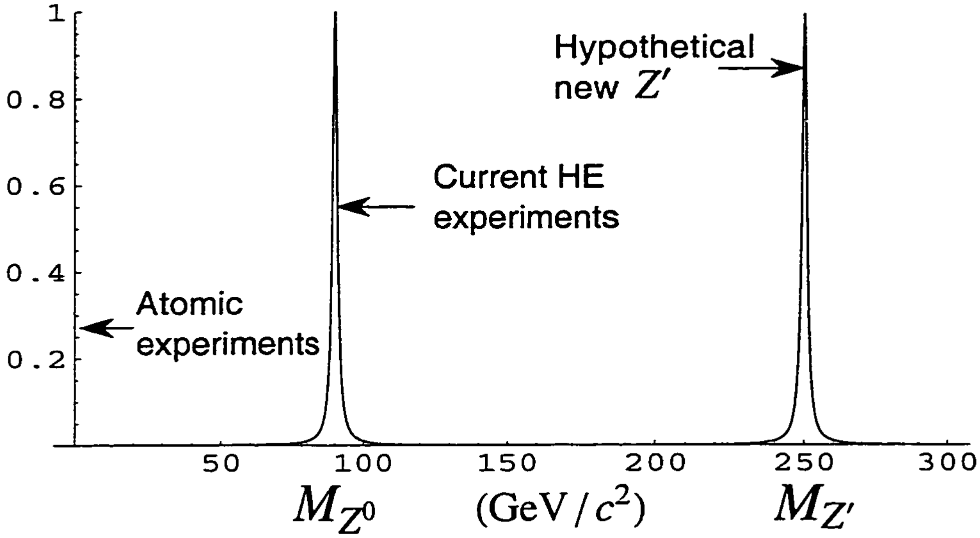

Figure 1.4: Plot illustrating the different sensitivities of high-energy and atomic experiments to a hypothetical new Z′.

1.7.2 Evidence for the direct exchange of new particles

Many alternatives to the Standard Model assume the existence of a second neutral vector boson Z′ that contributes to the weak interaction at tree level. Atomic experiments are more sensitive to new tree-level physics compared to high-energy experiments. The weak charge Q_W gains the term introduced in Section 1.4 that is proportional to $(M_{Z^0}/M_{Z'})^2$.

High-energy experiments that yield precise electroweak data (LEP and SLD) operate at the Z^0 pole and are highly insensitive to other effects that occur at other (higher) energies. The sensitivity of these experiments can be expressed in terms of the cross section of the observation σ, which is proportional to a sum of Lorentzian linewidths,

$$\sigma \propto \frac{A}{(q-M)^2+(\Gamma/2)^2}+\frac{B}{(q-M')^2+(\Gamma'/2)^2}, \tag{1.13}$$

where q is the momentum transfer of the observation, M is the mass of the particle, and Γ is the width of the resonance. At the Z^0 pole relatively far from the Z' pole where the LEP and SLD experiments operate,

$$\sigma \propto \Gamma \left(1 + \frac{\Gamma'^2}{M'^2}\right) ; \tag{1.14}$$

we have used the values and approximations that $q = M$, $q \ll M'$, $\Gamma' \approx \Gamma$, and $\Gamma \ll M$ and have set Γ equal to 3 GeV. Consider a precision of 0.1% in an experiment. From Equation 1.14, we see that such experiments are sensitive to a new tree-level Z' of mass

$$M' \sim \sqrt{1000}\Gamma' \sim 100 \text{ GeV}/c^2. \tag{1.15}$$

Figure 1.4 illustrates the point that the LEP and SLD experiments are insensitive to Z' masses much above the Z^0 mass itself.

The related quantity of merit in atomic experiments is written as

$$\mathcal{E}_{\text{PNC}} \propto \frac{g^2}{M^2} + \frac{g'^2}{M'^2}. \tag{1.16}$$

In the atomic case, the same experimental precision (0.1%) of the M term yields a sensitivity to new tree-level Z' of mass

$$M' \sim \sqrt{1000}M \sim 2 - 3 \text{ TeV}/c^2. \tag{1.17}$$

Results of direct searches for the Z' set a lower bound of 425 GeV/c^2 at the Tevatron [A+86, B+90]. Analysis of current results for Q_W from low-energy atomic experiments already indicate a lower limit of 700 Gev/c^2 for $M_{Z'}$ [RM97].

1.7.3 New physics suggested by the 1999 Cs result

A reinterpretation of the Cs result [BW99] completed after Rosner's plot was published almost matches the hypothetical uncertainty that Rosner suggested. (The value for Q_W shifts slightly to -72.06(28)(34).) The net effect of this precision is as Rosner predicted; the 1999 Cs result for S sits 2.5σ away from the Standard Model prediction and high-energy results. Plotting the Cs result for S next to the combined result of all high-energy and nuclear results, we clearly see the discrepancy as a strong hint of a new Z′ of mass 642 (maximum 1180, minimum 497) GeV/c^2 or some other form of new physics.

Rosner in a very recent publication uses the 1999 Cs result in plots similar to those in Figure 1.3 [Ros99]. He presents updated numbers that differ from those presented here using the 1998 paper, but the essential conclusions are the same. Rosner also includes the top quark mass with error bars in his new graphical analysis. The top quark mass largely determines T. The high-energy and nuclear data error bars shrink substantially and separate from the Cs result in the S and T plane, again suggesting that the Cs result includes physics to which the other experiments are not sensitive.

1.8 Concluding remarks

The goals for atomic PNC have moved beyond merely proving that a PNC effect exists and can be measured in a stable atom. More accurate measurements of $\mathcal{E}_{\text{PNC}}$ in reliably calculable atoms can and do make precise tests of the electroweak theory and can uncover new physics above the electroweak energy scale, including the effects discussed in Section 1.4. To progress further, additional measurements in other elements with tractable atomic structures that are precise at better than the few-percent level are needed to reveal these other contributions and to add to our understanding of fundamental physics.

High-energy experiments also probe this interaction, but atomic experiments are complementary and may be uniquely sensitive to new physics, as the 1999 Cs result already suggests. Discrepancies between atomic results and high-energy results that cannot be accommodated by the uncertainty ranges of the results suggest the existence of new physics.

Further, precise measurements of $\mathcal{E}_{\mathrm{PNC}}$ on atoms belonging to a chain of isotopes of the same element can provide a test of electroweak theory free from any uncertainty due to atomic physics calculations, although other uncertainties such as due to the neutron distribution in the nucleus then can become important.

Table 1.2: Electroweak observables used in the fit in Figure 1.3. Table taken from [Ros98].

Quantity	Experimental value	Theoretical value
$Q_W(\mathrm{Cs})$	-72.11±0.93 [a]	-73.20 [b]-0.80 S-0.005T
$Q_W(\mathrm{Tl})$	-115.0±4.5 [c]	-116.8 [d]-1.17S -0.06T
M_W (GeV/c^2)	80.41±0.10 [e]	80.308 [f]-0.29S+0.45T
M_W (GeV/c^2)	80.38±0.14 [g]	80.308 [f]-0.29S+0.45T
M_W (GeV/c^2)	80.35±0.21 [h]	80.308 [f]-0.29S+0.45T
$\Gamma_{ll}(Z)$ (MeV)	83.91±0.11 [i]	83.90-0.18S+0.78T
$\sin^2\theta_{\text{eff}}^{\text{lept}}$	0.23200±0.00027 [j]	0.23211 [k]+0.0036S-0.0026T
$\sin^2\theta_{\text{eff}}^{\text{lept}}$	0.23061±0.00047 [l]	0.23211 [j]+0.0036S-0.0026T
m_{top} (GeV/c^2)	175.5±5.5	175 +241 S+82T

[a] [WBC+97]

[b] Calculation [MR90, MR92] incorporating atomic physics corrections [DFS89, BJS90, BJS92].

[c] [VMM+95, EPBN95]

[d] Calculation [LS94] incorporating atomic physics corrections [DFSS87].

[e] Average of direct hadron collider measurements.

[f] Including perturbative QCD corrections [DGS96].

[g] LEP II value as of March 1997.

[h] Value from deep inelastic neutrino scattering [M+98].

[i] LEP average as of November, 1996 [LDL+].

[j] From asymmetries at LEP [LDL+].

[k] As calculated [DGS96] with correction for relation between $\sin^2\theta_{\text{eff}}^{\text{lept}}$ and $\hat{s}^2$.

[l] From left-right asymmetry in annihilations at SLC [Col96].

Chapter 2

A TRAPPED BARIUM ION AND ATOMIC PARITY NONCONSERVATION

We are exploring a novel technique to measure atomic parity nonconservation that may be sufficiently precise to attain the goals for high sensitivity to new weak physics and higher-order processes discussed in Section 1.7. The technique takes advantage of the sensitivity inherent in single-ion trapping experiments and utilizes and expands the special techniques for querying a single particle. Although we postpone descriptions of these techniques until Chapter 6, we highlight the advantages in this chapter. Singly-ionized barium is an ideal heavy element for a precise determination of the atomic PNC weak interaction; it is cesium-like with excellent prospects for sufficiently accurate atomic-structure calculations. Additionally, barium has several stable isotopes available for isotope comparisons, and the technique can accommodate different isotopes easily.

2.1 Why use ion traps?

The experiment will be performed on a single, barium ion confined in an RF electric trap. Ion traps have been used for confining charged particles for decades, and the first report of a single, trapped barium ion was published in 1980 [NHTD80]. It is a mature technology with known advantages for specific kinds of traps. Ideally a trap for ions is a three-dimensional electric potential well. Unfortunately, this ideal is impossible; it is not possible to generate a minimum of an electrostatic potential in three-dimensional free space. That is, a charged particle cannot be held in stable equilibrium by electrostatic forces alone. Fortunately, there are several ways to overcome this limitation, accounting for the variety of ion traps. The important advantages of single-ion traps for an atomic PNC measurement are discussed in this section and lead to our choice of an RF electric trap.

The advantages of ion traps are often in contrast to the situation for PNC experiments performed in atomic vapors and beams. Atoms in dense vapor cells are whirling around, crashing into each other and into the walls. Their motion automatically introduces Doppler broadening into the signals collected from the atoms. Their frequent collisions limit the coherence time of any process one may be observing and may introduce systematic errors. These two characteristics of vapors ultimately limit the experimental precision of these experiments. Atomic beams are free of some of these problems but can be limited by beam divergences and transit-time effects.

Ions in an electromagnetic trap are well isolated from the environment. Under the ultra-high vacuum (UHV) conditions of the trap, there are only rare collisions with the background gas and therefore negligible pressure broadening of spectral lines. In single-atom traps, there are also no perturbing like-atom interactions. In an RF electric trap, a cooled ion resides at the center of the trap where the trapping fields only minimally perturb the ion's energy-level structure. Also, the ion resides at the time-averaged zero electric-field center within the trapping volume such that any stray static electric fields are effectively shielded.

In most ion traps, laser cooling is possible, meaning that the motional energy of the already localized ion can be reduced to very low temperatures. This minimizes the Doppler width of spectral lines that would otherwise be due to the atom's thermal motion. A typical optical Doppler width of 1 GHz at room temperature is reduced to about 5 MHz at 10 mK, a typical laser-cooled temperature. In the Ba^+ PNC experiment, the Doppler effect virtually disappears because the wavelength of interest, $\lambda \cong 2\ \mu\text{m}$, is much larger than the orbit size, 0.1 μm. The laser-cooling beams also produce an observable fluorescence that is convenient for detecting and analyzing the quantum state of a single ion (see Chapters 4 and 6 for discussions of these techniques).

Because the ion is well localized by trapping and laser cooling, long interaction times between the probing laser and the ion are possible, minimizing transit-time broadening and maximizing the signal-to-noise ratio (see Section 2.2). This is particularly advantageous when examining long coherent processes like the Ba^+ observable, described in detail in Section 3.5. For the Ba^+ PNC measurement, standing waves are used to create an electric-field pattern that maximizes the PNC effect and minimizes other spurious effects. A trapped and cooled particle can be localized at precise points along a standing wave, such as at a node or an antinode.

Very small samples can be studied in ion traps because they yield sufficiently large signals using unique single-ion measurement techniques. This is particularly convenient when studying rare isotopes, as necessary for a study on a series of Ba^+ isotopes (see Sections 1.6 and 2.2).

The relatively perturbation-free environment of a highly localized single Ba^+ ion confined in an RF electric trap is an ideal situation for a precision atomic PNC measurement. The single-ion measurement techniques preclude many of the limiting difficulties inherent in atomic vapors and beams.

2.2 Why use barium?

All atomic samples used in PNC measurements have contained neutral atoms. This experiment using barium is the first attempt to measure atomic PNC in an ion. Barium is a natural choice to exploit ion-trapping techniques, as we discuss in this section. It also exhibits an observable PNC effect, which is detailed in Section 3.5.

Table 2.1: Comparison of the enhancement factors of heavy atoms used in atomic PNC experiments. The relativistic correction factor is given in Equation 2.1.

Element	Z	K_r	Z^3K_r
Cs	55	2.8	470×10^3
Ba	56	2.9	510×10^3
Tl	81	8.5	4500×10^3
Pb	82	8.9	4900×10^3
Bi	83	9.4	5400×10^3
Ra	88	12.3	8400×10^3

2.2.1 Heavy atom

Barium, which comes from the Greek word *barys* meaning heavy, possesses the usual enhancement of an atomic PNC effect because of its high Z=56. We can quantify the enhancement for any given atom as $Z^3K_r(Z,R)$. The relativistic correction factor $K_r(Z,R)$ introduced by Bouchiat and Bouchiat [BB74a] for heavy atoms ($Z > 50$) is given by

$$K_r(Z,R) \approx \left[\frac{\Gamma(3)}{\Gamma(2\sqrt{1-(Z\alpha)^2}+1)}\left(\frac{2ZR}{a_0}\right)^{\sqrt{1-(Z\alpha)^2}-1}\right]^2, \tag{2.1}$$

where R is the nuclear radius, estimated as $R \simeq 1.2A^{1/3} \times 10^{-15}$ m. For $^{138}\mathrm{Ba}^+$, $K_r = 2.9$. See Table 2.1 for a comparison of the enhancements of barium and other atoms.

2.2.2 Trappable ion

Having chosen to design an atomic PNC atomic experiment in an ion trap, barium is a natural choice for the first effort. Barium was the first atomic ion to be singly trapped, and in-house expertise already exists at the University of Washington. Precision atomic measurements have been made using the system, mapping out several atomic quantities of interest for a PNC measurement and establishing single-ion techniques ideally suited for precision measurements.

2.2.3 Available light sources

The transitions of interest in Ba^+ for laser cooling and other relevant trapped-ion techniques such as shelving (see Chapter 6) and for driving the PNC effect are readily available in solid-state laser technology (see Section 4.7). The highly stable solid-state laser systems are necessary for a precision measurement such as the PNC observable because of the large quantity of data required to achieve the necessary statistics. The lasers are expected to run continuously without manual handling for several days at a time and particularly overnight. Also, it is typical to spend just as much if not more data-acquisition time studying the systematic effects, increasing the total data-acquisition time requiring constant laser use.

2.2.4 Atomic theory

The electronic structure of Ba^+ is like cesium, with a single valence electron outside a tightly closed shell. Of all the heavy atoms used for PNC measurements, cesium has the most accurately calculated atomic-structure theory (see Table 1.1) at a 0.47% uncertainty. The atomic-structure calculations for Ba^+ are expected to be at least as precise. Work is in progress to complete relativistic many-body calculations of energy levels and transition rates for ions with one valence electron [SDJ98]. The initial results for similar lighter atoms indicate precisions of 0.1-0.3% in comparison with measured transition amplitudes and other experimental data. We therefore predict a similar precision for atomic-structure calculations of Ba$^+$;

$$\frac{\delta C(Z)}{C(Z)} \sim 0.3\%, \tag{2.2}$$

where $C(Z)$ was defined in Equation 1.1.

A calculation of the contributions to PNC in ^{137}Ba$^+$ from neutral weak currents has been made using a relativistic configuration-interaction approach [MSD95]. The authors conclude that any reliable theory of PNC for Ba$^+$ should incorporate the many-body effects arising from low-lying configurations, including the core and $6s, 5d$, and $6p$ orbitals, as they have done in their analysis of ^{137}Ba$^+$. In future work, they propose including the effects of other configurations.

2.2.5 Isotopic comparisons

Barium presents many opportunities for the isotopic comparisons discussed in Section 1.6. Barium has seven stable isotopes and 22 known radioactive isotopes. Table 2.2 lists all stable isotopes and includes radioactives with half lives on the order of days. Five of the stable isotopes have favorable even-even nuclei, with minimal nuclear-structure uncertainties, and are trappable. The two isotopes with lifetimes of at least two days are also feasible for use in a single-ion experiment and extend the mass range of isotopes.

2.2.6 Nuclear uncertainties

In atomic-structure calculations, nuclear-size effects enter at the 0.3% level in middle-Z elements like barium [MSH78]. Fortunately, in even-even barium nuclei, the neutron distribution can be determined accurately by measurements of the electroweak interference in polarized-electron/nucleus scattering [DDS89, Mar97, Mar]. Experiments

Table 2.2: Stable and long-lived isotopes of barium. There are a total of seven stable isotopes and 22 known radioactive isotopes. Five of the stable isotopes are the favorable even-even nuclei. Even isotopes without hyperfine structure are the easiest to trap. Two isotopes with lifetimes of at least two days extend the mass difference to $\Delta N = 12$.

Atomic mass	Natural abundance	Lifetime	Nuclear spin
140		12.8 days	0
138	71.70%	stable	0
137	11.32%	stable	3/2
136	7.854%	stable	0
135	6.592%	stable	3/2
134	2.42 %	stable	0
132	0.10 %	stable	0
130	0.11 %	stable	0
128		2.42 days	0

on ^{138}Ba have been proposed and would be conducted at the Continuous Electron Beam Accelerator at the Thomas Jefferson National Accelerator Facility. Expectations are for $\delta R_N/R_N \approx 0.1\%$, where R_N is the r.m.s. of the neutron distribution, consistent with the predictions for experimental and atomic-structure uncertainties.

2.3 Inherent statistical accuracy

I have discussed several advantages of choosing barium and of using single-ion traps. One particularly obvious statistical limitation for single-ion trapping experiments in general that also concerns our experiment is that there is only one ion participating

Table 2.3: Comparison of the statistical power of various atomic PNC experiments. Total measurement time of $t = 1$ day is used. The key advantages for the ion PNC experiment are in the intensely focused laser beams and the longer coherence time.

Experiment	$\mathcal{E}_{PNC}$	E	N	τ	S/N
Single ion	$10^{-10}ea_0$	10^4 V/cm	1	50 s	1000's
Oven source	$10^{-9}ea_0$	3 V/cm	10^{15}	10^{-8} s	1000's

in the measurement. The high signals that are provided by dense atomic beams or vapors are therefore lost; but there are compensating advantages.

For perspective on the advantages and disadvantages, we compare the experimental sensitivities of a single-ion experiment and a traditional beam or oven experiment. This will show how our experiment is fundamentally different than typical atomic PNC experiments and yet can achieve a comparable statistical signal-to-noise ratio.

For the transition dipole resulting from parity mixing, we can approximate the S/N ratio as

$$\frac{\mathcal{E}_{PNC}}{\delta\mathcal{E}_{PNC}} \cong \frac{\mathcal{E}_{PNC}}{\hbar} E f \sqrt{N\tau t}, \tag{2.3}$$

where $\mathcal{E}_{PNC}$ is the dipole moment, $\delta\mathcal{E}_{PNC}$ is the shot-noise-limited uncertainty, E is the electric field of the laser driving the dipole transition, f is an efficiency factor determined by experimental conditions, N is the number of atoms or ions participating in the measurement, τ is the coherence time, and t is the total measurement time. The efficiency factor for our experiment is limited by the sensitivity to the spin polarization and the fraction of the full exponential decay time τ that can be utilized during each measurement cycle. A pessimistic estimate would be $f \approx 0.1$. We assume roughly the same efficiency factor for other experiments. See Table 2.3 for the values used to estimate $\mathcal{E}_{PNC}/\delta\mathcal{E}_{PNC}$.

A single trapped ion is highly localized, allowing tightly focused laser beams that drive the PNC effect, boosting our S/N ratio. The single ion will not undergo collisions with other ions, allowing us to utilize nearly the full lifetime of the upper state of the PNC transition. The 10^{-8} s coherence time of the beam and oven experiments is limited primarily by radiative or collisional relaxation. These factors compensate for the serious loss in N that the single-ion experiment suffers. The result is a comparable signal/noise ratio (see again Table 2.3).

2.4 Concluding remarks

Single-ion, RF electric traps provide a unique environment for precise atomic measurements. Ba^+ exhibits the PNC effect in an accessible location with good sensitivity. Together barium and traps provide the opportunity for a new precision limit in atomic PNC results. We predict that in our experiment

$$\frac{\delta\mathcal{E}_{\mathcal{PNC}}}{\mathcal{E}_{\mathcal{PNC}}} \approx 0.1\%. \tag{2.4}$$

Combined with the tractable atomic theory of alkali-like Ba^+ quoted in Equation 2.2 as 0.1%, this result would provide another decisive atomic test of electroweak physics.

Chapter 3

ELECTROWEAK THEORY IN THE BARIUM ION

The Standard Model of the electroweak interaction was formulated in the 1960s by Glashow, Weinberg, and Salam [Gla61, Wei67, Sal68]. They used principles of local gauge invariance and spontaneous symmetry breaking to show that the electromagnetic and weak interactions could be understood as manifestations of a single underlying interaction. The unified theory predicted a new gauge boson Z^0 that carried no charge and mediated a neutral current weak interaction. Being neutral, this interaction does not change the charge of the interacting particles, implying correctly that the interaction could be observed in a stable atom. In this chapter we explore the neutral current weak interaction and show how it can be observed in a barium ion.

3.1 Z^0 and the neutral current

The first observation of a neutral current process mediated by the Z^0 was in neutrino-electron scattering at CERN in 1973 [H^+73]. This observation was an important confirmation of the Standard Model that had predicted its existence. Z^0 resonances were directly observed in 1983 at CERN [Col83a, Col83b, Col83c]. The most recent determination of the Z^0 boson mass is 91.1863 ± 0.0020 GeV/c^2 [LDL^+].

PNC in atoms is a result of the electroweak interaction between electrons and nucleons and is dominated by the exchange of the Z^0; see Figure 3.1. The effect is manifested through the mixing of opposite-parity atomic states, producing observable

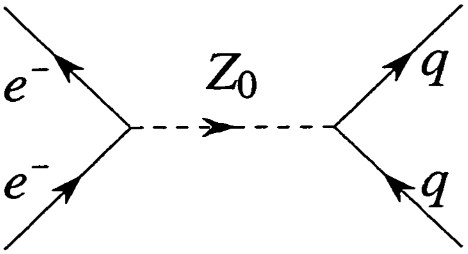

Figure 3.1: Feynman diagram of the dominant term of the weak interaction observed in atomic PNC experiments, due to the exchange of the Z^0.

PNC effects in ordinary electromagnetic phenomena.

Because the mediator is so massive, the quark-electron interaction due to Z^0 exchange is zero range compared to atomic distances, to a good approximation. If the nucleus is assumed to contain a static weak charge, then the field due to the weak charge is Yukawa in form and decays exponentially with a length scale given by the Compton wavelength of the Z^0. This wavelength is written as

$$\lambda_{Z^0} = \frac{\hbar}{M_{Z^0} c} \approx 2 \times 10^{-18} \text{ m}, \tag{3.1}$$

where M_{Z^0} is the Z^0 mass. This value is much smaller than the atomic length scale characterized by the Bohr radius, given by

$$a_0 = \frac{\hbar}{m_e c \alpha} \approx 0.05 \text{ nm}, \tag{3.2}$$

where m_e is the electron mass and $\alpha \approx 1/137$ is the fine-structure constant. It is also several orders of magnitude smaller than the nucleus itself (on the order of 10^{-15} m), justifying the point interaction that we shall assume. In the limit of an infinitely massive Z^0, the potential associated with this electric field becomes a delta function, a fact that we use in the next section.

3.2 Atomic parity-nonconserving Hamiltonian

The tree-level neutral weak interaction is described by the parity-nonconserving Hamiltonian $\mathcal{H}_{\rm PNC}$ built from the electronic and nucleonic neutral weak currents J^μ. In principle, we should write the hadronic currents in terms of the quarks. For our purposes, it suffices to use the composite nucleons and treat them as Dirac point particles. (Later we sum over all nucleons and consider the nucleus as a point particle.) Each current contains vector and axial-vector components,

$$\begin{aligned} J_e^\mu &= V_e^\mu + A_e^\mu \propto a\bar{\psi}_e\gamma^\mu\psi_e + b\bar{\psi}_e\gamma^5\gamma^\mu\psi_e, && (3.3)\\ J_n^\mu &= V_n^\mu + A_n^\mu \propto c\bar{\psi}_n\gamma^\mu\psi_n + d\bar{\psi}_n\gamma^5\gamma^\mu\psi_n, && (3.4)\end{aligned}$$

where $a, b, c,$ and d are coefficients and the γ^μ are the Dirac γ-matrices. The ψ are electronic and nuclear wave functions, where we introduce an unlabeled convention that the wave function on the left is always the final state and the wave function on the right is the initial state.

The currents interact, yielding two scalar and two pseudoscalar terms. The scalar parts, $V_e^\mu V_n^\mu + A_e^\mu A_n^\mu$, are not parity violating and therefore ignored here. The pseudoscalar terms remain and give the form of the PNC Hamiltonian;

$$\mathcal{H}_{\rm PNC} = V_n A_e + A_n V_e. \tag{3.5}$$

The two terms take the following explicit forms:

$$\begin{aligned} \mathcal{H}_{\rm PNC} &= \mathcal{H}_1 + \mathcal{H}_2, && (3.6)\\ \mathcal{H}_1 &= \frac{G_F}{\sqrt{2}}\sum_{e,n} C_{1n}\int \bar{\psi}_n\gamma_\mu\psi_n\bar{\psi}_e\gamma^\mu\gamma^5\psi_e d^3r, && (3.7)\\ \mathcal{H}_2 &= \frac{G_F}{\sqrt{2}}\sum_{e,n} C_{2n}\int \bar{\psi}_n\gamma_\mu\gamma^5\psi_n\bar{\psi}_e\gamma^\mu\psi_e d^3r, && (3.8)\end{aligned}$$

where the sum is over all electrons e and nucleons n in the atom. The characteristic strength of the weak interaction is determined by the Fermi weak coupling constant,

$$G_{\mathrm{F}} \cong 3 \times 10^{-12}\, m_e c^2 \left(\frac{\hbar}{m_e c}\right)^3 \tag{3.9}$$

$$= 1.16639(2) \times 10^{-5} (\mathrm{GeV}/c^2)^{-2}. \tag{3.10}$$

The nucleons are nonrelativistic inside the nucleus, allowing us to simplify the integral representation. In preparation for taking the nonrelativistic limit, we insert the definition $\bar{\psi} = \psi^\dagger \gamma_0$. Examining the matrix products by substituting the appropriate forms for the Dirac matrices and then taking the limit, we find that Equations 3.7 and 3.8 reduce to

$$\mathcal{H}_1 \approx \frac{G_F}{\sqrt{2}} \sum_{e,n} C_{1n} \int \psi_n^\dagger \psi_n \psi_e^\dagger \gamma^5 \psi_e d^3 r, \tag{3.11}$$

$$\mathcal{H}_2 \approx \frac{G_F}{\sqrt{2}} \sum_{e,n} C_{2n} \int \psi_n^\dagger \vec{\gamma} \gamma^5 \psi_n \cdot \psi_e^\dagger \vec{\alpha} \psi_e d^3 r, \tag{3.12}$$

where we have also used the definition $\vec{\gamma} = \gamma_0 \vec{\alpha}$. The C's are coupling constants, given in the Standard Model by

$$C_{1P} = \frac{1}{2}(1 - 4\bar{x}), \tag{3.13}$$

$$C_{2P} = \frac{1}{2}(1 - 4\bar{x}) g_A, \tag{3.14}$$

$$C_{1N} = -\frac{1}{2}, \tag{3.15}$$

$$C_{2N} = -\frac{1}{2}(1 - 4\bar{x}) g_A, \tag{3.16}$$

where $g_A \approx 1.25$ is the axial-vector coupling constant of neutron beta decay and $\bar{x}$ was defined in Equation 1.4.

The term $\mathcal{H}_2$ reduces in the limit just taken to a sum over the nucleonic spins that cancel in pairs, leaving a contribution only from the odd spin. In general this contribution is much smaller than $\mathcal{H}_1$, and in the specific case of $^{138}\mathrm{Ba}^+$ with no odd spin, the contribution is zero.

The interaction Hamiltonian $\mathcal{H}_{\text{PNC}}$ therefore reduces to the $\mathcal{H}_1$ term and is written as

$$\mathcal{H}_{\text{PNC}} = \frac{G_{\text{F}}}{2\sqrt{2}} \sum_e \int \left[-N\rho_N(r) + Z(1-4\bar{x})\rho_P(r)\right] \psi_e^\dagger \gamma^5 \psi_e d^3r, \tag{3.17}$$

where we have used $N\rho_N(r) = \psi_N^\dagger \psi_N$ and $Z\rho_P(r) = \psi_P^\dagger \psi_P$. If we now assume $\rho_N(r) \simeq \rho_P(r) \equiv \rho(r)$, then we recognize in Equation 3.17 the weak charge Q_W.

$$\mathcal{H}_{\text{PNC}} = \left(\frac{G_{\text{F}}}{2\sqrt{2}}\right) Q_{\text{W}} \int \rho(r) \psi_e^\dagger \gamma^5 \psi_e d^3r, \tag{3.18}$$

where we eliminate the appearance of the the sum over all electrons because we recognize that the dominant effect in Ba$^+$ comes from a single valence electron. Contributions from the core electrons are very small because these electrons are rarely in excited states. Q_{W} represents the combined effect of the weak charges of all the quarks in the nucleus; $Q_{\text{W}} = (2Z+N)Q_{\text{W}}(\text{u}) + (Z+2N)Q_{\text{W}}(\text{d})$.

Finally, we take the nonrelativistic limit for the electrons, which is not strictly valid but is useful for illustrating the structure of the interaction. The interaction Hamiltonian reduces to

$$\mathcal{H}_{\text{PNC}} = \left(\frac{G_{\text{F}}}{2\sqrt{2}}\right) Q_{\text{W}} \int \rho(r) \psi_f^\dagger \left(\frac{\vec{\sigma}_e \cdot \vec{p}}{m_e c}\right) \psi_i d^3r. \tag{3.19}$$

Note that the $\vec{\sigma}$ are the Pauli spin matrices. Since we shall be concerned with only transition matrix elements using this Hamiltonian, we explicitly indicate with subscripts on the electron wave functions the initial and final states of the single valence electron involved in the transitions.

We approximate the nuclear charge density with a delta function located at the origin where we place the nucleus and integrate over all space to obtain as our final form of the PNC Hamiltonian,

$$\mathcal{H}_{\text{PNC}} = \left(\frac{G_{\text{F}}}{2\sqrt{2}}\right) Q_{\text{W}} \psi_f^\dagger(0)(\vec{\sigma} \cdot \vec{p})\psi_i(0). \tag{3.20}$$

There are two other terms that contribute to atomic PNC. They can be written as

$$\mathcal{H}_{\mathrm{A}} + \mathcal{H}_{\mathrm{ee}}, \tag{3.21}$$

where $\mathcal{H}_{\mathrm{A}}$ is a contribution due to an anapole moment and $\mathcal{H}_{\mathrm{ee}}$ is due to Z^0 exchange between electrons. The anapole moment arises because nuclear states are also parity mixed by the weak interaction, as recognized by Yang and Lee [LY56]. This moment can then interact with the atomic electrons via the electromagnetic interaction. The first observation and measurement of an anapole moment in an atom was recently reported in cesium [WBC+97]. Since $^{138}\mathrm{Ba}^+$ has no net nuclear spin, there is no anapole moment, and we shall not discuss it further in this work.

The term $\mathcal{H}_{\mathrm{ee}}$ is estimated to be on the same order as the spin-dependent term $\mathcal{H}_2$, that is, nominally less than 1% of the spin-independent term $\mathcal{H}_1$. It is in fact much further reduced because of the small factor $(1 - 4\sin^2\theta_{\mathrm{W}})$ and will be ignored in this discussion.

3.3 Parity-mixed atomic states

The total electroweak atomic Hamiltonian can be written as the sum of three terms

$$\mathcal{H} = \mathcal{H}_0 + \mathcal{H}_{\mathrm{PNC}} + \mathcal{H}_{\mathrm{PC}}^{\mathrm{weak}}, \tag{3.22}$$

where $\mathcal{H}_0$ is the unperturbed atomic electromagnetic Hamiltonian and $\mathcal{H}_{\mathrm{PNC}}$ is described adequately for our purposes in Equation 3.20. $\mathcal{H}_{\mathrm{PC}}^{\mathrm{weak}}$ describes the part of the weak interaction that conserves parity. It is the same order as the PNC effect but being parity conserving has no unique feature to distinguish it from the overwhelmingly large electromagnetic effects. For these reasons this part of the weak interaction is not measured in atomic PNC experiments.

The eigenstates of the Coulomb Hamiltonian have definite parity, but they are perturbed by $\mathcal{H}_{\rm PNC}$ and thus admixed with states of opposite parity. Using perturbation theory, we can write the new eigenkets as

$$|k^0\rangle \rightarrow |k\rangle = |k^0\rangle + \sum_l \frac{|l^0\rangle\langle l^0|\mathcal{H}_{\rm PNC}|k^0\rangle}{E_{k^0} - E_{l^0}}, \tag{3.23}$$

where $|k^0\rangle$ and E_{k^0} are the exact eigenfunctions and eigenvalues in the absence of the perturbation $\mathcal{H}_{\rm PNC}$. First-order perturbation theory is justified here because the perturbation due to $\mathcal{H}_{\rm PNC}$ is extremely small. The linear momentum factor in $\mathcal{H}_{\rm PNC}$ contains a radial-coordinate gradient. The delta function of $\mathcal{H}_{\rm PNC}$ means that the entire matrix element in Equation 3.23 is evaluated at the nucleus. For these reasons, matrix elements of $\mathcal{H}_{\rm PNC}$ are nonzero only for electron orbitals with finite value and gradient at the nucleus. The pseudoscalar $\mathcal{H}_{\rm PNC}$ therefore only appreciably mixes S and P orbitals. In Ba$^+$, the $6S_{1/2}$ ground state is mixed with some $nP_{1/2}$ states only, since $\mathcal{H}_{\rm PNC}$ cannot change the total angular momentum of the state.

3.4 Parity-induced electric-dipole amplitude

Consider an electromagnetic transition amplitude between stationary states of the same parity, like an electric-quadrupole transition $E2$. If we turn on the perturbation $\mathcal{H}_{\rm PNC}$, the transition can gain an additional PNC electric-dipole amplitude $\mathcal{E}_{\rm PNC}$, where the electric-dipole operator is given by

$$\hat{E}_1 = -\sum_j e\vec{r}_j \tag{3.24}$$

with a sum over all spatial coordinates.

The amplitude of the electric-dipole transition between the initial and final states as a result of the PNC mixing is given by $\mathcal{E}_{\rm PNC}$:

$$\mathcal{E}_{\rm PNC} = \sum_n \left[\frac{\langle f|\hat{E}_1|n\rangle\langle n|\mathcal{H}_{\rm PNC}|i\rangle}{W_i - W_n} + \frac{\langle f|\mathcal{H}_{\rm PNC}|n\rangle\langle n|\hat{E}_1|i\rangle}{W_f - W_n} \right], \tag{3.25}$$

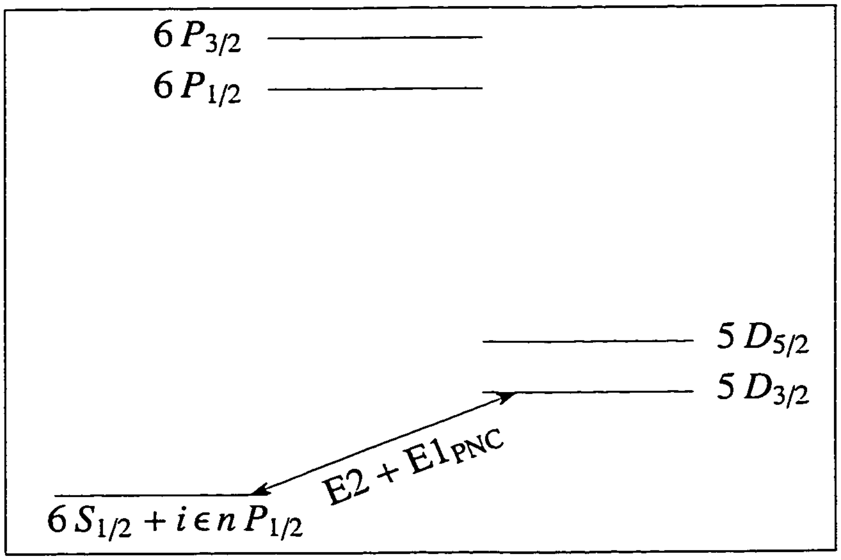

Figure 3.2: Ba^+ energy-level diagram with parity-mixed ground state, including only low-lying levels of interest. A nonvanishing electric-dipole transition amplitude exists between the $6S_{1/2}$ ground state and the $5D_{3/2}$ excited state as a result of $nP_{1/2}$ states being mixed into the ground state by the weak interaction.

where $|f\rangle$ are the final states, $|i\rangle$ are the initial states, W is the energy of the state, and the sum is over all intermediary states. Since both $\mathcal{H}_{\mathrm{PNC}}$ and $\hat{E}_1$ have odd parity, nonzero matrix elements $\mathcal{E}_{\mathrm{PNC}}(fi)$ exist only when $\langle f|$ and $|i\rangle$ are of the same parity. Diagonal matrix elements of $\mathcal{H}_{\mathrm{PNC}}$ are zero, meaning that $\mathcal{H}_{\mathrm{PNC}}$ does not mix the same state into itself and that there is no energy-level shift of first order, which would otherwise be more straightforward to observe. The addition of opposite parity states into the ground state adds an electric-dipole component to the already existing electric-quadrupole transition between the ground and $5D_{3/2}$ states. From Equation 3.25, we write

$$\mathcal{E}_{m'm}^{\mathrm{PNC}} = \sum_n \frac{\langle 5D_{3/2,m'}|e\mathrm{r}|nP_{1/2,m}\rangle\langle nP_{1/2,m}|\mathcal{H}_{\mathrm{PNC}}|6S_{1/2,m}\rangle}{W_{6S_{1/2}} - W_{nP_{1/2}}}. \tag{3.26}$$

By summing over all n, we are allowing for mixing into the ground state from all possible $nP_{1/2}$ states. The $\mathcal{H}_{\mathrm{PNC}}$ matrix elements are much smaller for higher n values in $nP_{1/2}$ other than 6 or 7, although precise calculations of PNC in barium would include all n and the continuum states. Figure 3.2 shows the energy-level structure for Ba$^+$ including the parity-mixed ground state and the electric dipole and quadrupole transitions. The second term in Equation 3.25 does not contribute to the result in Equation 3.26 because $\mathcal{H}_{\mathrm{PNC}}$ does not mix the parity of the upper $5D_{3/2}$ state.

3.5 PNC observable in Ba$^+$

The transition dipole moment due to PNC is observable through its interference with other atomic moments in radiative transitions. For example, in the optical rotation experiments summarized in Section 1.5.1, the interference term is $M1 - E1_{\mathrm{PNC}}$ and is detected as a rotation of the plane of polarization of the interacting laser light. The $E2 - E1_{\mathrm{PNC}}$ interference term in Ba$^+$ is detected as a light shift in the $6S_{1/2}$

ground-state Zeeman splitting. A light shift can be described as an energy shift of the atomic levels due to the interaction of these levels with the strong electric fields of intense laser light. In the case of Ba^+ and the transition of interest, the magnitude of the total light shift is altered by the presence of P-states mixed into the ground state as a result of PNC.

3.5.1 The shift

The total shift of the ground-state magnetic sublevels includes contributions from $\Delta m = m' - m = 0, \pm 1, \pm 2$ transitions. The light fields used to drive the transitions ideally can be polarized to select only one of these transitions; therefore we do the same in our analysis here and limit our discussion to $\Delta m = \pm 1$ transitions. To quantify the light shift, we first write the transition matrix elements of the electric quadrupole and PNC-dipole couplings to the laser field in terms of the Rabi frequency defined below:

$$\Omega_{m'm} = \Omega^{\mathrm{quad}}_{m'm} + \Omega^{\mathrm{PNC}}_{m'm}, \tag{3.27}$$

where the subscript m denotes a magnetic sublevel of the ground state and m' the same of the excited state. The electric-quadrupole and the electric-dipole PNC-induced couplings are given, respectively, by

$$\Omega^{\mathrm{quad}}_{m'm} = -\frac{1}{2\hbar}\sum_{i,j}(\mathcal{E}^{\mathrm{quad}}_{m'm})_{i,j}\left[\frac{\partial E''_i}{\partial x_j}\right]_0, \tag{3.28}$$

$$\Omega^{\mathrm{PNC}}_{m'm} = -\frac{1}{2\hbar}\sum_{i}(\mathcal{E}^{\mathrm{PNC}}_{m'm})_i E'_i(0), \tag{3.29}$$

where $\mathcal{E}^{\mathrm{PNC}}_{m'm}$ is given in Equation 3.26 and $\mathcal{E}^{\mathrm{quad}}_{m'm}$ is defined by

$$(\mathcal{E}^{\mathrm{quad}}_{m'm})_{i,j} \equiv \langle 5D_{3/2,m'}|\frac{e}{6}(3x_i x_j - r^2\delta_{ij})|6S_{1/2,m}\rangle. \tag{3.30}$$

The electric-field quantities in both couplings are evaluated at $r = 0$, the spatial location of the ion inside the trap. The sum over i, j includes the components x, y, z

defined with respect to the chosen quantization axis. Note that Ω^{PNC} is proportional to the electric-field amplitude and Ω^{quad} is proportional to the electric-field gradient.

If the ion is placed initially in the mth magnetic sublevel of the $6S_{1/2}$ ground state, the optical field driving the $6S_{1/2} \rightarrow 5D_{3/2}$ transition will induce an energy shift $\hbar\Delta\omega_m$ as well as a loss rate Γ_m to this sublevel. It is the energy shift that will concern us primarily, but for completeness we consider the total complex shift given by

$$\mathbf{a}_m = \Delta\omega_m - i\frac{\Gamma_m}{2}. \tag{3.31}$$

We apply a small magnetic field to split the Zeeman sublevels by a known amount. In this limit, the solution to the set of equations of motion for the amplitudes of the two-level system is given by

$$\mathbf{a}_m = \frac{1}{2}\left(\omega_0 - \omega - i\frac{\gamma_{5D}}{2}\right) \pm \frac{1}{2}\left[(\omega_0 - \omega - i\frac{\gamma_{5D}}{2})^2 + 4\Omega_m^2\right]^{1/2}, \tag{3.32}$$

where $\hbar\omega_0 = W_{5D_{3/2}} - W_{6S_{1/2}}$, γ_{5D} is the decay rate of the $5D_{3/2}$ state, and ω is the laser-field frequency. Ω_m^2 is given by

$$\Omega_m^2 = \sum_{m'} |\Omega_{m'm}|^2 = \sum_{m'}[|\Omega_{m'm}^{\mathrm{quad}}|^2 + 2\mathrm{Re}(\Omega_{m'm}^{\mathrm{PNC}*}\Omega_{m'm}^{\mathrm{quad}}) + |\Omega_{m'm}^{\mathrm{PNC}}|^2], \tag{3.33}$$

where we explicitly note that $\Omega_{m'm}^{\mathrm{PNC}}$ is purely imaginary.

In Equation 3.33, the term quadratic in Ω^{PNC} is too small to observe. The term linear in $\Omega_{m'm}^{\mathrm{PNC}}$ is still small but possible to measure and is the $E2-E1_{\mathrm{PNC}}$ interference term that leads to the observable PNC-induced light shift.

Assume that $\Omega_m >> |\omega_0 - \omega - i\gamma_{5D}/2|$, which would be the usual conditions of operation since the lifetime of the upper state is long and the electric field of the laser is intense. Then we can write

$$\begin{aligned} \mathbf{a}_m &\simeq \frac{1}{2}(\omega_0 - \omega) - i\frac{\gamma_{5D}}{4} \pm \frac{1}{2}\sqrt{4\Omega_m^2}, & (3.34)\\ &= \frac{\omega_0 - \omega}{2} \pm \Omega_m - i\frac{\gamma_{5D}}{4}. & (3.35) \end{aligned}$$

Comparing this final expression to Equation 3.31, we can by inspection pick out the real and imaginary parts of the complex level shift;

$$\Delta\omega = \frac{(\omega_0 - \omega)}{2} \pm \Omega_m, \tag{3.36}$$

$$\Gamma_m = \frac{\gamma_{5D}}{2}. \tag{3.37}$$

The loss rate is half the natural lifetime of the upper state. The ion being driven between the $6S_{1/2}$ and $5D_{3/2}$ states spends about half of its time in the upper state.

Part of the total light shift in Equation 3.36 is due to PNC and contains the weak-interaction information;

$$\Delta\omega = \frac{\omega_0 - \omega}{2} - \Omega_m = \frac{\omega_0 - \omega}{2} - \sqrt{\sum_{m'} |\Omega_{m'm}|^2} = \Delta\omega_m^{\text{quad}} + \Delta\omega_m^{\text{PNC}}. \tag{3.38}$$

The largest part of the total shift is due to the pure quadrupole term,

$$\Delta\omega_m^{\text{quad}} = \frac{\omega_0 - \omega}{2} - \sqrt{\sum_{m'} |\Omega_{m'm}^{\text{quad}}|^2} \cong \frac{\omega_0 - \omega}{2} - \Omega_m^{\text{quad}}, \tag{3.39}$$

which is proportional to m^2 and therefore independent of $m = \pm 1/2$. The small remainder of the shift is the PNC part due to the interference term linear in $\Omega_{m'm}^{\text{PNC}}$ in Equation 3.33;

$$\Delta\omega_m^{\text{PNC}} \cong -\frac{\operatorname{Re} \sum_{m'} (\Omega_{m'm}^{\text{PNC}*} \Omega_{m'm}^{\text{quad}})}{\Omega_m^{\text{quad}}}, \tag{3.40}$$

which we find by taking a Taylor-series expansion of the square-root term in Equation 3.38. In contrast to the quadrupole part, this quantity is m dependent for our case.

The ground state of Ba^+ has two magnetic sublevels $m = \pm 1/2$. $\Delta\omega^{\text{PNC}}$ shifts the $m = \pm 1/2$ sublevels by the same amount in opposite directions, to higher and lower frequency values. $\Delta\omega^{\text{quad}}$ shifts the $m = \pm 1/2$ sublevels by the equal amounts in the same direction, both higher or both lower. Both shifts occur when the laser light is driving the $6S_{1/2} + nP_{1/2} \leftrightarrow 5D_{3/2}$ transition, as described by the couplings.

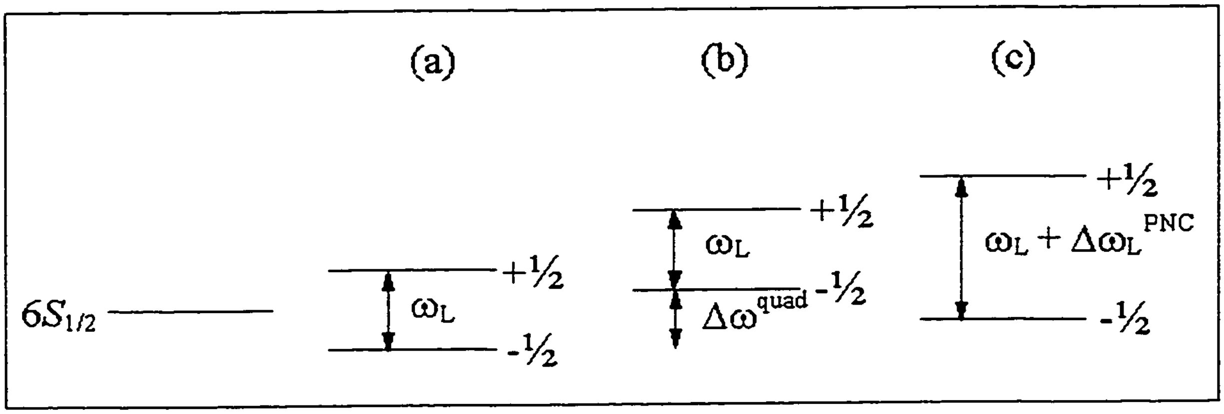

Figure 3.3: Diagram distinguishing between the pure quadrupole and PNC-induced light shifts. In (a), a small magnetic field of ~ 10^{-4} G is applied to split the ground-state magnetic sublevels by 100-1k Hz. In (b) and (c) the two laser fields are applied to drive the quadrupole and PNC-dipole transitions. (b) If we visualize the effect of the pure quadrupole shift alone, we see that it has no effect on the Larmor precession frequency. (c) The PNC-dipole light shift changes the separation between the magnetic sublevels, changing the size of the Larmor precession frequency.

The very different dependencies of the two shifts on the same magnetic sublevels are depicted in Figure 3.3. Visualizing the pure quadrupole and PNC shifts separately, we can pinpoint the very different behaviors.

3.5.2 Larmor precession

An atom placed in a weak magnetic field will exhibit a set of equally spaced, magnetic sublevels separated by energies of $\hbar\omega_L$, where

$$\omega_L = g_J \mu_B \frac{B}{\hbar} \tag{3.41}$$

is the Larmor angular frequency, g_J is the Lande g factor, and μ_B is the Bohr magneton. The light shift $\Delta\omega_m^{\mathrm{PNC}}$ of the individual magnetic sublevels discussed in the preceding sections will alter the observed Larmor precession frequency when the quadrupole and PNC-dipole transitions are being driven;

$$\omega_L \rightarrow \omega_L + \Delta\omega_L^{\mathrm{PNC}}, \tag{3.42}$$

where we now tack on the subscript L and add the shift of each sublevel to represent the net effect on the Larmor frequency. The pure quadrupole shift will have no effect on the Larmor frequency because its value is m-independent, as stated in the previous section.

To drive these transitions, we apply a total electric field $\mathbf{E} = \mathbf{E}' + \mathbf{E}''$ where $\mathbf{E}'$ is designed to drive the PNC-dipole transition and $\mathbf{E}''$ is designed separately to drive the quadrupole transition. Substituting these fields into Equation 3.40, we can represent the total shift of the Larmor frequency as

$$\Delta\omega_L^{\mathrm{PNC}} = \eta\langle 2(\mathbf{E}' \cdot \nabla)\dot{\mathbf{E}}'' + \mathbf{E}' \times (\nabla \times \dot{\mathbf{E}}'')\rangle_t, \tag{3.43}$$

where

$$\eta \approx \frac{e a_0 \lambda^2 \mathcal{E}_{\mathrm{PNC}}}{2\pi h c}. \tag{3.44}$$

3.5.3 Size of the effect

Optimally, a large optical field with no gradient, $\mathbf{E}'$, drives $\mathcal{E}_{\mathrm{PNC}}$ and a much smaller optical field of pure gradient, $\mathbf{E}''$, drives the competing $\mathcal{E}_{\mathrm{quad}}$. To produce such a large field with no gradient, the antinode of a standing wave is chosen for $\mathbf{E}'$. The node of a smaller amplitude field will have a small gradient at the ion, which is the choice for $\mathbf{E}''$. See Figure 3.4 for a sketch of the standing-wave pattern. An example set of fields that will achieve the optimized goals is given by

$$\begin{aligned} \mathbf{E}' &= \hat{\mathrm{x}} E_0' \cos kz, & (3.45) \\ \mathbf{E}'' &= i\hat{\mathrm{z}} E_0'' \sin kx, & (3.46) \end{aligned}$$

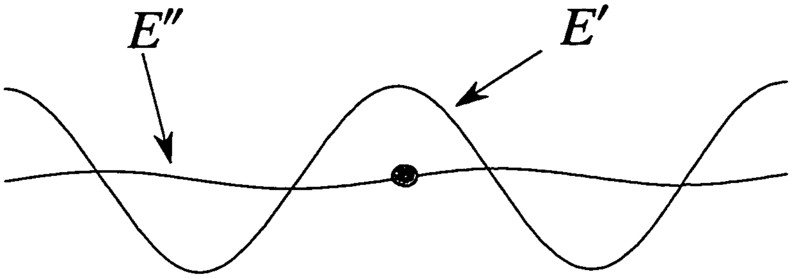

Figure 3.4: Sketch of the standing-wave field pattern for the PNC measurement. The ion (grey dot) resides at the antinode of the PNC-dipole $\mathbf{E}'$ standing wave and at the node of the quadrupole $\mathbf{E}''$ standing wave.

where the zero subscript refers to the value of the respective field at the ion, with the ion located at $\mathbf{r} = 0$. The two fields are linearly polarized and propagate in perpendicular directions. They are 90° out of phase with each other spatially to achieve the desired antinode/node pattern and temporally to make the observable $\Omega^{\mathrm{PNC}*}_{m'm}\Omega^{\mathrm{quad}}_{m'm}$ real (recall that $\Omega^{\mathrm{PNC}}_{m'm}$ is imaginary).

With these fields and using a calculation of $\mathcal{E}_{\mathrm{PNC}}$ by Das [MSD95] made in $^{137}\mathrm{Ba}^+$, we estimate that the Larmor precession frequency is shifted by

$$\begin{aligned}
\Delta\omega_L^{\mathrm{PNC}} &= \frac{\mathcal{E}_{\mathrm{PNC}} E_0{}'}{\hbar}, && (3.47)\\
E1_1(J_i = 1/2, J_f = 3/2) &= i0.515\ ea_0 Q_W \times 10^{-12}, && (3.48)\\
&\rightarrow\ \mathcal{E}_{\mathrm{PNC}} = 4.0\ ea_0 \times 10^{-11}, && (3.49)\\
\frac{\Delta\omega_L^{\mathrm{PNC}}}{2\pi} &\approx 2\ \mathrm{Hz}, && (3.50)
\end{aligned}$$

using the expected value $E_0' = 10^4$ V/cm. Figure 3.5 shows this shift added to ω_L produced with an applied magnetic field of $\sim 10^{-4}$ Gauss.

Note that to extract $\mathcal{E}_{\mathrm{PNC}}$ from the measured quantity, E_0' must be known as precisely as the measured shift itself. To accomplish this, an independent calibration measurement involving E_0' will be made involving precisely calculable parity-conserving

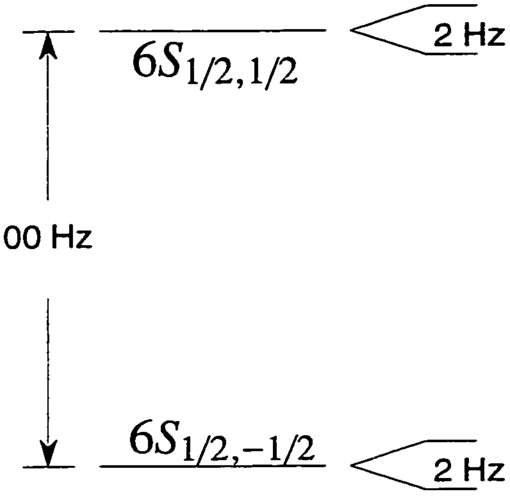

Figure 3.5: Diagram showing the level splitting due to PNC added to that due to the applied external magnetic field of $\sim 10^{-4}$ Gauss.

light shifts of the same Ba^+ ion.

3.5.4 The measurement

The measurement cycle from which the value for $\Delta\omega_L^{\mathrm{PNC}}$ will be extracted is described as follows and summarized in Figure 3.6. An external, static magnetic field of $\sim 10^{-4}$ G is applied in the z direction to create a small Zeeman splitting in the ground state. The ion is cooled and then prepared into a specific spin state of the ground state using a circularly polarized cooling-laser beam. For the sake of our discussion, assume that the ion is prepared in the $m_s = +1/2$ state. Both the cooling and cleanup beams are blocked, and the PNC and quadrupole standing-wave laser fields tuned to 2.05-μm are applied to drive the couplings. With laser fields applied to drive the transitions, $\Delta\omega_L^{\mathrm{PNC}}$ will then alter the Larmor precession frequency ω_L due to the applied field. A nearly resonant RF magnetic field is applied to drive $\Delta m_s = \pm 1$ Zeeman transitions

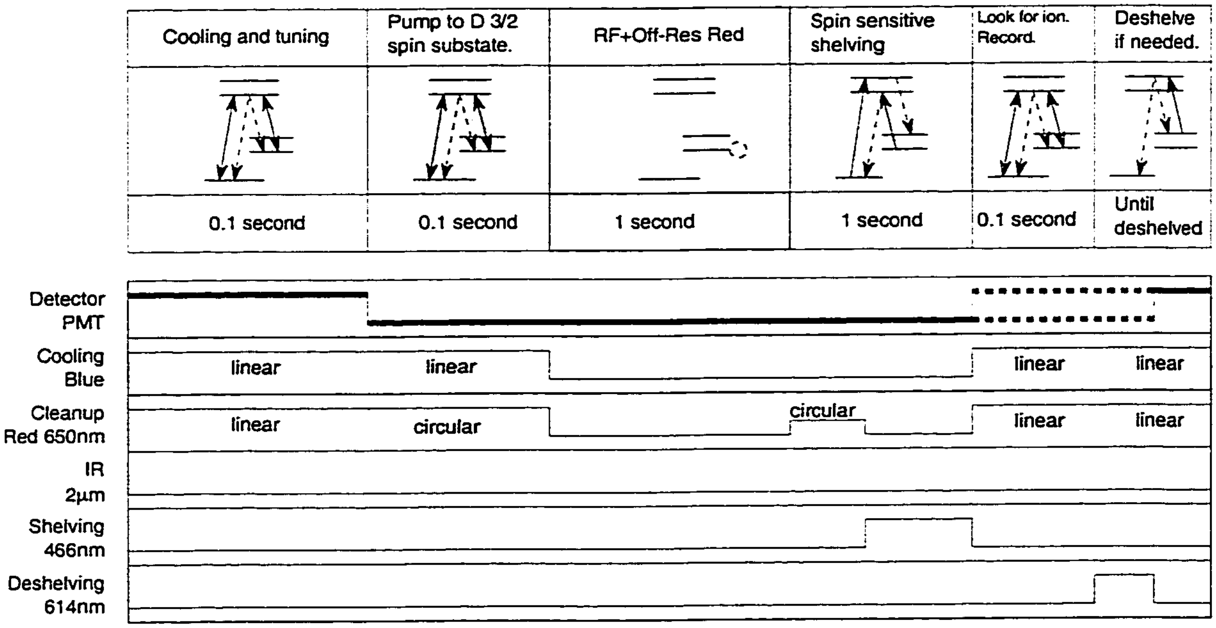

Figure 3.6: Measurement sequence used to determine the PNC light shift. This figure style is explained in Section 6.2.

at the same time. Then the 2.05-μm beams are blocked. Circularly polarized shelving laser light is used to selectively shelve the ion out of a particular spin state. In the case of our example, we shelve out of the $m_s = -1/2$ state. If the spin has made the Zeeman transition from the upper spin state, it will be shelved. Shelving will give us $\approx$ 50% detection efficiency of the final spin state. This efficiency rate could approach 100% using a circularly polarized shelving laser at 1.76 μm and π pulses. Finally, cooling beams are unblocked to check for the shelved ion, and the datum (shelved: yes or no) is recorded. This measurement cycle is repeated at the same and at different RF frequencies to map out the RF transition, from which the light shift can be determined.

3.6 Concluding remarks

The neutral current weak interaction can be determined in a single, trapped barium ion by measuring the resulting light shift in the ground-state magnetic sublevels. The size of this shift is characteristically small. But taking advantage of the features of single ion traps and its techniques, a very precise measurement of the light shift may be possible.

Chapter 4

APPARATUS

All experiments are performed on a single barium ion suspended in an ultra-high vacuum (UHV) environment by a confining RF-electric quadrupole trap. After an ion is trapped, lasers are used to cool the ion's motion. The trapped and cooled ion is manipulated by lasers and external fields to extract the desired information. The actual measurements are described in Chapter 6. The apparatus utilized for all measurements is described in this chapter. A photograph of the experiment is in Figure 4.1.

4.1 The trap

An ion trap most generally is a configuration of electric and magnetic fields that confines the motions of charged particles to a small region. Electric fields are produced by voltages applied to electrodes, and magnetic fields are applied remotely. The Paul trap used in the experiments presented in this thesis is an electric-only trap. According to Earnshaw's theorem (a result of Maxwell's equations), a charged particle cannot be held in stable equilibrium by electrostatic forces alone in charge-free space. The Paul trap overcomes this difficulty by employing an oscillating electric potential that is applied to the electrodes. Ideally the electrodes are hyperboloids of revolution about the z axis, which produce a three-dimensional trapping potential of axially symmetric quadrupole form, given by

$$V = \frac{V_0}{z_0^2}\left[z^2 - \frac{1}{2}(x^2 + y^2)\right]\cos\Omega t, \tag{4.1}$$

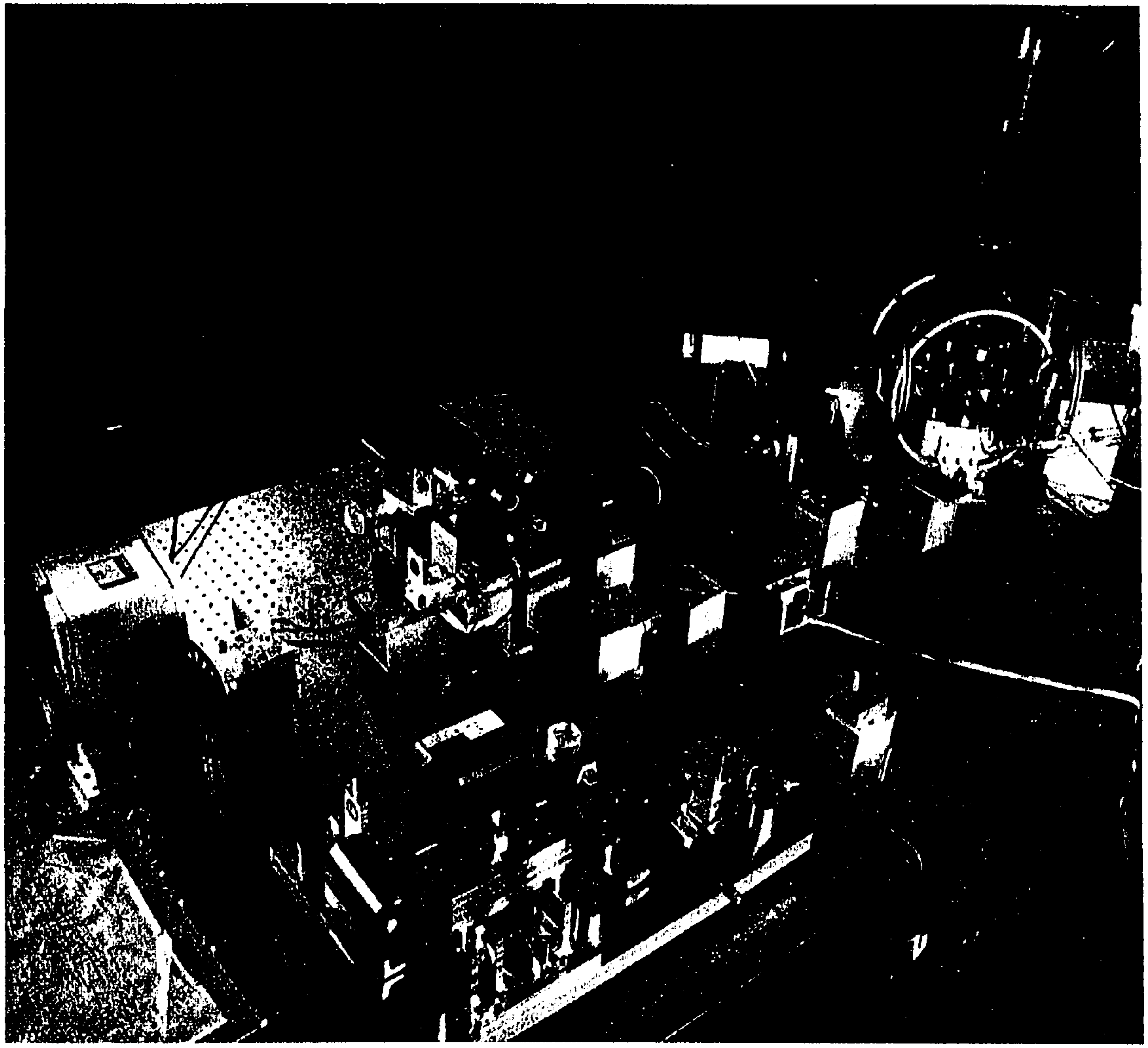

Figure 4.1: Photograph of the experimental apparatus.

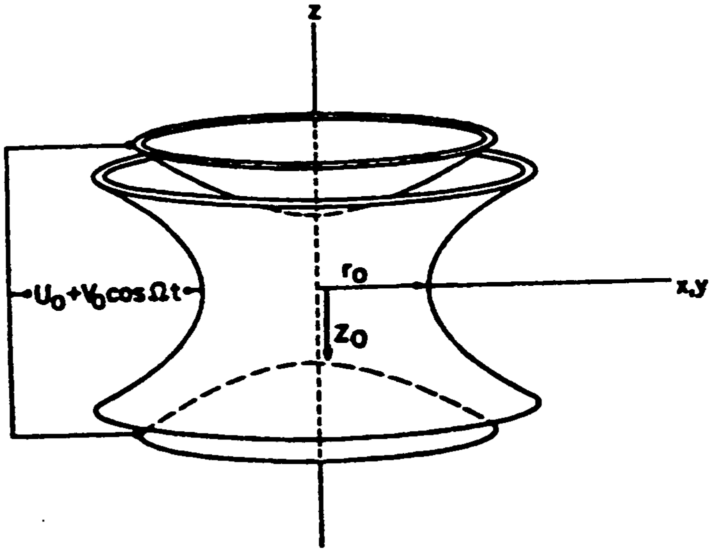

Figure 4.2: Hyperbolic electrode structure of the Paul trap [Wer85]. V_0 is defined in Equation 4.1. U_0 is a constant voltage that can be added to the oscillatory term.

where V_0 is the potential at the point $x = y = 0$ and $z = z_0$ that coincides with one of the electrodes. This electrode structure is illustrated in Figure 4.2.

In this trap, precise quadrupole fields exist over the entire spatial extent of the volume interior to the electrodes. At the trap center, the potential forms an oscillating saddle. The trap is stable in the axial direction and unstable in the radial plane for one half cycle and vice versa for the next half cycle. The average force in one period of the oscillating field is not necessarily zero but has some magnitude and is directed towards regions of weak electric field (towards the geometric center of the trap and away from the electrodes in the absence of external fields). At the trap center, there is no RF field and therefore no motion due to the oscillating field; a particle here can be at rest.

Ions do not settle down to the exact center, however. Instead, an ion follows a small orbit about the center and exhibits harmonic motion in three dimensions,

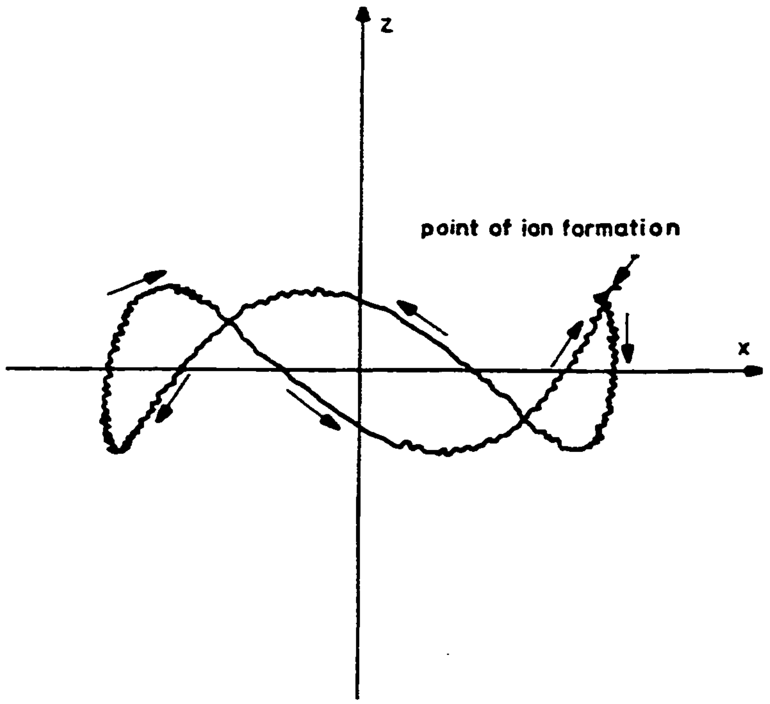

Figure 4.3: Calculated ion trajectory in a Paul trap. The projection of the three-dimensional ion orbit is onto the x-z plane [Wer85]. The frequencies of the motion depend on the physical parameters of the trap and on the frequency of the applied trapping field.

as shown in Figure 4.3. The resulting equations of motion in the axial and radial directions are Mathieu's equations and can be solved. (The x and y equations are exactly the same and therefore are collectively represented by an equation in the variable r.) The solution in each direction consists of a sum of components at angular frequencies that are linear combinations of $\omega_{r,z}$ and Ω, where the $\omega_{r,z}$ depend on the physical parameters of the trap, according to

$$\begin{aligned} \omega_z &= \frac{\sqrt{2}eV_0}{M\Omega z_0^2}, && (4.2) \\ 2\omega_r &= \omega_z. && (4.3) \end{aligned}$$

The frequency Ω is the frequency of the applied electric potential.

Stable motion is only possible in a given trap for certain ranges of applied oscillating voltages, defining stability regions. The stability parameter α is defined as the following ratio of frequencies,

$$\alpha \equiv \frac{\Omega}{\omega_z}, \tag{4.4}$$

and must be larger than 2. For for our trap α is between 3 and 10. In this range, the total motion is approximated by a slow secular harmonic oscillation at frequencies $\omega_{z,r}$ with a superimposed speedy micromotion at the drive frequency Ω of smaller amplitude.

The time-varying inhomogeneous electric fields of the trap produce a pseudopotential well in which the ion moves. The depth of this well is defined as the difference between the pseudopotential at the trap center and the electrodes, given by

$$\begin{aligned} \Psi(\bar{z}) &= \frac{eE_0^2(\bar{z})}{4M\Omega^2} = \frac{eV_0^2}{M\Omega^2 z_0^2}, && (4.5) \\ \Psi(\bar{r}) &= \frac{eV_0^2 r_0^2}{4M\Omega^2 z_0^4}. && (4.6) \end{aligned}$$

The well depth in the axial and radial directions should be the same, yielding the condition that $r_0 = \sqrt{2}z_0$.

For tight confinement of ions in deep potential wells, high frequencies Ω and high voltages V_0 are used in physically small traps. Conveniently, it has been shown [Maj62] that it is not necessary to use ideally shaped electrodes, allowing smaller shapes that are easier to manufacture and allow easy laser beam access. Any electrode shape that produces a local minimum of the oscillating electric field will trap ions, and generally these electrodes consist of a ring and/or end caps.

The Paul-Straubel trap used exclusively in the experiments discussed in this thesis is a very small ring electrode supported by leads with distant and grounded end caps also called compensation plates. This is an example of an unconventional trap, which has several features that distinguish it from a conventional (ideal) trap [YND91, YN95]. First, a higher voltage is required in an unconventional trap to achieve the same trapping strength (well depth) as a conventional trap of the same size. This is because without the endcaps close to the ring, most of the voltage drop occurs not between the ring electrode and the ring center but in the region between the ring and the distant ground. Equivalently, the effective depth of the pseudopotential is reduced as the electrode shape varies from ideal. Being simpler to construct, an unconventional trap wins back this voltage loss factor by easily being much smaller in size. Second, nonvanishing terms of higher order in the potential cause anharmonicity in the ion's secular motion. For a single, laser-cooled ion this is not a problem because the ion resides very near the trap center where the higher-order terms of the potential contribute minimally to the ion's motion. Third, other nearby electrodes can alter the trapping field. Most notably, the long supporting leads of a ring trap will break the azimuthal symmetry that caused the two radial secular frequencies to be degenerate. For traps using laser cooling, this fact has a serendipitous consequence. It allows efficient laser cooling in all three directions with a single laser beam that would otherwise not be possible with exactly degenerate secular frequencies (see Section 4.2

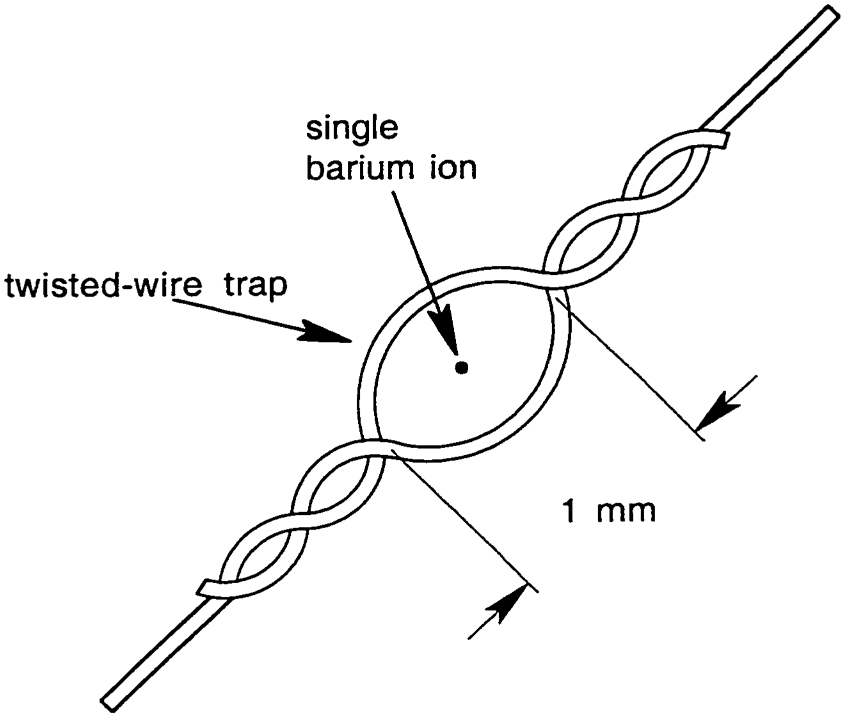

Figure 4.4: Sketch of a twisted-wire trap from [Bur95]. The traps used in this thesis were constructed with 125-μm diameter tantalum wire twisted around a 415-μm diameter wire to form the central hole.

for a discussion of laser cooling). Finally, the ring and distant end cap construction allows for easy access for all laser beams and for detection of the ion's fluorescence.

An additional feature of the type of miniature Paul-Straubel trap used here is the fact that it is heatable [YND91]. It is possible to pass a current through a ring trap with two leads, resistively heating the trap electrode. At a sufficiently high temperature, this heating drives off impurities like oxides and barium. These deposits could otherwise create patch effects and contact potentials that would shift the equilibrium point in the trap away from the center to where the RF is nonzero, increasing the amplitude of the trapped ion's micromotion.

The trap used in these experiments is a twisted-wire trap with grounded end caps positioned parallel to the plane containing the trap hole and located far ($\sim 1/2$ cm) from the trap to allow adequate laser beam access. The wire is 125-μm diameter tantalum twisted around a 415-μm diameter circular form. Figure 4.4 includes a sketch of this type of trap. The end caps are thin plates of stainless-steel shim stock, each ~ 1 cm^2. One or both leads of the twisted-wire trap are connected to the RF source operating at $\Omega/2\pi \approx 30$ MHz. At this frequency, an RF voltage $V_0 = 600$ V is found to produce a well depth of a few eV and a secular frequency $\omega/2\pi$ of a few MHz. To achieve this well depth, an applied RF power of 5-15 W is necessary.

Only ions created inside the trap have any reasonable chance of getting to the trap well and starting on an orbit that will remain inside the trap, for true conservative forces. Barium ions are created from a gas of neutral barium that is ionized by electrons emitted from the stainless-steel oven metal or from a filament. These electrons are accelerated and focused into the trap by the applied RF voltage. Generally the RF power is increased to 10 or more Watts during initial trapping and alignment procedures. Once an ion (or ions) is trapped, the trapping power can be incrementally reduced to 5 W or less, if desired, for the anticipated experiment.

4.2 Laser cooling

Uncooled ions in traps have temperatures of 10,000s K (few eV). There are several reasons to cool below this temperature. Storage times of cooled ions are increased because hot ions with their larger spatial extent are more likely to be lost from the trap. A cold ion spends more time inside the tightly focused laser beams tuned close to resonance, increasing the number of scattered photons available for ion detection. Cooling can drastically reduce Doppler broadening. With sufficient cooling, the first-order Doppler effect is eliminated and the second-order (relativistic) Doppler effect is reduced, as described in this section.

Laser beams are used to cool the ion's motion after the ion is trapped with the Doppler cooling technique [WD75, HS75]. This technique can be described using a photon-atom energy picture. A photon carries energy that can be imparted to the ion. If the photon is tuned to a frequency slightly below the resonant frequency of the ion, then the ion will preferentially absorb the photon when the ion is traveling towards the photon, Doppler tuning the photon into resonance. The subsequent re-emission of the photon by the ion will be in a random direction and will contain on average the full energy of the resonant frequency, reducing the total energy of the ion. In the lab frame, the re-emitted photon has more energy than the incident photon and therefore the kinetic energy of the ion must be reduced by the energy difference. After several absorption and emission cycles, the ion's motion is appreciably cooled. For an ion to be cooled efficiently, both radial and axial motions must be reduced by this method. The propagation direction of the cooling beam is chosen to couple to all three orthogonal axes of the trap. The maximum orbit of the cooled ion's motion is typically < 0.1 μm corresponding to a temperature of ≈ 1 mK. The minimum energy achievable in Doppler laser cooling is estimated to be

$$\langle E_{\mathrm{min}} \rangle = \frac{\hbar\Gamma}{4},$$

where Γ is the natural linewidth of the cooling transition and when the laser is set at a frequency $\Gamma/2$ below the resonance [WD75, WI79]. A minimum temperature T can then be estimated from the equipartition theorem,

$$\frac{1}{2}k_B T = \frac{\hbar\Gamma}{4}. \tag{4.7}$$

An ion remains trapped for several weeks with periodic cooling.

Specifically in Ba$^+$, cooling is accomplished on the transition from the $6S_{1/2}$ ground state to the $6P_{1/2}$ excited state, which is electric-dipole allowed (see Figure 4.5). This transition is excited by a blue laser detuned to the cooling side ~ 100 MHz away

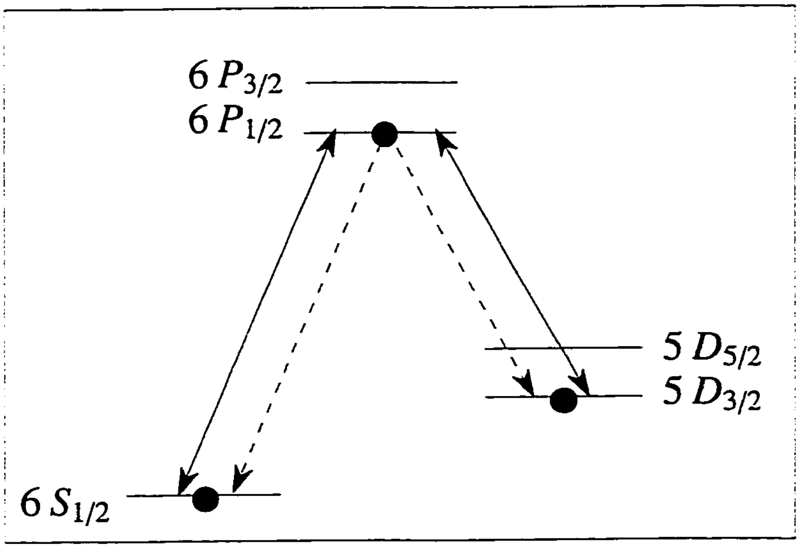

Figure 4.5: Energy-level diagram for Ba$^+$ showing the cooling cycle. Laser cooling occurs on the $6S_{1/2}$ to $6P_{1/2}$ transition. The clean-up beam excites the valence electron out of the $5D_{3/2}$ state into the $6P_{1/2}$ state.

from the 493-nm resonance. A second laser is required to cool barium efficiently. An electron excited to the $6P_{1/2}$ state can decay into the $6S_{1/2}$ ground state or the metastable (tens of seconds) $5D_{3/2}$ state. A red clean-up laser connects the $6P_{1/2}$ state to the $5D_{3/2}$ state, which is also a dipole-allowed transition. The purpose of the clean-up beam is to pump the ion out of the long-lived $5D_{3/2}$ state so that the ion can continue to be cooled by the blue beam.

The applied RF voltage will create frequency sidebands on the ion's motion. The Doppler effect in an ion oscillating in a trap results in an unshifted carrier frequency with sidebands spaced at the oscillation frequency ω. Under strong laser cooling, the ion resides very near the trap center and the sideband amplitudes approach zero, leaving just the unshifted carrier frequency. This is called the Lamb-Dicke regime, and it occurs when the oscillation amplitude is much less than $\lambda/2\pi$ of the laser light used for cooling [TDHP+97], leading to the elimination of the first-order Doppler effect.

4.3 Ion signal

An ion in the trap is detected by the 493-nm photons that the ion scatters during the cooling process. Light collection is oriented perpendicular to the propagation direction of the blue cooling laser to minimize its contributions to the ion signal. One might expect a small spectroscopic signal from a single ion, but it is possible to obtain quite a large signal due to the unique features of ion traps. The spontaneous decay rate of the cooling transition is 10^8 s^{-1}. At most 10^7 photons are absorbed and re-emitted by the ion interacting with the laser beam operating at the saturation intensity of the transition. The photon-counting system has a counting efficiency of ~ 0.001, allowing ion counts up to 10^4 photons/s. In practice we record 3000-4000 cps maximum for a single ion. Figure 4.6 shows the result of an typical photon-counting experiment.

4.3.1 Light-collection system: physical description

Detection of the scattered blue photons is accomplished with a photomultiplier tube (PMT) chosen specifically for high sensitivity and low dark currents at 493 nm.[1] The PMT is preceded by an interference filter (centered at 500 nm with a width of 20 nm), a small pinhole (100 μm), and a 50-mm camera lens. The center of the trap, where trapped ions are expected to be, is enlarged and imaged onto the pinhole by the camera lens.

A small green LED is mounted in the space above the pinhole. When lit, it shines through the pinhole to illuminate it. A microscope eyepiece is mounted at 45° to the

---

[1] Hamamatsu Model HR464.

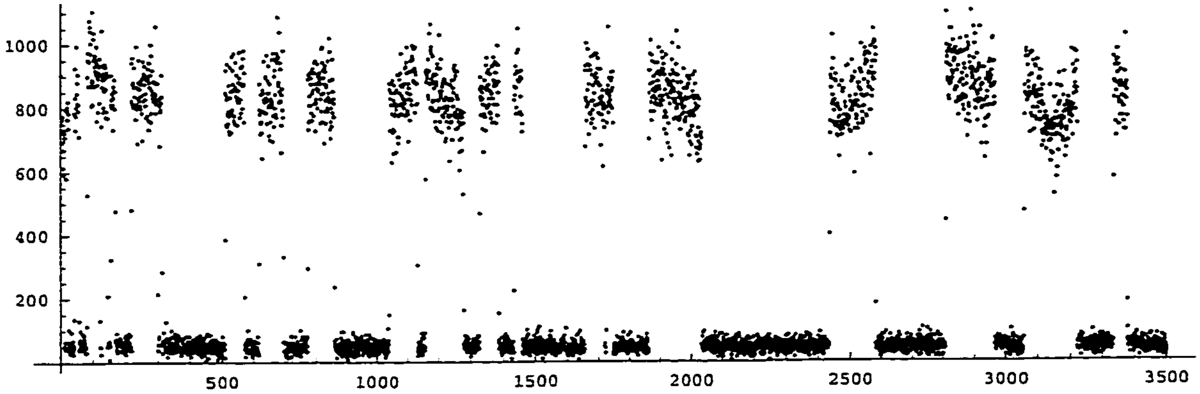

Figure 4.6: Real-time read out of photons/s scattered by a trapped ion exposed to blue (493-nm) and red (650-nm) radiation as it cycles among the $6S_{1/2} \leftrightarrow 6P_{1/2} \leftrightarrow 5D_{3/2}$ levels. The average number of photons per second collected in this example is 900. The ion generating the figure is also exposed to shelving light (discussed in Sections 4.7.1 and 6.1), resulting in the quantum jumps observed in the signal when the ion makes a transition to the metastable $5D_{5/2}$ level. From the number of these quantum-jump levels, we can count a single ion in this trap.

tube-assembly axis (see Figure 4.7). A small, flat mirror is fixed at the bottom end of the eyepiece tube with visual access to the interior of the tube assembly. It allows one to see the pinhole, especially when the green light is shining through it. This setup is important for the initial alignment of the light-collection system over the trap. The entire assembly is housed in a light-tight metal housing that is painted matte black inside and includes magnetic shielding around the PMT.

The position of the camera lens above the trap and the position of the pinhole above the lens are variable. The entire assembly moves via a precision, three-axis stage.[2] A rail that supports the camera lens and light-tight bellows attaches to this stage. Motion on the rail itself allows for an additional but coarse vertical degree of freedom.

---

[2] Newport model 460A-XYZ with SM-13 actuators.

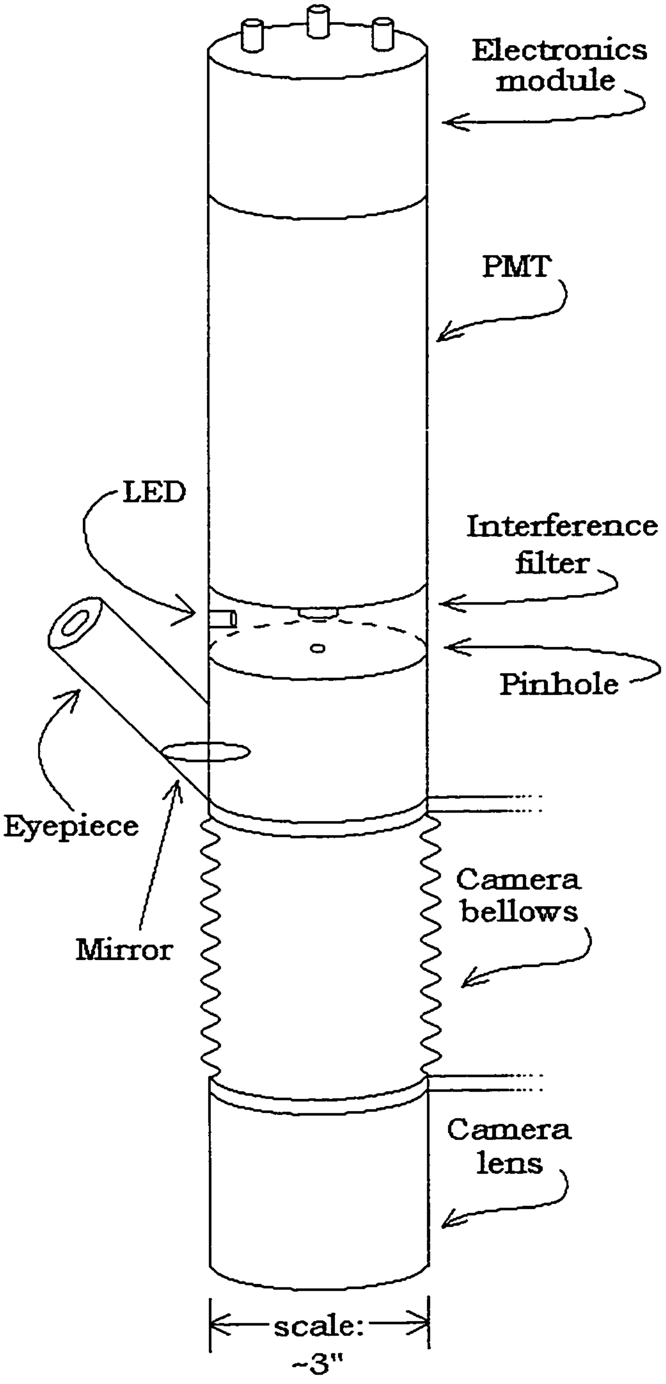

Figure 4.7: Sketch of the light-collection system.

4.3.2 Electronics modules

On top of the PMT itself is a cylindrical module that houses an electrical connector socket for the PMT, including a voltage-divider circuit, HV power input for PMT operation, and filter capacitors and connections to the anode of the PMT to collect the output current signal. Power input to the LED also enters through this module. The light intensity is sufficiently low that incident photons on the PMT's photocathode appear as discrete pulses on the cathode output. A discriminator that creates a logic pulse when the photon pulse crosses some preset threshold is contained in a separate box and sends the pulses to the computer for counting and display.

4.3.3 Alignment procedures

During the initial horizontal alignment procedure, the trap hole is imaged onto the pinhole and centered. The trap can be illuminated in one of several ways to aid this step. Hot filaments inside the vacuum chamber that are positioned directly below the trap cast a shadow of the trap up onto the plane of the pinhole. The center of this shadow is roughly aligned to coincide with the pinhole. Note that the ion is not guaranteed to be at the geometric center of the trap if some stray DC electric field exists.

The trap itself will radiate visible light when it is resistively heated with a current of about 4-8 A. This light can be imaged onto the pinhole and used to align the collection system over the trap. However, the trap wires expand when hot to produce appreciable movement of the whole trap, making this procedure less useful than the shadow method.

Other bright, general lighting from room lights, flashlight, and filament glow from the vacuum gauge can sufficiently illuminate the trap to image it onto the pinhole and to make it visible through the eyepiece.

The lasers can also be used for horizontal alignment. When the beams are aimed at the various edges of the trap-hole wire, the laser light reflects up onto the pinhole where it is visible through the eyepiece. Noting the micrometer positions corresponding to each visible edge, the collection system can be centered over the trap.

Finer alignment steps utilize the PMT and the ion signal. With all bright lights like the green LED and filaments extinguished, the laser beams that have been focused tightly to pass completely inside the trap hole can be swept across the trap. Photon-counting spikes will occur at the edges of the trap hole when laser light is reflected up into the PMT. The PMT is then roughly centered between these maxima. The same cautions that this will not be the exact center of the trap apply here. But it is a reasonable starting point.

Vertical alignment of the light collection system is sensitive and therefore important. Coarse vertical alignment involves focusing the trap shadow, however it is created, onto the pinhole. Finer vertical adjustments use the laser beams in a similar manner to the method described for the horizontal alignment procedure. The laser beams are aimed at each trap edge in opposite-side pairs. The pinpoint of light is focused by adjusting the vertical locations of the pinhole and the camera lens. This procedure is repeated with the lasers aimed at the opposite edge, which is located in a different horizontal plane. In each case, the z-axis micrometer reading on the actuator is noted, and the average of the two locations is used to determine the initial placement in the z direction.

During trapping, all of the finer adjustments will be tweaked when searching for the trapped ion signal and also once an ion is found to maximize the ion signal.

4.3.4 Possible improvements

Stability of the heavy light-collection assembly that is secured via the bellows rail to a single, three-dimensional, translation stage was originally questionable. We have been completely successful with this design. Reduction of hysteresis and creep in this particular stage would be desirable and may eventually require a better translation stage. It may be desirable to orient the system horizontally.

4.4 Trapping systems

Two different vacuum systems and trap headers were used in the series of experiments presented in this thesis. It is expected that the final measurement will require an as-yet-not-designed system. The known flaws in the two existing systems that must be overcome in the final system will be discussed at the end of each description.

4.4.1 Classic system

The first system built was designed specifically to accommodate a single mirror inside the vacuum chamber with the purpose of testing the stability of a standing wave created with the red laser beam. While the priority of this test has fallen and therefore has not yet been made, much has been learned from it about the difficulties of putting such a mirror near the trap. These problems will be discussed later in this section.

The trapping chamber is based on a 6-inch, 304 stainless-steel pipe with 6-inch top and bottom knife-edge flanges. Eight 2-3/4-inch flanges extend radially outward around the 6-inch cylinder. A mechanical drawing of the custom-built chamber is shown in Figure 4.8. The top 6-inch flange hosts a large, custom-built, re-entrant window for positioning the light-collection system as close as possible to the trapped ion. The bottom flange holds a 6-inch blank with electrical feedthroughs welded into drilled through holes. These electrical feedthroughs hold the trapping elements.

Drilled and tapped interior holes are used for mounting the trap hardware. A photograph of the Classic header with all trapping elements, the trap, and the mirror mount is shown in Figure 4.9. These pieces are described in the next section. The eight smaller flanges are used as indicated in Figure 4.10. The laser-entry windows are angled down at roughly 15° to minimize the amount of reflected light feeding back to the diode lasers. (The red laser can be particularly sensitive to this feedback.) Standard 2-3/4-inch, flat windows are used on all smaller flanges, as indicated in Figure 4.10.

Power feedthrough elements

Two 10-pin power feedthroughs[3] provide electrical power and physically hold all auxiliary trapping elements including the compensation plates. The conducting pins are 0.056-inch Alumel pins that are slightly flexible but generally fixed and strong. All of the following elements are mounted by crimp-type Alumel connectors.[4]

A single, high-voltage, 2-pin power feedthrough is used to conduct trap voltages into the vacuum. These pins serve no structural purpose and are quite flexible. In-line barrel connectors of BeCu[5] are used inside and out to connect the copper pins to the trap leads inside and to the trap circuit outside the vacuum. Teflon-coated wire is used outside the vacuum to carry the RF signal because ordinary hook-up wire insulators and coatings absorb RF power readily and will melt.

Care is taken to avoid electrically shorting the feedthrough pins inside the vacuum via conductive barium coatings that may appear on the header once the ovens are fired. Small, glass mushrooms are constructed from glass tubing whose inner diameter

---

[3] ISI part number 9421002, 10 Amp-per-pin, 700-Volt capacity.

[4] ISI part number 9923014.

[5] ISI part number 9924006.

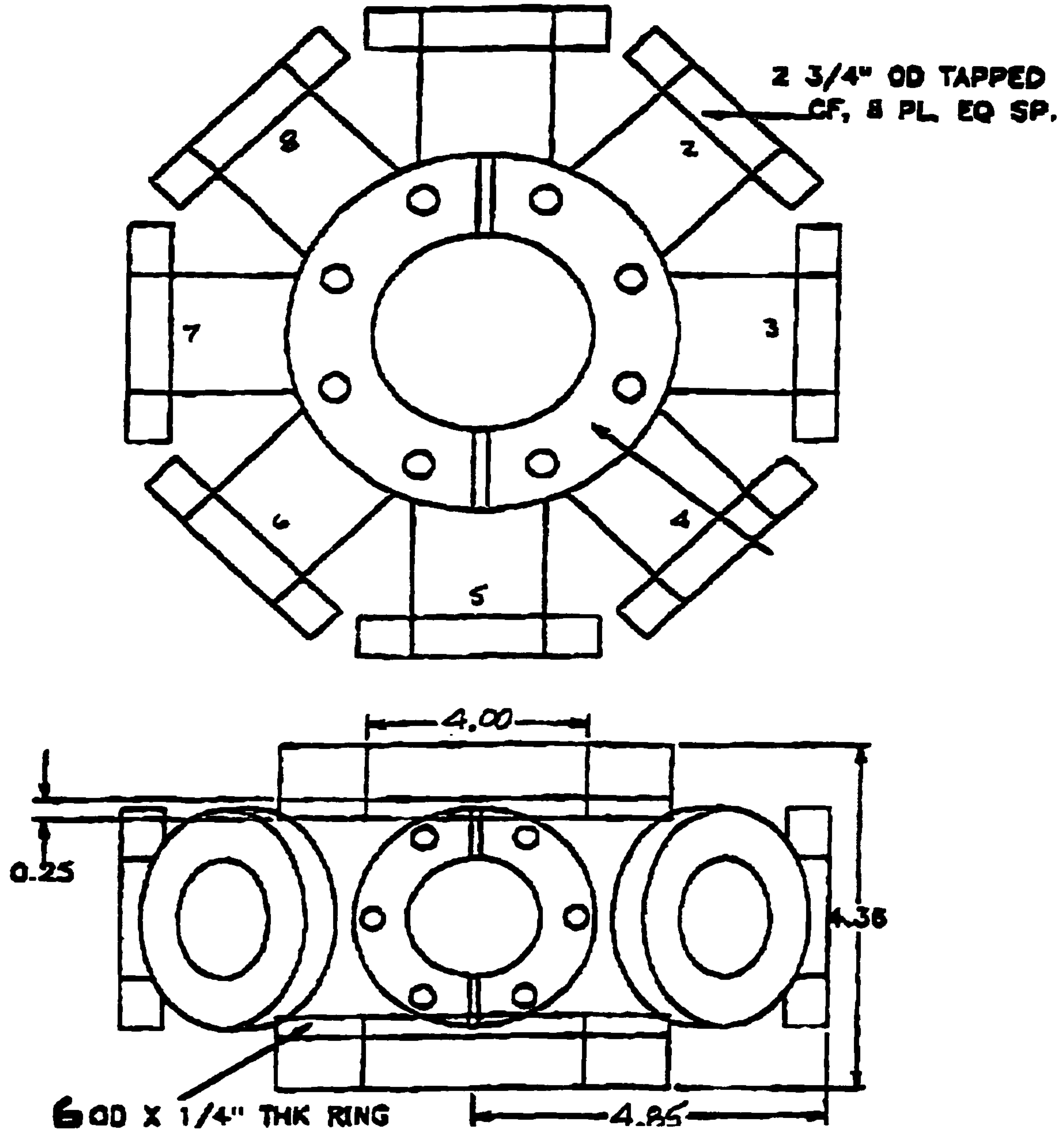

Figure 4.8: Classic system main chamber design.

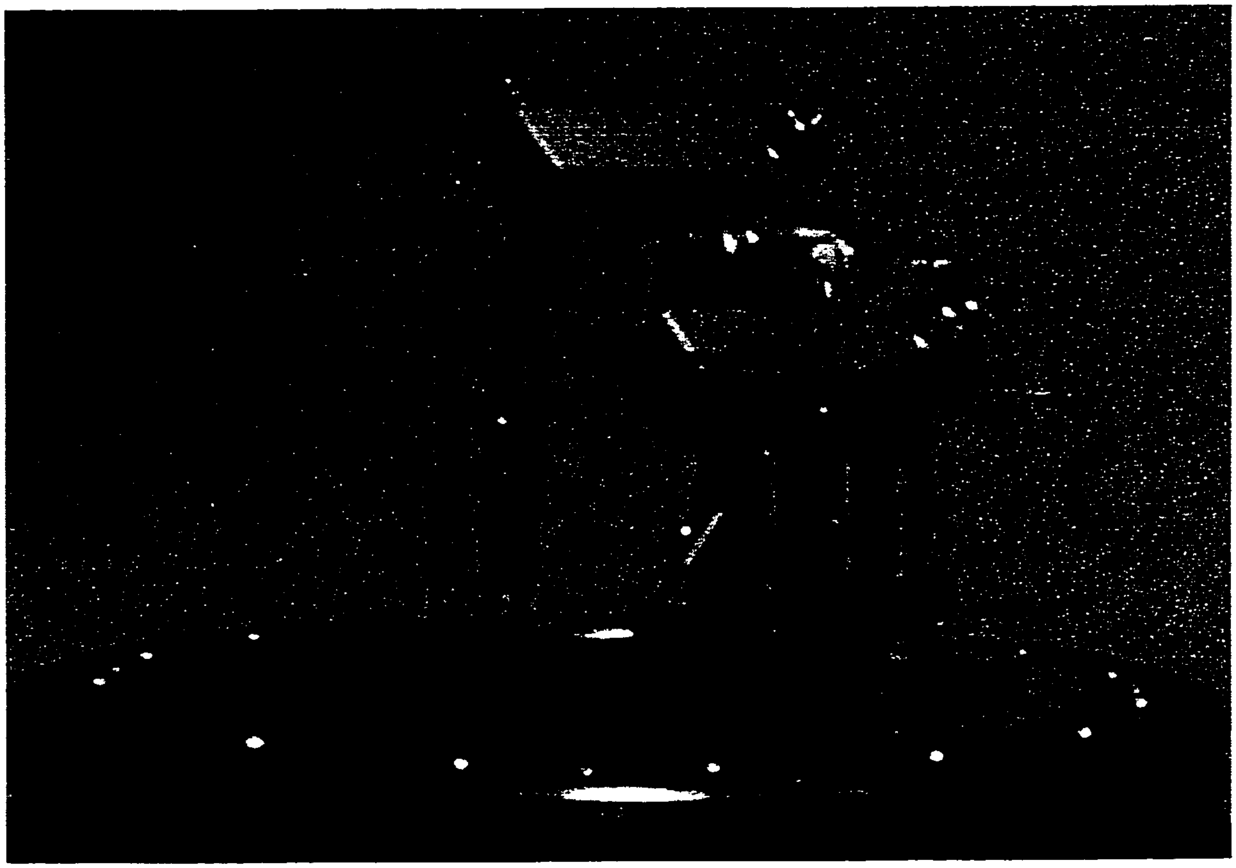

Figure 4.9: Photograph of the Classic system trap header. For scaling, note that the flange is 6 inches in diameter.

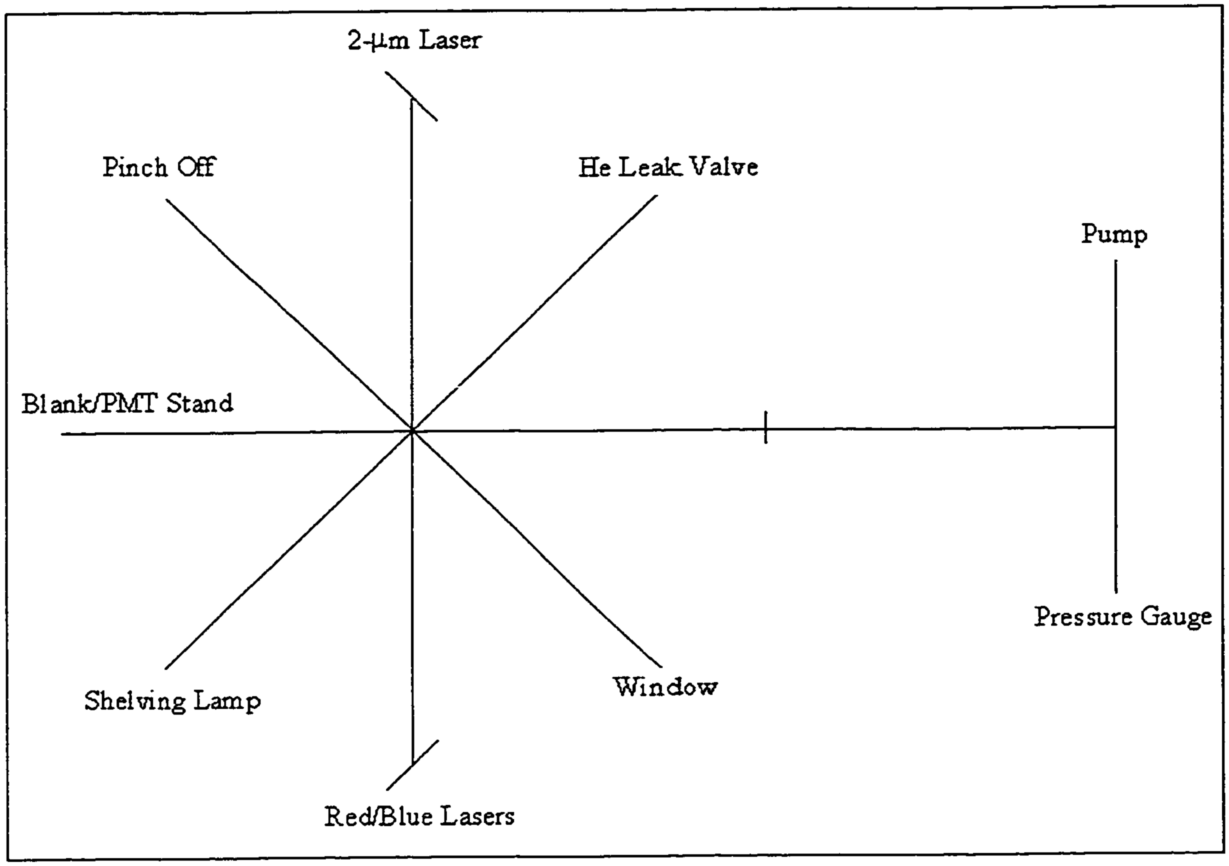

Figure 4.10: Beam arrangement diagram for the Classic system.

allows the mushrooms to slide freely over the feedthrough pins. The mushroom end is melted glass that bowls out into an umbrella cap or head. The shadow of the mushroom head when placed at the bottom of each feedthrough pin prevents barium coatings from creating complete conducting paths between pins or to the chamber.

Trap holder and electrical connections

A U-shaped piece cut from a solid hunk of 1-cm thick Zerodur[6] holds the trap electrodes and mirror assembly. It is coated by evaporation with copper because Zerodur is a very good insulator that can hold massive charge accumulations and thus create large DC electric fields that will move the trapping center far from the geometric center of the trap hole. Certain areas are not coated because they are in direct contact with other conducting pieces that will not be at the ground potential of the copper coating. The Zerodur piece can be seen in Figure 4.9. The Zerodur piece is firmly held under spring tension at 45° to the horizontal via custom stainless-steel legs and feet.

Tungsten rods (diameter 0.626 inch) are forced through hot Pyrex to create an insulating layer between the rod and the copper-coated Zerodur. The Pyrex also bowls out to act as a self-centering stopper. These rods slip through drilled holes in the Zerodur arms. The trap is the twisted-wire trap described in Section 4.1 and illustrated in Figure 4.4. The long twisted ends are spot welded directly to the rods. One rod is longer than the other to accommodate a short spring made of Inconel[7] and positioned between the Zerodur and the Pyrex pieces. The spring keeps the straight trap under tension as it expands when hot. The tension is small to avoid

---

[6] Zerodur is a nonmagnetic ceramic glass known and chosen for its extremely low thermal expansion coefficient. It is available from Schott Glass and can be machined with diamond cutters.

[7] Inconel is a high-temperature spring material that can survive the maximum bake-out temperatures.

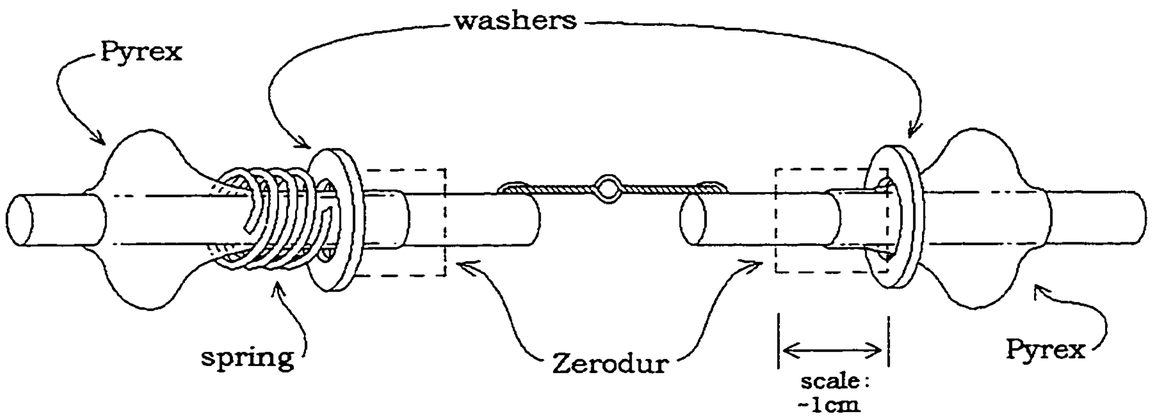

Figure 4.11: Sketch of the trap assembly.

stretching the hole into nonexistence. Thermal cycling of a twisted-wire trap to clean off deposited barium and other junk will over time cause the trap to warp appreciably if some tension is not applied.

Tantalum wires are coiled tightly around the ends of the rods and spot welded into place. These wires then attach via in-line barrel connectors to the copper feedthrough wires for RF voltage input. The trap assembly is sketched in Figure 4.11.

Mirror assembly

The mirror "used" thus far is a small (~ 1-cm diameter) flat mirror gold-coated to reflect both 2-μm and 650-nm light. An aluminum mirror holder is machined to hold the mirror snuggly and yet accommodate thermal expansion during baking. Small tabs screw into the front of mirror holder and cantilever over the mirror to press fit it into the holder. A hollow, ceramic piezoelectric transducer (PZT)[8] fits snuggly under an overhanging lip that protrudes from the back of the mirror holder. The other end

---

[8] Staveley Sensors, NDT Technologies, Inc., EBL #2, 0.750-inch outer diameter × 0.025-inch wide × 1.25-inch long with appropriate silver-plated electrodes.

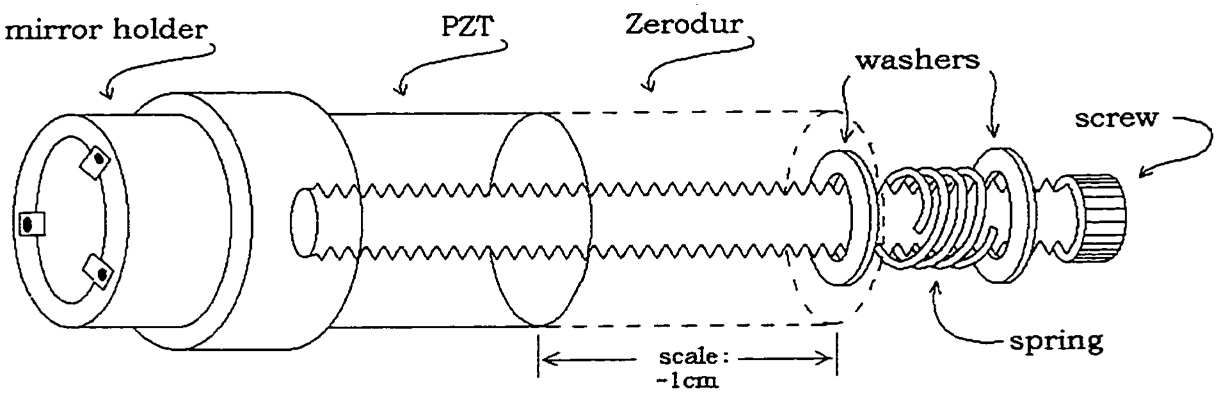

Figure 4.12: Sketch of the mirror holder assembly.

of the PZT fits into a circular groove created by a diamond cutter. A smaller through hole is cut into the center of the groove to accommodate a stainless steel screw. The screw passes through a washer, a spring, another washer, the Zerodur, and PZT to finally screw into a threaded hole in the back of the mirror holder. The two washers keep the spring from slipping over the screw head and from chipping the Zerodur. The PZT therefore acts under the tension of the spring. Figure 4.12 contains a sketch of the mirror assembly. The mirror front is $\sim$ 1 cm from the trap.

The high voltage electrode of the PZT is deposited on the inside walls and wraps around the back end. A wire is pressed into the uncoated groove drilled into the Zerodur and then exits through a notch in the side of the Zerodur. This wire is connected to a feedthrough pin via an in-line barrel connector.

Known flaws

The ability of the Zerodur to accumulate charge was an unknown factor that prevented our first trapping efforts from being successful. The location and size of the charge accumulation was found under the following conditions. With the RF power set to 10-15 Watts, a "blue flame" of fluorescing barium ions was observed by eye exiting the hot ovens. Instead of following the straight-line path directly to the trap center, the blue flame turned 90° and slammed into the Zerodur arm, missing the trap center by at least a cm. The copper coating on the Zerodur has eliminated this problem. We now use the blue flame as a diagnostic tool and can create it at will. It is more clearly visible in the presence of a helium buffer gas.

Other insulators near the trap are a concern. For instance, the mirror may also accumulate charge, although the current mirror is gold coated and grounded through the mirror mount to the chamber.

The final PNC light shift measurement will require stringent control of any ambient magnetic fields. Shielding will be used extensively to reduce magnetic effects from materials in the room and building. Materials inside the shielding must be as nonmagnetic as possible. The chamber is made of standard 304 stainless steel, which has magnetic properties. A less magnetic chamber material may be necessary, like 316 stainless steel, OHFC copper, or glass. Most power feedthrough units use highly magnetic Kovar to seal insulators to the conducting materials. The conducting material itself, Alumel, is an aluminum-nickel alloy, which may also be magnetic. Different power feedthroughs and connectors may be necessary to reduce sufficiently the magnetic fields created inside the vacuum chamber.

4.4.2 System 97

The second working version of the trap system is based on a slightly modified 2-3/4-inch six-way cross. All trapping elements fit inside this much smaller vacuum volume. One arm of the cross is made as short as physically possible to bring the camera lens of the light collection system as close as possible to the trap. A mechanical sketch

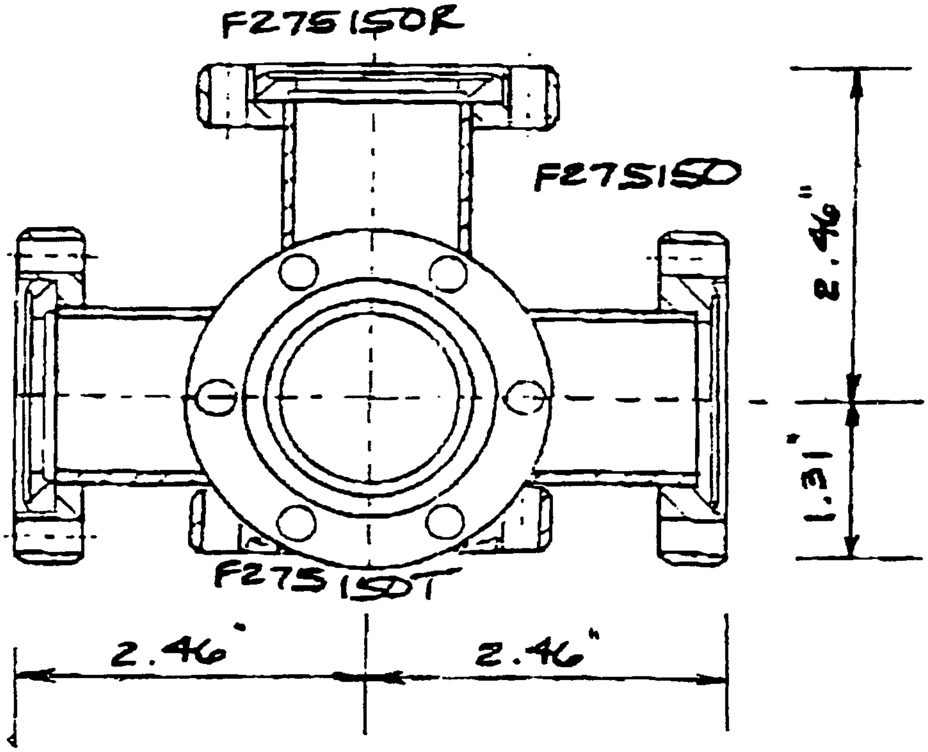

Figure 4.13: Mechanical sketch of the modified six-way cross vacuum chamber.

of the chamber is shown in Figure 4.13. Two power feedthrough units are located on perpendicular 2-3/4-inch flanges, the trap and compensation plates mounted on the side flange and all other elements mounted on the bottom flange. The trap and compensation plates are spot welded directly to the copper feedthrough pins.[9] This feedthrough unit is mounted on a 2-3/4-inch flange with six copper conductor pins capable of conducting a total of 30 A and handling up to 5000 V. Mild tension is applied to the trap by squeezing its copper pins together slightly when spot welding the second trap lead to the pin. The filaments, ovens, and anode are directly spot welded to the Alumel pins of the bottom flange.[10]

Light collection is vertical since all lasers enter and leave perpendicular to the flanges just mentioned. This also makes the two chambers completely interchangeable on the table without moving the lasers, focusing lenses, or the light collection system. No tilted input windows are used and have not posed any problems. A second, standard, six-way cross and vacuum tee accommodate all other auxiliary trap components. The flange arrangements are shown in Figure 4.14.

A mirror assembly that would theoretically fit inside this chamber has been proposed but not built. Its sketch is shown in Figure 4.15.

4.4.3 Vacuum preparation

A rigorous cleaning procedure closely followed is necessary to ensure that a low pressure system is possible. Any item that will be inside the vacuum chamber is cleaned in an ultra-sonic bath in turn with trichloroethylene, acetone, methanol, and de-ionized water. The pieces are allowed to dry completely after the tricholoroethylene and de-ionized water baths and remain wet after acetone and methanol baths. Gloves are

---

[9] ISI part number 9422158.

[10] ISI part number 9132005.

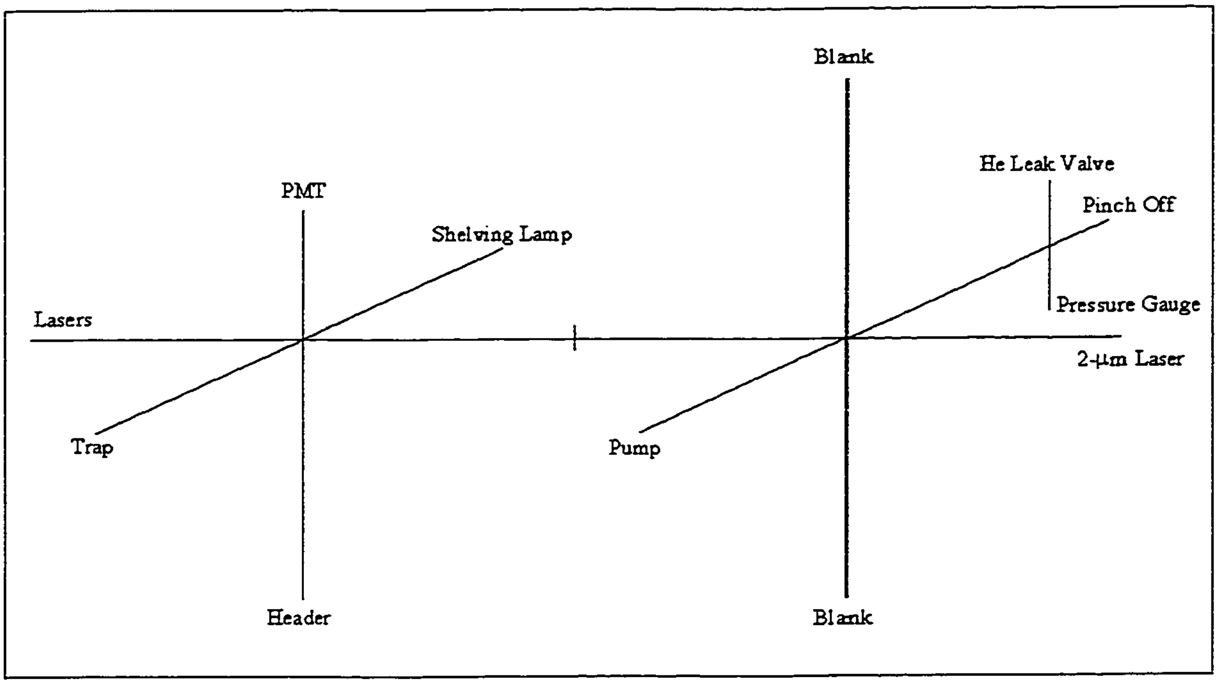

Figure 4.14: Beam arrangement in System 97.

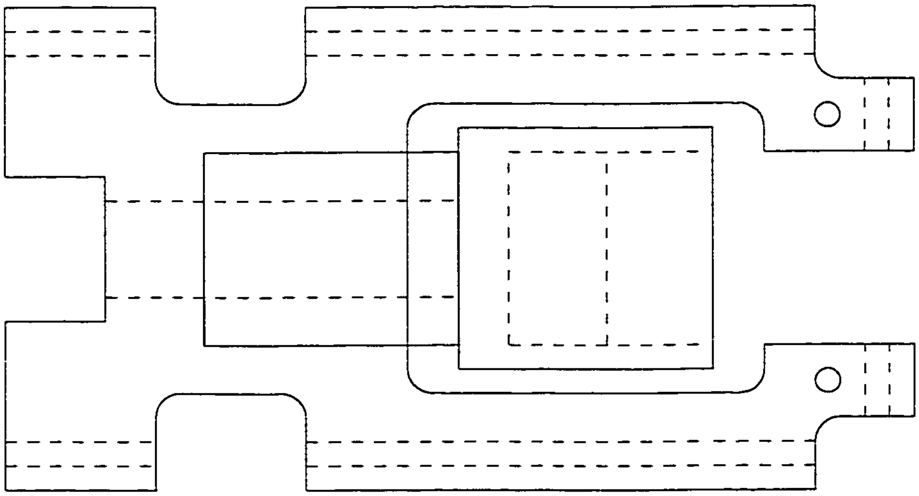

Figure 4.15: Proposed mirror assembly for System 97.

used to handle directly any pieces. Any tools that are used to work with the clean pieces are also wiped clean with solvents, rinsed with de-ionized water, and allowed to dry completely.

Consideration was made to eliminate any possible sources of virtual leaks inside the vacuum. All screw threads were filed off on one side to allow an escape path for gases trapped between the threads. Through holes were drilled whenever possible to again allow an escape path for trapped gases.

The UHV pressures are maintained by a 20 l/s Varian Triode sputter-ion pump. A separate vacuum bake-out system consisting of a cryopump and a 30-l/s ion pump is used to bring the vacuum down to 10^{-8} Torr before starting the smaller ion pump. Maximum bake temperatures are above 100°C. Once separated via a copper adapter from the roughing system, the 20 l/s pump runs continuously during trapping and all experiments. Pressures are measured using a Bayard-Alpert type, nude ionization gauge. Pressures in the mid 10^{-10} Torr range are typical under operating conditions.

The trap, filaments, and ovens are outgassed twice: once while connected to the bakeout system and again at lower pressures when detached from the bakeout system and after the 20-l/s pump has been working.

Some effort was made to remove the pump and its permanent magnet a reasonable maximum distance from the trap. Shielding with two to three layers of 1/16-inch μ-metal around the pump magnets has been added to further reduce stray magnetic fields.

A helium leak valve is attached to each system. Pure helium gas is leaked into the system by heating Quartz glass in the presence of helium. This is used to buffer cool barium ions for the purpose of trapping large clouds. A large cloud interacting with the red and blue laser beams will generate a correspondingly large scattered-photon signal that can be used to test a new or nonworking system or to align the laser beams or light-collection system. The ion pump does pump helium well; cloud trapping must be done with the pump off. Also, single-ion trapping can follow when the pump is restarted.

4.4.4 The trap voltage

The voltage applied to the trap electrodes is generated by a commercial RF oscillator at 25-32 MHz, amplified by a commercial RF amplifier to a few watts, and then stepped up in voltage by a custom circuit. Schematics of two circuits that will step up the voltage are shown in Figures 4.16 and 4.17. A few hundred volts are necessary for a reasonable trap well depth. It is important to impedance match within the custom circuit to maximize the high-voltage RF signal that appears on the trap electrodes. Two variable capacitors or a variable coil in the step-up circuits exist for this purpose. The variable capacitors are typically accessible from the outside for convenience. A Teflon-coated wire conducts the stepped-up voltage directly to the trap feedthrough.

RF signals can readily leak out of the cables, instruments, or connectors carrying it. Some care must be taken to minimize this leakage as it can interfere easily with other unrelated electronics like photon-counting and laser-locking systems. It is important to prevent the RF signal that has been successfully applied to the trap electrodes from being picked up by the various antennae inside the vacuum (filaments, ovens, etc.) that then transport the signal out through their power feedthroughs. All non-RF feedthroughs into the vacuum system have RF chokes in line to filter out RF signals. Ferrite beads appropriate for 25-32 MHz can also be slipped over non-RF cables and positioned as close to the chamber as possible where the RF signal could leak out. Shielded RF and non-RF cables can also help minimize the leakage problem. Eliminating physical gaps or holes in boxes containing RF signals and providing a separate ground point for all RF electronics from other electronics may help.

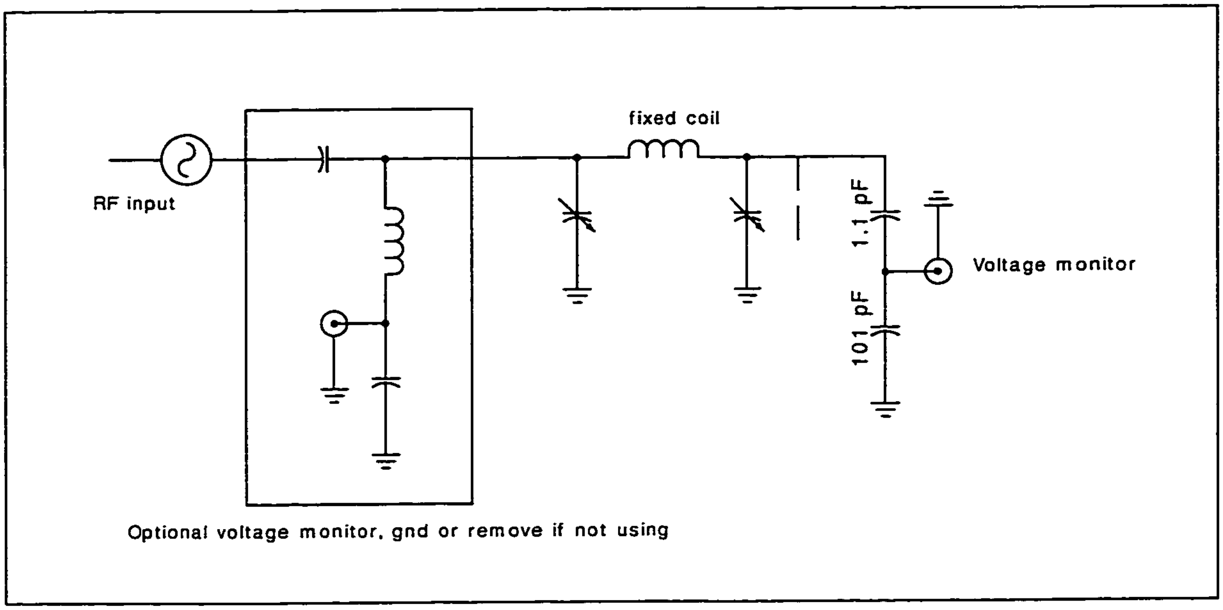

Figure 4.16: [Pi network circuit used to step up the trap voltage to hundreds of volts. The coil is fixed. Impedance matching within the circuit is accomplished with two variable capacitors. An optional voltage monitor usually contained in a separate and removable box is also shown and can be used in either circuit.

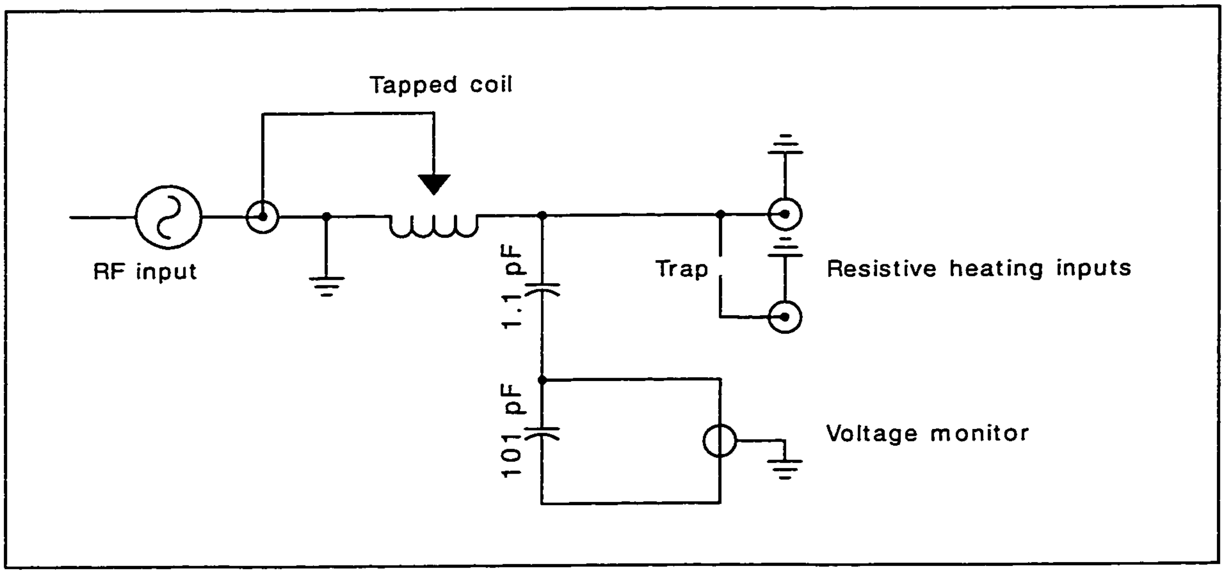

Figure 4.17: Tapped coil step-up trap circuit. This circuit will step up the trap voltage to hundreds of volts. The tapped coil is adjustable for proper impedance matching within the circuit. The monitor output gives the voltage on the trap /100.

The trap voltage can be measured by charging the trap up to the maximum amplitude of the trapping voltage. With the RF power tuned to its operating level in the presence of an active electron source (such as a biased filament), electrons will jump to the trap during the positive half of the RF cycle and continue until the trap is neutral. When no more electrons are attracted to the trap, charging ceases at the maximum voltage amplitude. This voltage can be monitored and measured at various points indicated in the schematics above.

4.5 Trapping elements

The several elements needed to create and trap barium ions are the same for both systems. This section describes how these pieces are constructed and used. All elements are aligned by eye and mounted after the trap is in place. The electron beam and neutral beam of barium should intersect at the trap. They are mounted as close to the trap as possible without blocking the incoming or outgoing light paths. Elements in the Classic chamber tend to be mounted using crimp-type or in-line barrel connectors. Elements mounted in System 97 tend to be spot welded directly to the pins.

4.5.1 Ovens

The barium ovens are constructed from 0.001-inch thick stainless-steel shim stock. A tube about 1.5-cm long and 2-mm in diameter is made by wrapping the rectangle around a copper wire form and spot welding the sides. (It is important not to punch holes into the metal when spot welding.) One end is flattened, wrapped around, and welded to a tantalum lead. After filling the oven to the half-way point, a second lead is folded over to pinch the oven closed like a paper clip and attached by spot welding at the fill point. This leaves a cold muzzle or baffle on the front of the hot oven to control the angular dispersion of the spray of barium. The oven front should be mostly but obviously not completely closed. Two ovens are usually constructed with one lead in common to both.

Pure barium is not stable at room temperature and atmospheric pressure and for this reason is not used as oven material. Barium getter material used in vacuum pumps is a pressed powder of a barium-aluminum alloy[11] and is used instead to fill the oven tubes. When activated, barium will spray radially outward from the front of the tube (mostly). The barium is disassociated from the alloy either during baking, outgassing, or first use. A flash of light may be seen at this point. When trapping, a current of 4-8 Amps is necessary to make the oven barely glow orange. This is sufficient current to create a beam of pure, neutral barium.

---

[11] SAES Getters/USA, Inc.

4.5.2 Filaments

A filament in conjunction with an anode is used as a possible electron beam for ionizing the neutral barium. One or more filaments are constructed from 12 mil (sometimes acid-etched to be thinner) thoriated-tungsten wire about 1 cm long and spot welded to tantalum leads or directly to the Alumel pins. A small (couple cm), squarish anode made of thin but rigid Advance or 0.005-inch-thick stainless-steel metal with a small hole drilled in it. The anode can be bent to enclose the filament. Alignment of these elements follows placement of the trap. The filament must be able to see the trap center through the hole in the anode. This filament light must also be invisible to the PMT. A voltage of over 10 V between the filament and anode is sufficient to ionize the neutral barium. This filament was rarely used for its intended purpose because the electrons needed for ionizing the barium atoms were produced by the heated oven itself.

A second filament made by wrapping the tungsten wire around a small (same as trap form) wire to form a more substantial source of light is mounted directly beneath the trap hole. This is the curly filament that is used to create a trap shadow on the pinhole of the light-collection system during alignment procedures.

4.5.3 Compensation plates

Compensation plates are used to add a DC electric field to the oscillating trap fields. The plates are 1-cm squares of Advance or stainless-steel metal spot welded to tantalum leads or directly to the pins. We generally install only one pair of compensation plates aligned parallel to the plane of the trap loop and within 1 cm of the trap.

4.6 Magnetic shielding

The goal for magnetic shielding is to reduce ambient field levels inside the chamber to much less than μGauss. The eventual plan for maximum magnetic shielding includes housing the entire chamber in μ-metal magnetic shielding with small holes for laser beam access, light collection, and power feedthroughs. The pump, which has large, permanent magnets, will be outside the shielding. The pump may be moved further away from the trap center, to minimize its effects. As a first step, the pump magnets themselves are housed in the shielding material. The pump has been moved about 6-12 inches from the trap center with additional vacuum tubing.

4.7 The lasers

One challenge to a viable spectroscopy experiment like this one is the availability of light sources. A further challenge for this particular experiment is the stability of all light systems. Precision experiments require months of continuous data taking to accumulate sufficiently high statistics. The lasers must be stable enough to not require any manual handling for at least days at a time and particularly overnight. Most other barium trapping experiments use fussy Ti-sapphire, dye, and color-center laser systems that require constant babysitting. It would not be practical to attempt the PNC light shift measurement using those types of laser systems. All of our lasers are highly stable, solid-state lasers that we further stabilize by locking in various ways, depending on the particular laser. Under normal operating conditions, all lasers run continuously.

4.7.1 Light sources

Red

The red laser, used for clean up in the cooling cycle and various detection and optical pumping schemes, is an external-cavity diode laser. Over 1.5 mW of power is available, although only hundreds of microWatts are necessary to saturate the transition and therefore were used. All of the data and results discussed here were taken using a homemade external-cavity system for a bare diode laser.[12] The diode is antireflection coated and placed inside a Littrow-configuration cavity based on the design by Steve Lamoreaux. The output end of the laser cavity is created by a diffraction grating mounted on a piezo-driven optical mount. The piezo stack is controlled by an external circuit (see the Appendix for schematics). The diode sits in thermal contact with a thermal electric cooler, controlled by a stabilizing feedback circuit. The grating position and temperature control determine the frequency range of the diode. The output beam appears elliptical in shape and is polarized perpendicular to the table.

Blue

The blue laser, used for cooling and in the detection process, is a 25-mW 986-nm external-cavity diode laser,[13] frequency doubled to produce $\sim$ 500 μW of 493-nm laser light; see Figure 4.18 for a sketch of the doubling system designed by Warren Nagourney. The 986-nm light is sent through various beam-manipulating devices that control phase matching into the cavity and prevent disruptive feedback into the diode laser. Frequency doubling is accomplished in a bow-tie cavity that contains a small potassium niobate ($KNbO_3$) crystal. The cavity is resonant with the fundamental to

---

[12] Laser is a Toshiba T0LD9421.

[13] New Focus Model 6200.

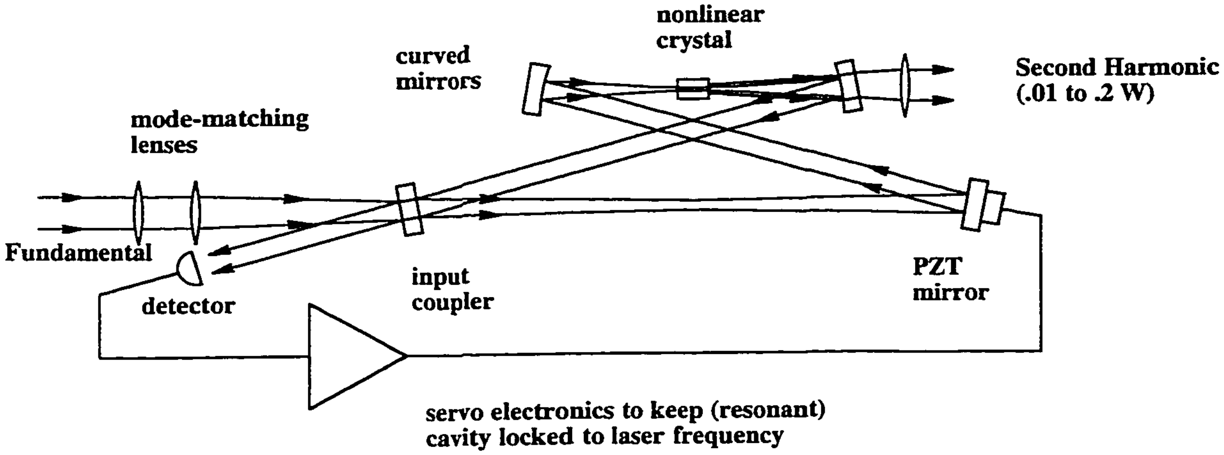

Figure 4.18: Schematic of the frequency-doubling cavity used to produce 493-nm laser light from 986-nm light. Artwork taken from [Nag98].

effectively increase the interaction length of the second harmonic generation (SHG) in the crystal. SHG is a consequence of the nonlinear behavior that occurs in materials at high electric-field intensities, like those created by focused laser beams. Inside the nonlinear crystal, a laser beam of frequency ω is partially converted to a coherent beam at 2ω. The physical origin of SHG is the beating of the fundamental frequency with itself as a result of the nonlinear relationship between the induced dielectric polarization of the medium and the applied electric field [ABD66]. The first observation of SHG was by Franken, Hill, Peters, and Weinreich in 1961 [FHPW61].

When phase-matching conditions are met in the cavity, a growing instead of oscillating generated wave at 2ω is produced. To achieve this, the phase velocity of the polarization (doubled) wave must be the same as that of the generated electromagnetic wave,

$$v_P = \frac{\omega}{k_\omega} = v_E = \frac{2\omega}{k_{2\omega}}. \tag{4.8}$$

A Faraday isolator is positioned after the diode laser and before the bow-tie cavity to extinguish any light that may reflect off the high quality optics in the cavity and interfere with stable diode-laser operation. Even small amounts of light reflecting off mirrors in the bow-tie cavity can affect the diode because its influence is multiplied by the high build-up factor of the cavity. The isolator works by rotating the plane of polarization of the electromagnetic radiation as it passes through the isotropic medium that is exposed to a magnetic field inside the isolator unit. The angle of rotation is proportional to the magnetic-field strength and the isolator length. A linear polarizer precedes and follows the magnetic field region, aligned to allow the forward light to pass maximally through both. Any reflected light traveling back through the isolator is rotated again and therefore not transmitted through the input polarizer.

For cw operation, the bow-tie cavity (once tuned) is locked to the drifting whims of the 986-nm laser using a frequency-stabilization-by-polarization-spectroscopy technique [HC80]. An error signal for a servo loop is generated by analyzing the degree of elliptical polarization of light of the fundamental frequency reflected by the resonant cavity. The parallel and perpendicular light polarization components suffer different frequency-dependent phase shifts upon reflection. Relative phase changes between the two components produces the elliptically polarized light. On resonance, the reflected-wave components remain in phase. Away from resonance, the parallel component is phase shifted relative to the perpendicular component; the handedness of the ellipticity depends on the sign of the detuning from resonance. The ellipticity is detected using a quarter-wave plate and a linear-polarization beam splitter. The light intensity of the split beams are monitored by two photodetectors and a differential amplifier.

One mirror of the bow-tie cavity is mounted on a PZT whose position is controlled by an electronic servo system that monitors the output of the 986-nm laser, as just described. The infrared laser drifts $\sim$ 5 MHz/min. The blue laser may wander out of range of its locking system once every few days. Mechanical jarring of the system can also disrupt the lock. The entire system is bolted on a solid slab of aluminum and is housed in a cardboard box to protect it from disruptive wind currents in the room.

The full schematics with description can be found in [Sch00]. The blue-laser output beam typically carries a couple of transverse modes. It is polarized parallel to the table. The beam is focused via a fiber-coupler into a visible-light fiber. A small loop is made in the fiber to eliminate all but the lowest-order cavity mode.

2 μm

The 2.05-μm infrared laser is a diode-pumped microchip laser.[14] The Tm^{3+},Ho^{3+}-doped $LiYF_4$ (YLF) crystal is 4 mm in diameter and 1-mm thick. The crystal is plano-convex and coated for 98% 2.05-μm reflectivity, creating the mirrors of the laser resonator.

The crystal is pumped at 792 nm by a 0.750-W fiber-coupled diode laser[15] that is collimated and focused to a small spot inside the crystal; see Figure 4.19 for a sketch of the 2-μm laser. The infrared output, with the 792-nm light absorbed by a filter, is collimated by a lens included in the laser assembly. Output beam divergence is ~ 8.6 mRad with an internal mode size of 218 μm [Koc].

Laser operation is on the $^5I_7$ to $^5I_8$ transition in holmium, as shown in Figure 4.20. The diode pump beam is absorbed into the $^3H_4$ level in thulium from its ground state. The excitation decays into the $^3F_4$ level in thulium by radiative and nonradiative (phonon de-excitation) processes. The $^3F_4$ level then transfers excitation to the holmium $^5I_7$ level, which is the upper level of the lasing transition. Above threshold for laser operation, two infrared photons are produced for each absorbed

---

[14] Actual laser courtesy of NASA/Langley and the Lidar-in-Space Technology Experiment (LITE).

[15] Opto Power Corporation part number OPC-A001-792FC.

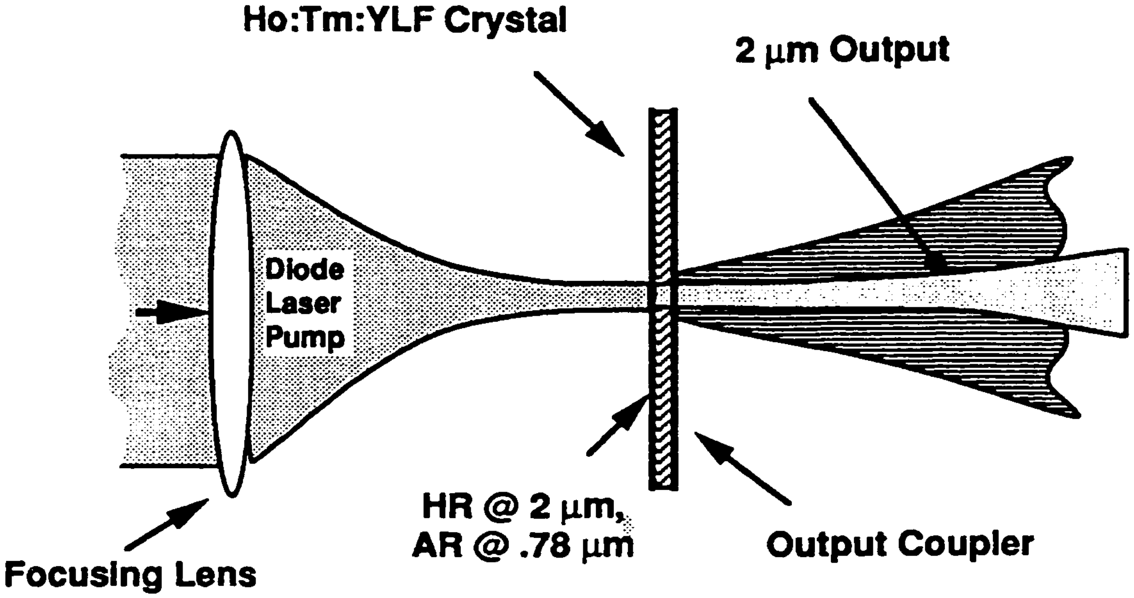

Figure 4.19: Sketch of the 2-μm laser. The diode laser pump light at 792-nm is focused into the crystal where the infrared light is produced and emitted. The intense pump light is filtered from the output. Diagram courtesy of NASA/Langley and the Lidar-in-Space Technology Experiment (LITE).

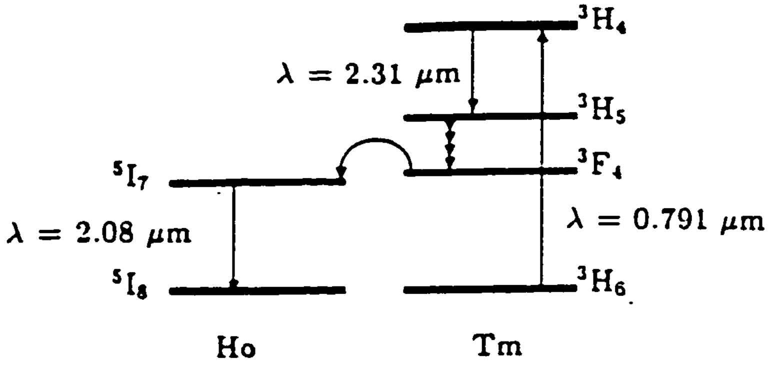

Figure 4.20: Pumping diagram for cascade laser emission, showing energy-transfer processes in the 2-μm laser [Est89].

pump photon due to cross-relaxation processes [Est89]. This is a quasi-four-level laser where the lower level of the lasing transition is in the ground-state manifold but is not the very lowest Zeeman level [BFN+93].

Free running, the laser drifts approximately a MHz/min. Measurements indicate that the linewidth is < 10 MHz and probably $\ll 1$ MHz in a slow scan that includes frequency jitter, as reported by users of similar laser systems [KBZ92, KDS93]. A fast scan would be expected to yield a laser linewidth $\ll 5$ kHz [Sto]. The single-mode power output is ~ 10 mW based on measurements using a pyroelectric radiometer.

In the infrared-laser system, fine tuning of the output frequency is accomplished by adjusting the input current to the diode pump, which changes the output power of the pump, thermally inducing a change in the crystal's cavity length and in the index of refraction of the crystal [ZK92]. This tuning yields MHz/mA changes in the laser output [Sto]. Coarse tuning is achieved by changing directly the temperature of a thermo-electric cooler (TEC) that is in thermal contact with the crystal microchip. The wavelength tunes ~ 2 GHz/°C when directly changing the crystal temperature. Tuning is highly reproducible for given temperature and current settings. Single-mode

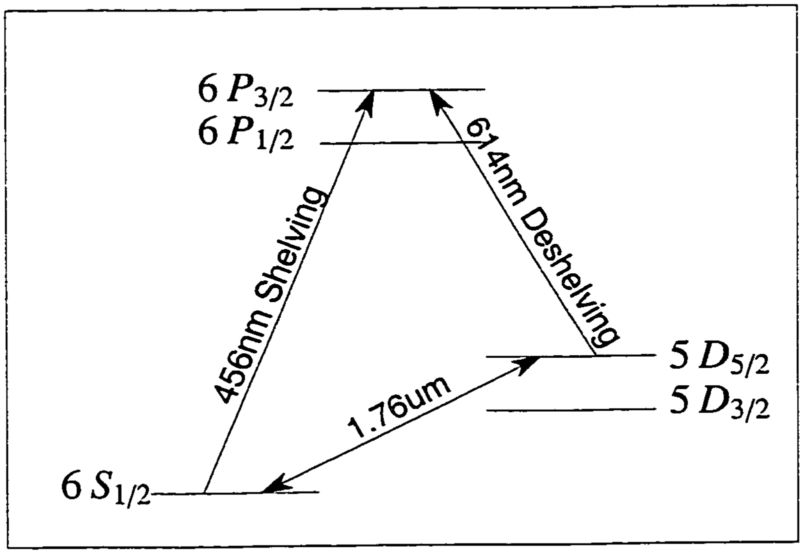

Figure 4.21: Energy-level diagram for Ba^+ showing shelving and deshelving transitions. Direct shelving is accomplished with a 1.76-μm laser from the $6S_{1/2}$ state to the $5D_{5/2}$ shelved state. Indirect shelving pumps from the ground state to the $6P_{3/2}$ state using 456-nm light, from where the electron eventually falls into the $5D_{5/2}$ shelved state. After shelving and to decrease the duty cycle of a measurement, the electron can be optically pumped out of the shelved state directly with 1.76-μm light or indirectly with 614-nm light.

output can be selected by adjusting the pump power and the position and degree of focus of the pump light in the crystal.

Shelving and deshelving

Shelving and deshelving, which is described fully in Chapter 6, directly requires a 1.76-μm laser; see Figure 4.21 for an energy-level diagram of Ba^+. This yields optimal shelving efficiency. For the data and results presented in this thesis, shelving and deshelving are accomplished with sufficient efficiency with a focused and filtered barium hollow-cathode lamp.[16] A wheel holding the two interference filters is mounted on a stepper motor that is controlled remotely by the computer. The shelving (and hence deshelving) light can be polarized using a linear polarizer and a quarter-wave plate fixed in the path of the light beam.

4.7.2 Laser locking

Red

The red laser is locked to the peak of the resonance line produced by the opto-galvanic effect in a dedicated barium hollow-cathode tube. This effect is produced by the interaction of the Ba^+ ions in the barium plasma with the red laser light. The population redistribution of Ba^+ caused by the resonant light alters the current from the cathode to anode in the lamp. As the frequency of the laser is altered away from resonance, the change in the current decreases. Sweeping the laser frequency from below resonance to above, we see that the current follows a Doppler-broadened resonance curve. The cavity of the diode laser is dithered to generate a slope of the resonance line. A servo-feedback electrical system creates an error signal from the slope and feeds that signal back to the red laser as a voltage correction to the piezo behind the grating. The linewidth of the resonance line is $\sim$ 1 GHz, producing a linewidth of $\sim$ 30 MHz for the locked red laser. The schematics and full description of the phase-sensitive lock-in circuits used to lock the red laser are found in [Sch00]. Only rare, campus-wide power failures or major environmental changes necessitate hand tuning of this laser.

---

[16] Perkin Elmer part number 0303-6012 or N305-0109.

Blue

The frequency-doubling cavity of the blue laser follows the 986-nm (infrared) laser as it drifts, necessary to maintain constant lasing of the blue light (as described in Section 4.7.1). The frequency of the blue laser then wanders around as the frequency of the infrared laser drifts. This situation is undesirable for long-term trapping and during experiments. A separate locking system indirectly monitors the blue-laser frequency, keeping it within operational limits by appropriately changing the frequency of the 986-nm laser. The computer monitors the total number of blue photons scattered by the ion each second as it cools and changes the current to the 986-nm laser appropriately if the photon count averages above or below user-defined preset levels. These levels are set below the peak number of photons/second scattered by the ion to allow a range of play before the laser may be mistakenly tuned to the too hot or too cold side. This technique has proven to be extremely effective in practice.

A resonance line due to the opto-galvanic effect in a separate barium hollow-cathode tube, again produced by the interaction of the barium plasma with the laser light, is monitored and displayed in another window by the computer. This resonance line is used to manually tune the blue laser for initial trapping and before beginning experiments.

2 μm

An active frequency-locking scheme for the 2-μm laser is currently under construction. The laser will be locked to the reference signal provided by the spectral resonance of a high-finesse (F=500), external, reference cavity. The nearly confocal cavity is composed primarily of Zerodur, a zero-expansion ceramic glass that does not require strict control of the environmental conditions for high stability. The entire cavity can be further thermally stabilized by wrapping it in heater tape and surrounding that with insulation, if necessary. A PZT is secured with optical epoxy between the Zerodur spacer and one mirror to allow scanning of the cavity length over a range of 3 μm. It is necessary to shape and focus the input beam using lenses and other mode-matching optics to couple properly into the desired lowest-order transverse mode of the cavity. To reduce the coupling from degenerate transverse modes, the cavity length is chosen to be far from the degenerate case. After the laser is roughly tuned with a wave meter, phase-sensitive detection is used to determine the instantaneous frequency difference between the laser and the reference signals as the reference-cavity length is dithered. The phase-sensitive detection and lock-in circuits are identical to those used for locking the red laser except that the feedback signal alters the current of the pump diode in this case.

The precision achieved by locking in this manner depends on the frequency width of the reference line, which translates into the degree of the slope of the frequency discriminant. This cavity is designed to produce a 747 kHz linewidth of the discriminant. Optimally one expects to be able to lock to 1/10 of that width, yielding a locked width of 75 kHz.

4.8 Focusing optics system

The collimated red laser beam is aimed through its polarization box to a 50% beam-splitter. The blue laser beam is emitted from the end of an optical fiber and then collimated by an achromatic lens. The collimated beam passes through its polarization box. The beams are combined by the 50% beam splitter and then pass through a microscope objective. The combined beams pass through two camera lenses: the first is a 105-mm portrait lens that expands the beams and the second is a telephoto lens of focal length 200 mm that focuses the beams to a 50-100-μm diameter at the trap. The distance between the lenses and the trap are variable. Each beam can be focused independently because the position of the blue laser's fiber is variable. The telephoto lens is mounted on an XYZ-translation stage. Three-dimensional motion of this lens is used during trapping to tweak the position of the lasers' spot in the trap.

4.9 Computer control

A modest PC is used to control as many aspects of the experiment as possible, maximizing data taking. Each step in the experiment cycles shown in Chapter 6 is controlled by the computer. With computer-controlled stepper motors holding customized wheels, the laser beams can be turned to on, off, or attenuated settings. The computer also sets and changes the polarization of the red and blue lasers with voltage-controlled variable retarders in conjunction with linear polarizers or quarter-wave plates.[17] Another stepper motor holding a filter wheel switches the shelving lamp to shelving, deshelving, both, or off. The applied magnetic fields are also controlled by the computer through a custom-built, regulated, high-current controller.[18]

The same computer is used to lock the blue laser to the ion count level. It also accepts the opto-galvanic signal from the blue laser's hollow-cathode tube, generating a display that is used to manually tune the blue laser. In a separate window, the computer displays the current red-laser locking signal.

Raw data from the ion are in the form of photons of blue light scattered by the ion. These data are interpreted according to the particular experiment and usually are used to determine which atomic state the ion was in. The computer collects these count measurements, waits for predetermined clues, and proceeds through a dictated measurement cycle. Preliminary data based on the data collected by a particular

---

[17] Thorlabs CR-100 is a continuously variable wave plate, whose retardance is controlled manually with a knob or remotely with a 0-5 V input signal. An input linear polarizer is mounted 45° to the crystal optical axis.

[18] See the Appendix for a schematic of this circuit.

experiment are generated as the experiment runs and are displayed in a separate window on the same monitor to indicate the success of the current experiment.

These windows occasionally can be viewed remotely at http://ionpnc.phys.washington.edu/IonSPY.

Chapter 5

SYSTEMATICS

In precision measurements like the PNC light shift, an important consideration is the statistical limit on the optimal precision that is obtainable in a perfect experiment. This limit was discussed in Chapters 1 and 2 and was found to be satisfactory for this experiment. Systematic effects can limit the achievable experimental precision and perhaps overwhelm and mask the small PNC effect that one is trying to measure. In this chapter I discuss the anticipated systematic effects and strategies for minimizing or eliminating them.

Possible systematic effects arise from a myriad of sources. I group them into three general categories called fake PNC effects, decoherence effects, and magnetic field problems.

5.1 Fake PNC effects

One set of ideal 2-μm laser fields that would create a nonzero PNC light shift in the ground state was presented in Section 3.5.3. A second ideal set of fields that satisfies the same criteria is described as follows:

$$\mathbf{E}' = \hat{\mathrm{x}} E_0' \cos kz, \tag{5.1}$$

$$\mathbf{E}'' = i\hat{\mathrm{x}} E_0'' \sin kz. \tag{5.2}$$

The applied magnetic field in both cases is aligned along z.

With either set of fields, there can be no spurious splittings in the ground state in addition to that due to the PNC light shift. Systematic problems arise when the actual fields deviate from the ideal, as they undoubtably will at some level. We explore the various types of shifts that arise from specific deviations and determine if the spurious shifts can be distinguished from the real PNC light shift [For99].

5.1.1 Dipole field effects

The electric field $\mathbf{E}'$ is tuned to drive the dipole coupling between the ground and $5D_{3/2}$ states. This field amplitude is high to maximize the PNC light shift $\Delta\omega_L^{\text{PNC}}$ that scales linearly with the field amplitude. This intense field nonresonantly couples to higher states and shifts the $5D_{3/2}$ and $6S_{1/2}$ states. If $\mathbf{E}'$ is perfectly linearly polarized as required in the two field cases, then the ground-state shifts are m independent. Any circular polarization of $\mathbf{E}'$ couples to the spin states differentially and will split the ground-state magnetic sublevels by an amount that scales as

$$\Delta\omega^{\text{dipole}} \propto (E')^2 \langle D\rangle^2 \delta'_{\text{circ}}, \tag{5.3}$$

where $\langle D\rangle$ represents a sum over the intermediary states in the nonresonant electric dipole matrix elements and δ'_{circ} represents the small fraction of circular polarization in $\mathbf{E}'$. This shift can be quite large.

This splitting depends only on $\mathbf{E}'$ and not on the quadrupole field $\mathbf{E}''$ directly or through any of the relative phase relationships between $\mathbf{E}'$ and $\mathbf{E}''$. This means that it can be distinguished from the real PNC light shift. The spurious shift can be measured independently by letting $\mathbf{E}''$ go to zero. This also allows us to minimize the offending circular polarization in $\mathbf{E}'$ by tweaking its polarization optics until this spurious shift is minimized.

5.1.2 Quadrupole field effects

The electric field $\mathbf{E}''$ is tuned to drive the quadrupole coupling and ideally is linearly polarized. The amplitude of this field is made to be much smaller than $\mathbf{E}'$ to maximize the PNC light shift relative to the pure quadrupole shift and to minimize generally spurious effects that scale with $\mathbf{E}''$. If $\mathbf{E}''$ has some circular polarization, there will be a splitting between the ground-state magnetic sublevels. This splitting scales as

$$\Delta\omega^{\text{quad}} \propto E''\langle Q\rangle^2\delta''_{\text{circ}}, \tag{5.4}$$

where $\langle Q\rangle$ is the appropriate electric quadrupole matrix element and δ''_{circ} represents the fraction of circular polarization in $\mathbf{E}''$.

Similar to the dipole field effect in the previous section, this splitting depends only on $\mathbf{E}''$ and in no way on $\mathbf{E}'$. The splitting can be determined by letting $\mathbf{E}'$ go to zero. Since the existence of this splitting depends on the degree of polluting circular polarization in $\mathbf{E}''$, the circular polarization of this field can be minimized to reduce this shift.

5.1.3 Quadrupole-quadrupole field effects

If $\mathbf{E}'$ is spatially misaligned, for example, if its standing-wave antinode is not located precisely, it contributes a quadrupole field at the ion. Additionally, if either field has some circular polarization or the angle between the two linear polarizations is not perfect, then a splitting will be created between the ground-state magnetic sublevels. This splitting scales as

$$\Delta\omega^{\text{quad/quad}} \propto E'E''\langle Q\rangle^2\delta_{\text{pol}}, \tag{5.5}$$

where δ_{pol} represents the fraction of the polarization error. This splitting would be quite large, but we are rescued by the nonresonant dipole coupling of $\mathbf{E}'$ mentioned in Section 5.1.1.

The intense $\mathbf{E}'$ dipole field induces an electric dipole moment in the ion. This moment interacts with the applied electric field and causes energy shifts in the participating atomic states. For $\mathbf{E}'$ aligned in the z direction, the energy of this shift is given by

$$\Delta W_\gamma = e^2(E')^2 \sum_{\gamma'} \left[\frac{|\langle \gamma J M_J | z | \gamma' J' M_{J'} \rangle|^2}{W_{\gamma J} - W_{\gamma' J'} - \hbar\omega} + \frac{|\langle \gamma J M_J | z | \gamma' J' M_{J'} \rangle|^2}{W_{\gamma J} - W_{\gamma' J'} + \hbar\omega} \right], \tag{5.6}$$

where the unprimed states are the ones being shifted, the primed states are the intermediate levels, W is the energy of the state, and $\hbar\omega$ is the energy in a 2-μm photon. If we include all the higher levels of Ba^+ up to and including the $10S$ state as possible intermediate states, we find that the ground states and $5D_{3/2}$ states are shifted by the following amounts, assuming an electric field amplitude of 2×10^4 V/cm:

$$6S_{1/2,\pm 1/2} \rightarrow -3.2 \text{ MHz}, \tag{5.7}$$

$$5D_{3/2,\pm 1/2} \rightarrow -1.3 \text{ MHz}, \tag{5.8}$$

$$5D_{3/2,\pm 3/2} \rightarrow -0.6 \text{ MHz}. \tag{5.9}$$

These shifts are shown in Figure 5.1. The $5D_{3/2,\pm 3/2}$ states are shifted 0.7 MHz away from the $5D_{3/2,\pm 1/2}$ states. This substantial difference allows us to tune the 2-μm laser to only the $\pm 1/2$ states of the upper level, removing the possibility of the electric field coupling to the $\pm 3/2$ states and therefore removing the spurious quadrupole-quadrupole splitting.

Another splitting arises if $\mathbf{E}'$ again is spatially misaligned to add a quadrupole field at the ion and if the propagation direction of either field is not quite right. This spurious splitting between the ground-state magnetic sublevels is created perpendicular to the properly aligned $\mathbf{k}$ that is parallel to the applied magnetic field aligned along z and creates a shift that adds to the real PNC shift that occurs and is measured along the direction of the applied magnetic field. This contribution is second order

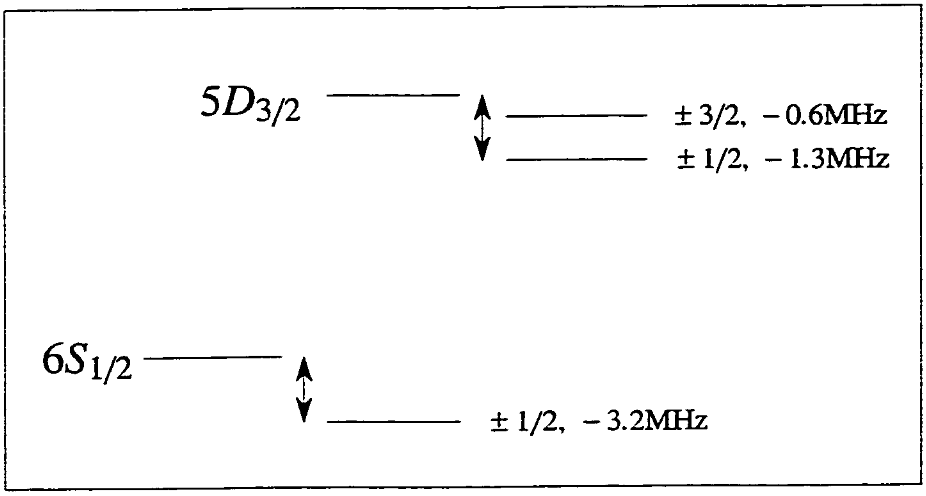

Figure 5.1: Energy-level diagram of Ba^+ showing the energy shifts of the $6S_{1/2}$ and $5D_{3/2}$ levels due to nonresonant dipole effects caused by the PNC electric field.

in the relative size of the shift to the applied magnetic field. If the applied magnetic field is also misaligned, then the net effect of this spurious splitting is amplified to first order.

The field misalignments required to create this spurious splitting can be characterized by three angles. The angle ϕ' is the spatial phase shift of $\mathbf{E}'$ away from ideal, θ'' is the angle that characterizes the misalignment of the propagation directions, and θ_B is the angle of misalignment of the magnetic field. The splitting can be estimated by

$$\Delta\omega_L^{\mathrm{spur}} \approx 10^{-4} \sin\phi' \sin\theta'' \sin\theta_B e a_0 \frac{E_0'}{\hbar}, \tag{5.10}$$

where the factor of 10^{-4} is the ratio of the electric-quadrupole to electric-dipole matrix elements.

There is no way to discriminate this spurious effect from the real PNC light shift. Instead we reduce the phase shifts and misalignment angles to reduce the size of the spurious effect. Our goal is to reduce each of these angles individually to 10^{-4} rad using transitions that only depend on the particular misalignment and tweaking the optics until that transition is minimized. This reduces the spurious shift to

$$\begin{aligned} \Delta\omega_L^{\mathrm{spur}} &\approx 10^{-4}(10^{-4})(10^{-4})(10^{-4})ea_0\frac{E_0'}{\hbar}, && (5.11) \\ &\approx 10^{-5}\times\Delta\omega_L^{\mathrm{PNC}}. && (5.12) \end{aligned}$$

5.2 *Decoherence effects*

The intense dipole field $\mathbf{E}'$ shortens the coherence time available for a single measurement. The nonresonant coupling of this field to higher levels by dipole transitions described in Equation 5.6 increases the decay rate out of the $5D_{3/2}$ metastable state, as illustrated in Figure 5.2. The signal-to-noise ratio for the PNC light shift can be written as

$$\frac{S}{N}\propto E_0'\sqrt{\tau}, \tag{5.13}$$

where τ is the coherence time. This ratio was introduced as an equation in Equation 2.3. The coherence time decreases from its maximum value τ_0 corresponding to the natural lifetime of the $5D_{3/2}$ state as E_0' increases, so that Equation 5.13 can be written as

$$\frac{S}{N}\propto\frac{E_0'}{\sqrt{\tau_0^{-1}+c(E_0')^2}}, \tag{5.14}$$

where c is a constant. When $E_0'\approx 10^4$ V/cm, then $c(E_0')^2\approx\tau_0^{-1}\approx 1/50\ \mathrm{s}^{-1}$. For small values of E_0' up to about 10^4 V/cm, τ_0^{-1} dominates in the denominator and the signal-to-noise ratio increases linearly with E_0'. For larger values of E_0', the signal-to-noise ratio reaches a constant value independent of E_0'.

Spin lifetime shortening can be caused by any process that couples nearby spin states. Time-varying fields like the applied trapping fields, any fluctuating contact potentials on the trap electrodes, room temperature thermal radiation, or other noise

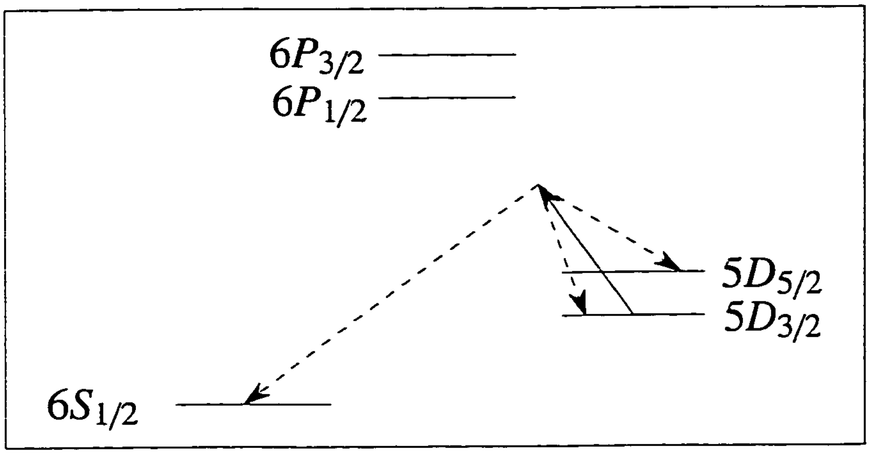

Figure 5.2: Decrease of the lifetime of the $5D_{3/2}$ due to nonresonant dipole coupling. The coherence time available for the PNC light shift measurement is limited by this lifetime.

sources are all possible culprits. The fact that the ion sees a time-averaged zero field in the trap effectively filters out low frequency fluctuations.

Collisions between Ba^+ in the metastable $5D$ states and neutral background atoms can mix those states, called fine-structure mixing. The fine-structure mixing cross section depends strongly on the interatomic velocity and on the energy gap between the fine-structure states. Substantial fine-structure mixing would mean that the lifetime in the $5D_{3/2}$ state would be limited by the shorter lifetime in the $5D_{5/2}$ state [KBKVW92]. Collisions with background gases are also capable of altering the ion's spin state. These collisions occur at time scales on the order of minutes and will not be a major problem.

Experimental measurements of the spin lifetimes at magnetic fields on the order of Gauss with Larmor frequencies of order MHz indicate that the spin lifetimes are very long and not severely limited by any source of spin coupling that fluctuates at MHz frequencies. Measurements at lower magnetic fields on the order of mGauss are planned to continue the search for these problems.

The 2-μm laser is another source of possible decoherence. When the laser deviates from a perfect monochromatic source, it can perturb the atomic states and limit their coherence lifetime, reducing the overall PNC sensitivity. The laser output spectrum must be sharp enough to put negligible power at the Rabi flopping frequency or the dipole splittings of Equations 5.7 - 5.9. This implies that the laser linewidth should be one or two orders of magnitude below 1 MHz for $E_0' \approx 10^4$ V/cm.

5.3 Magnetic field problems

The PNC light shift is created and measured along the direction of the applied magnetic field, which then must be well known to make an accurate measurement. Shielding with μ-metal will substantially reduce the effects of magnetic fields outside the chamber. Constant magnetic fields inside the shielding can be measured and nulled out. Ferromagnetic materials located inside the shielding can make contributions to the total magnetic field that vary in time and depend on the applied magnetic field. Fluctuations in the total magnetic field increase the width of the measured RF resonance between the magnetic sublevels and decrease the signal-to-noise ratio. Their existence can be measured independently before attempting the PNC light shift measurement.

5.4 Concluding remarks

The anticipated systematic effects present a challenge to completing successfully a measurement of atomic PNC in Ba^+. Other unanticipated problems may also arise. We have determined strategies for identifying, measuring, and minimizing the anticipated effects.

Chapter 6

EXPERIMENTS AND TECHNIQUES

Shelving is a technique unique to single trapped ion experiments that allows macroscopic detection of an ion's quantum state. Shelving or quantum jumps in a single ion can be observed when the ion has three effective energy levels: a ground state, a short-lived level strongly coupled to the ground state, and a long-lived metastable level weakly coupled to the ground state. While the ion is in the ground state, a strong fluorescence signal is observed when resonant light is tuned properly. If the ion is excited to the metastable state, then the ion cannot absorb the applied light, which is nonresonant with this transition, and the strong fluorescence abruptly terminates. The fluorescence signal returns when the ion decays or otherwise is forced to the ground state [TDHP$^+$97]. The ion signal in Figure 4.6 shows a single ion undergoing this process.

While shelving is a powerful technique, it is also the only practical technique available for making our measurements on a single ion. The challenge is to devise a way to use the shelving technique to answer each new question.

In the following section, the shelving technique is described in more detail. Each completed experiment is discussed including a summary of the relevant theory behind the measurement, an explanation of how the shelving technique was employed to make the measurement, and a presentation of the data with analysis. The chapter concludes with a summary list of experiments yet to be completed that lead to the PNC light-shift measurement in Ba$^+$.

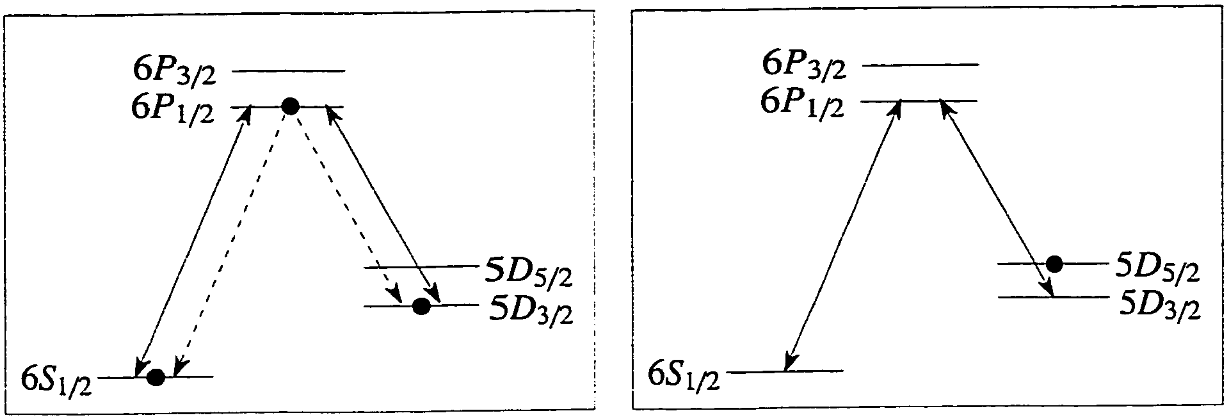

Figure 6.1: Ba$^+$ energy-level diagrams indicating the difference in scattered blue light when the ion is shelved. The solid dots indicate the possible locations of the ion. In both cases, the red and blue lasers are applied to the ion. On the left, if the ion is in the levels indicated, then scattered blue light is visible. On the right where the ion is shelved, no scattered blue light is visible even though the cooling lasers are applied. The difference in blue photons counted per second in the two cases is obvious to the experimenter and to the computer.

6.1 Shelving

Energy-level diagrams for Ba$^+$ are shown in Figure 6.1. The $5D_{5/2}$ and $5D_{3/2}$ states are metastable with lifetimes of about 30 s and 50 s, respectively. Recall that the blue cooling laser connects the $6S_{1/2}$ ground state to the $6P_{1/2}$ excited state and that the red clean-up laser connects the $6P_{1/2}$ and $5D_{3/2}$ excited states, as shown by double-headed arrows in Figure 6.1. When these two lasers are applied to the ion, the $5D_{5/2}$ state is not touched by the resonant light; that is, the $5D_{5/2}$ metastable state is not part of the cooling cycle. A shelved ion (an ion in the $5D_{5/2}$ state) will scatter no blue photons during cooling. An ion in the $6S_{1/2}$, $5D_{3/2}$, or $6P_{1/2}$ state will exhibit strong blue fluorescence. One can know with virtually 100% detection efficiency if the ion is in the shelved state or not. This is the tool that is manipulated to answer any specific question about Ba$^+$.

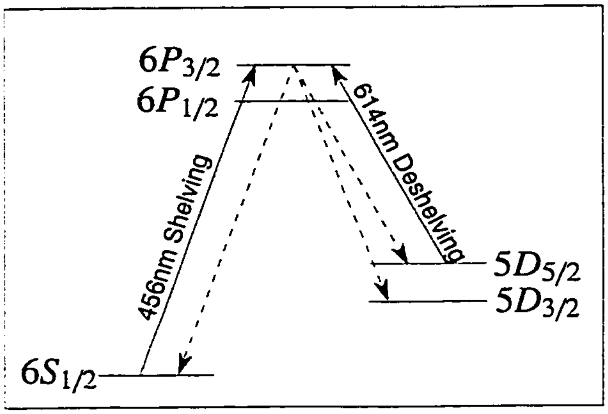

Figure 6.2: Allowed transitions during shelving and deshelving using the indirect method. Filtered and focused lamp light provides light at the two desired wavelengths. Note that from the $6P_{3/2}$ state the ion can decay to the ground state or either $5D$ state.

An ion can be shelved, that is, it can be optically pumped into the $5D_{5/2}$ level from the ground state, directly using a 1.76-μm laser. It can also be shelved indirectly via the $6P_{3/2}$ state using 456-nm light, which is the process used in the experiments presented in this thesis and illustrated in Figure 6.2. Note that indirect shelving has limited efficiency primarily because the ion can decay into either $5D$ state from the $6P_{3/2}$ state. If the ion falls into the $5D_{3/2}$ state, it will not be shelved. This effect is measured in the course of most measurement cycles to determine a maximum shelving probability and is discussed further in the next section. However, one can still know with virtually 100% detection efficiency if the ion is in the shelved state or not, based on whether blue fluorescence is observed or not.

An ion can also be deshelved, that is, it can be optically stimulated out of the shelved state, using 614-nm light that connects the $5D_{5/2}$ state to the $6P_{3/2}$ state, from where it will eventually fall into the ground state as desired.

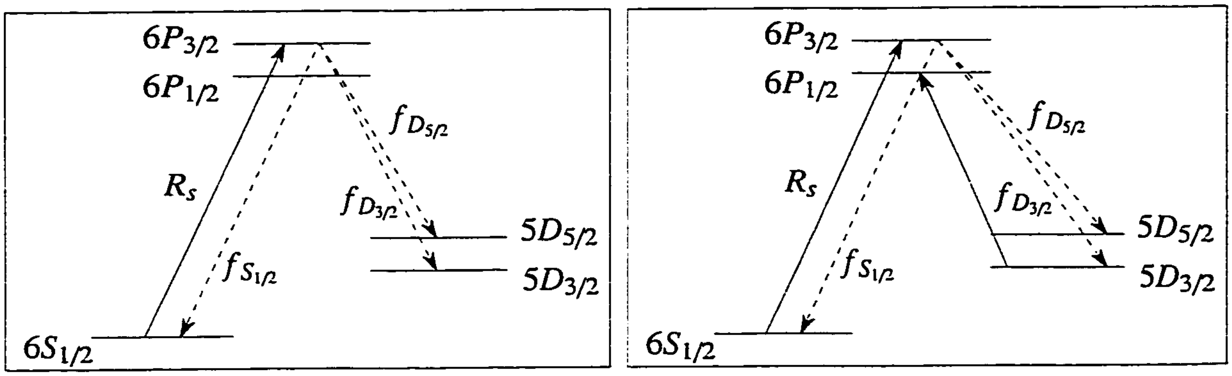

Figure 6.3: Indirect shelving transitions. The right-side figure differs from the left in that resonant laser light is applied to quickly pump the ion out of the $5D_{3/2}$ state. This corresponds to the measurement cycle in Figure 6.4 with red laser light applied during the shelving step.

6.2 Shelving probability and branching fractions

The maximum possible shelving probability using the indirect shelving method is determined by the branching fractions to the $5D$ states from the $6P_{3/2}$ state. Using the measurement cycle in Figure 6.4, we can measure these branching fractions.

The left side of Figure 6.3 indicates and labels the allowed transitions during the indirect shelving process. R_S is the pumping rate from the $6S_{1/2}$ ground state to the $6P_{3/2}$ state. From the $6P_{3/2}$ state, the ion can decay back to the ground state or into the $5D_{5/2}$ or $5D_{3/2}$ excited states. In the following analysis, we neglect decay modes out of the $5D$ states, which is reasonable because these states are metastable. The rate equations for the probability to be in a particular state during the indirect shelving process can be written as follows:

$$\dot{S}_{1/2} = -R_S S_{1/2} + \Gamma_{P_{3/2}} P_{3/2} f_{S_{1/2}}, \tag{6.1}$$

$$\dot{P}_{3/2} = R_S S_{1/2} - \Gamma_{P_{3/2}} P_{3/2}, \tag{6.2}$$

$$\dot{D}_{5/2} = \Gamma_{P_{3/2}} P_{3/2} f_{D_{5/2}}, \tag{6.3}$$

$$\dot{D}_{3/2} = \Gamma_{P_{3/2}} P_{3/2} f_{D_{3/2}}, \tag{6.4}$$

where $S_{1/2}, P_{3/2}, D_{5/2}$, and $D_{3/2}$ are the probabilities to be in that state, $\Gamma_{P_{3/2}}$ is the decay rate out of the $P_{3/2}$ state, and $f_{S_{1/2}}, f_{D_{5/2}}$, and $f_{D_{3/2}}$ are the branching fractions into these states from the $6P_{3/2}$ state. Because the lifetime of the $6P_{3/2}$ state is short compared to all other time scales in the problem, we can assume after a short time that

$$\dot{P}_{3/2} = 0 \rightarrow R_S S_{1/2} = \Gamma_{P_{3/2}} P_{3/2}. \tag{6.5}$$

We also use the normalization condition that

$$f_{S_{1/2}} + f_{D_{3/2}} + f_{D_{5/2}} = 1. \tag{6.6}$$

Substituting Equations 6.5 and 6.6 into the rate equations and using the initial condition that $S_{1/2}(0) = 1$ (recall that the ion was prepared in the ground state), we solve the rate equations and find

$$D_{5/2}(t) = \frac{f_{D_{5/2}}}{f_{D_{3/2}} + f_{D_{5/2}}} \left(1 - e^{-R_S (f_{D_{3/2}} + f_{D_{5/2}}) t}\right). \tag{6.7}$$

The measurement cycle for this experiment is shown in Figure 6.4 and facilitates the introduction of this figure style, which will be used to describe each experiment in this chapter. The top row of boxes uses a schematic of the barium-ion energy-level diagram to pictorially indicate the expected behavior of the ion during each step in the measurement cycle. Dashed arrows indicate the allowed decay channels, and solid arrows indicate the transitions stimulated by the applied light sources. The top line of text states the purpose of each step. The bottom line of text indicates roughly the time required for each step. The first row in the series of narrow boxes shows the expected level of blue photons counted by the light-collection system, corresponding to the sequence of applied light sources (high when participating in the cooling cycle and low when shelved or the cooling beams are blocked). In the remaining rows of

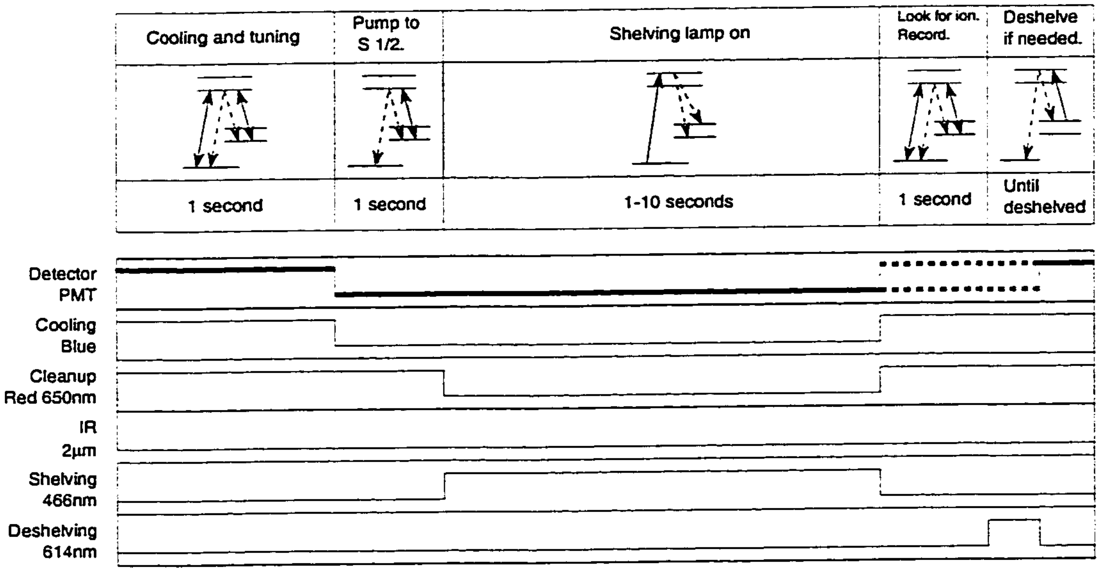

Figure 6.4: Measurement cycle used to determine the branching fractions and hence the shelving efficiency of the indirect shelving method. This experiment was also repeated with red laser light applied with the shelving light, preventing the ion from staying in the $5D_{3/2}$ state. Analysis of the shelving probability in each case yields a determination of the branching ratio from the $6P_{3/2}$ state into the $5D$ states.

narrow boxes, a high grey bar indicates that the light source is unblocked. Each step is controlled by the computer.

To determine the branching ratio, the ion is first laser cooled. At this point in the measurement cycle, the tuning of the 986-nm and therefore the blue laser is checked by the computer and altered if necessary. After cooling and tuning, the blue laser is blocked before the red laser to ensure that the ion is optically pumped into the ground state. This is the usual method to prepare the ion in the ground state. Then the red laser is blocked at the same time that the shelving light is applied for a specified time interval between 1-10 s.

Because the shelving technique is used in the measurement cycles of most experiments, the cycle usually ends with the next and final two steps. The shelving light is blocked while the red and blue lasers are simultaneously unblocked to look for the ion. If the ion was in the $5D_{3/2}$ or $6S_{1/2}$ states, then the PMT will record a strong blue fluorescence. If it had been shelved in the $5D_{5/2}$ state, the PMT will not see the strong fluorescence. The computer knows that the ion was shelved when the average number of photons counted falls below a preset level that is well below the strong fluorescence level of an ion cycling among the cooling transitions. The computer records whether or not (1 or 0) the ion was found to be shelved. Then it deshelves the ion if it had been shelved. And the experiment repeats from the beginning as many times as desired.

A plot of a data set taken according to the measurement cycle in Figure 6.4 is shown in Figure 6.5. The data are plotted as the cumulative shelving probability versus the number of trials. The limit lines plotted on the same figures are determined from

$$\sigma_P = \sqrt{\frac{P(1-P)}{N}}, \tag{6.8}$$

where P is the cumulative probability at a particular trial number N. Clearly after

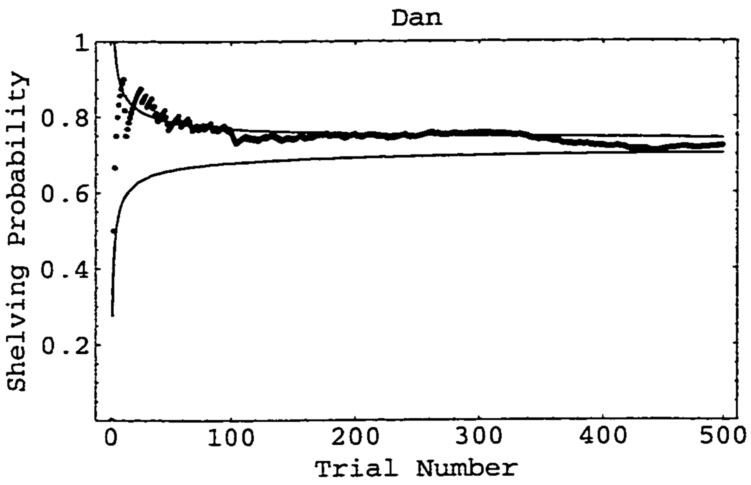

Figure 6.5: Shelving probability data with the red laser blocked during shelving, plotting the cumulative shelving probability P versus trial number N. Limit lines are determined by $\sigma_P = \sqrt{P(1-P)/N}$, assuming binomial statistics.

just a hundred trials, the scatter in the data are merely statistical and fall within the limit lines.

This experiment is repeated with the red laser on during the shelving process to scoop the ion out of the $5D_{3/2}$ state whenever it happens to decay into that state. The measurement cycle is the same as that shown in Figure 6.4 with the addition of the red laser during the shelving step. This process is indicated in the right side of Figure 6.3. The rate equations in Equations 6.1 and 6.4 are altered as follows:

$$\begin{aligned} \dot{S}^{\text{red}}_{1/2} &= -R_S S_{1/2} + \Gamma_{P_{3/2}} P_{3/2} f_{S_{1/2}} + \Gamma_{P_{1/2}} P_{1/2} f' \qquad (6.9) \\ \dot{D}^{\text{red}}_{3/2} &= \Gamma_{P_{3/2}} P_{3/2} f_{D_{3/2}} - R_r D_{3/2}, \qquad (6.10) \end{aligned}$$

where f' is the branching fraction from $6P_{1/2} \to 6S_{1/2}$ and R_r is the pumping rate out of the $P_{3/2}$ state due to the applied red laser light. The pumping rate R_r is sufficiently fast that we can assume within a short time that $\dot{D}_{3/2} = 0$.

Table 6.1: Data used to determine the branching ratio $f_{D_{3/2}}/f_{D_{5/2}}$. Data was taken according to the measurement cycle in Figure 6.4.

Wait time (s)	N	D	D^{red}	D/D^{red}
1	300	0.533±0.03	0.563±0.03	1.056±0.06
2	300	0.727±0.03	0.780±0.02	1.073±0.04
2	300	0.647±0.03	0.740±0.03	1.144±0.05
5	300	0.777±0.02	0.880±0.02	1.133±0.03
10	474	0.696±0.02	0.898±0.01	1.290±0.02

Solving the altered set of rate equations, we find

$$D^{\mathrm{red}}_{5/2}(t) = 1 - e^{-R_S \frac{f_{D_{5/2}}}{1-f_{D_{3/2}}} t} \approx 1 - e^{-R_S f_{D_{5/2}} t}, \tag{6.11}$$

which is the shelving probability with the red laser applied during shelving. The final step is valid because the branching ratio $f_{D_{3/2}} \sim f_{D_{5/2}}/10$. Taking the ratio of the two shelving probabilities in Equations 6.7 and 6.11 in the limit of long times where $R_S t \gg 1$, we find

$$\frac{D^{\mathrm{red}}_{5/2}}{D_{5/2}} = 1 + \frac{f_{D_{3/2}}}{f_{D_{5/2}}}. \tag{6.12}$$

Plots of the data taken with the red laser added are similar to that in Figure 6.5. A table of data taken using both methods for direct comparison is found in Table 6.1. The mean of the ratio of these values is

$$\left\langle \frac{D^{\mathrm{red}}_{5/2}}{D_{5/2}} \right\rangle = 1.10 \pm 0.09, \tag{6.13}$$

where the standard deviation serves as the error estimate. We use these results to determine the branching ratio, as follows:

$$\frac{f_{D_{3/2}}}{f_{D_{5/2}}} = \frac{D^{\mathrm{red}}_{5/2}}{D_{5/2}} - 1. \tag{6.14}$$

Applying this to our numerical result in Equation 6.13, we conclude that

$$\frac{f_{D_{3/2}}}{f_{D_{5/2}}} \approx 0.10 \pm 0.05. \tag{6.15}$$

The overall 5% error is still a rather large fractional uncertainty on such a small branching ratio, but it served our exploratory purposes.

We can compare this measured value to a theoretical estimate. The transition rate between two states is proportional to the square of a Clebsch-Gordan coefficient and to the cube of the energy of the transition;

$$\Gamma_{m_1,m_2} \propto |\langle\frac{3}{2}, m_1; 1, m_1 - m_2|j, m_2\rangle|^2\omega^3, \tag{6.16}$$

where ω is the frequency of the transition and m, j are the angular momentum quantum numbers describing the atomic state. The branching ratio can then be written in terms of the Clebsch-Gordan coefficient and evaluated as follows:

$$\frac{f_{D_{3/2}}}{f_{D_{5/2}}} = \frac{1}{9}\left(\frac{586\text{ nm}}{614\text{ nm}}\right)^3 \approx 0.094, \tag{6.17}$$

which is consistent with our measured results.

The maximum shelving probability cannot be 100% because the ion can decay into either D state and not just into the shelved state. From the branching ratio measured and calculated, we determine that the maximum shelving probability possible using the indirect shelving method is $\sim$ 90%. The maximum shelving probability can be measured during each experiment by shelving the ion and then immediately checking to see if it was shelved. This measurement is generally made during the experiments because the value is also sensitive to other time-dependent factors like the shelving lamp intensity and the laser powers.

6.3 Lifetime experiments

Direct measurements of long lifetimes (> 10 μs) are not generally possible with conventional methods involving collections of atoms and requiring direct observation of decay radiation. However, ions confined in traps for times long compared to the radiative lifetime are unperturbed, allowing measurements of the metastable lifetimes that we present in this section.

Precision measurements of radiative lifetimes provide basic information about atomic wave functions. Energy levels of atoms are known to high precision from observations of the frequency of the emitted radiation. Because of powerful variation methods, energy levels in multi-electron atoms like barium can usually be calculated much more accurately than transition probabilities. But the latter can be more sensitive probes of the details of the wave functions. Measurements thus provide important comparison tests for the Ba^+ atomic wave-function calculations needed to extract the PNC information from the measured quantity.

The lifetime measurements presented in this thesis are not of the highest possible precision and therefore are not appropriate for comparison with atomic-structure calculations. This was not the purpose of making these measurements at this point. At some point, these or other atomic measurements will be completed carefully and precisely using the techniques described in this section for the purpose of comparison to atomic-structure calculations.

The importance of these measurements now is not to make more precise determinations of the lifetimes of these states. Rather, we want to know that the lifetimes are as long as expected and to show that we understand all major systematic effects in our system that could affect the lifetimes and cause other problems, which we have done. We also have verified that we can easily and reliably prepare the ion in these states.

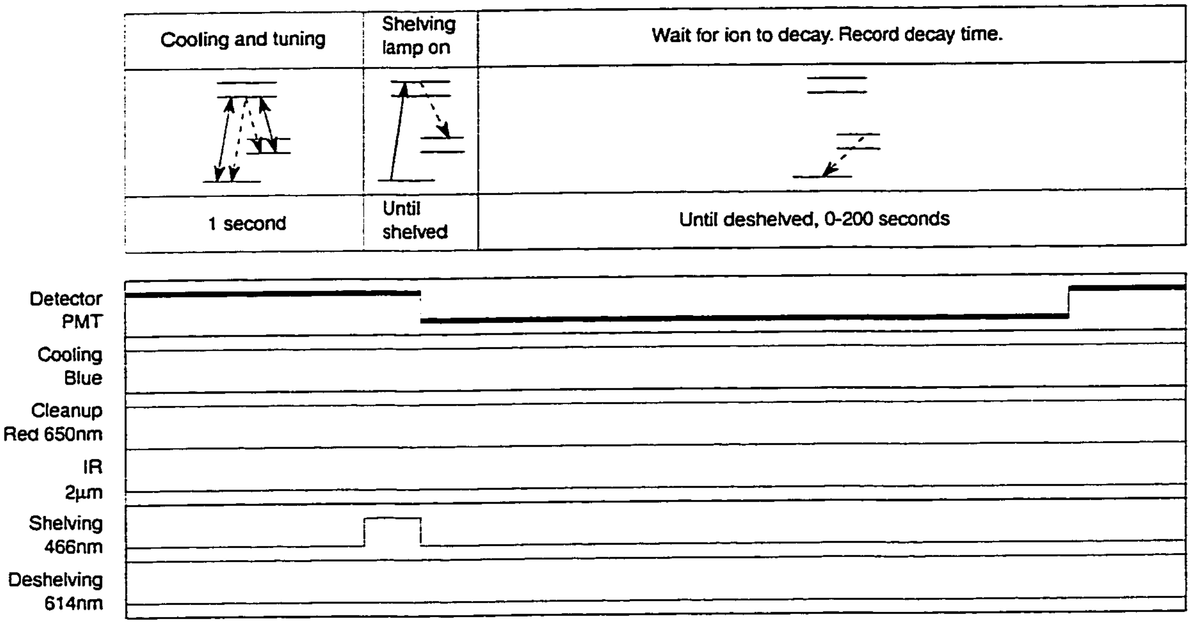

Figure 6.6: Measurement cycle used to determine the lifetime of the $5D_{5/2}$ metastable state.

6.3.1 Lifetime of the $5D_{5/2}$ metastable state

The measurement cycle used to determine the lifetime of the $5D_{5/2}$ metastable excited state is shown in Figure 6.6. Note that both the red and blue lasers remain unblocked during the entire measurement cycle. After cooling and tuning, the ion is optically pumped using the shelving lamp into the $5D_{5/2}$ state, which is the shelved state. The shelving lamp is applied until the computer sees that the ion has been shelved by the abrupt drop in blue fluorescence. Then the shelving light is blocked at the same time that the computer records the start time. Because the red and blue lasers are continually applied to the ion, a sudden increase in blue fluorescence indicates clearly when the ion has decayed out of the $5D_{5/2}$ state. This signal triggers the computer to record the stop time, and the time spent in the $5D_{5/2}$ state before decay is determined. The entire measurement cycle is repeated hundreds of times.

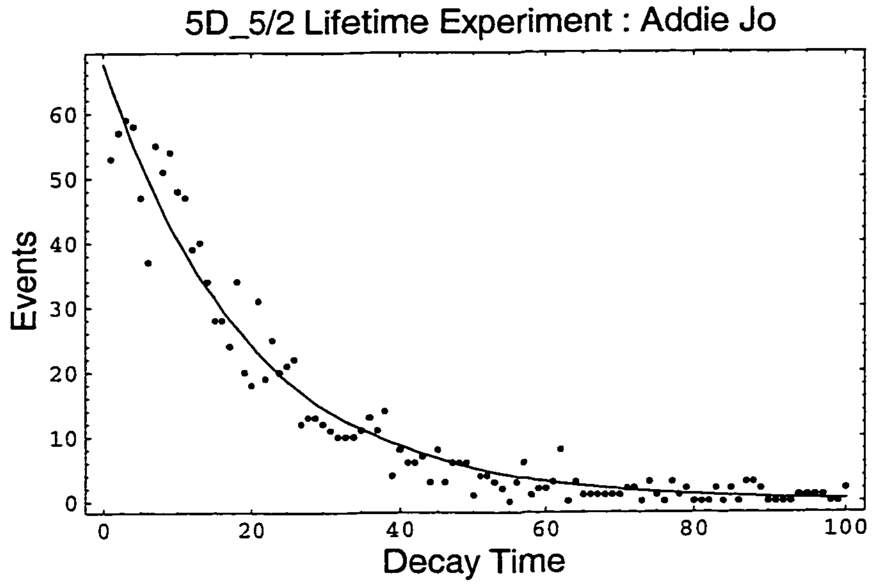

Figure 6.7: Histogram of the data used to determine the lifetime of the $5D_{5/2}$ state. The decay time is in seconds.

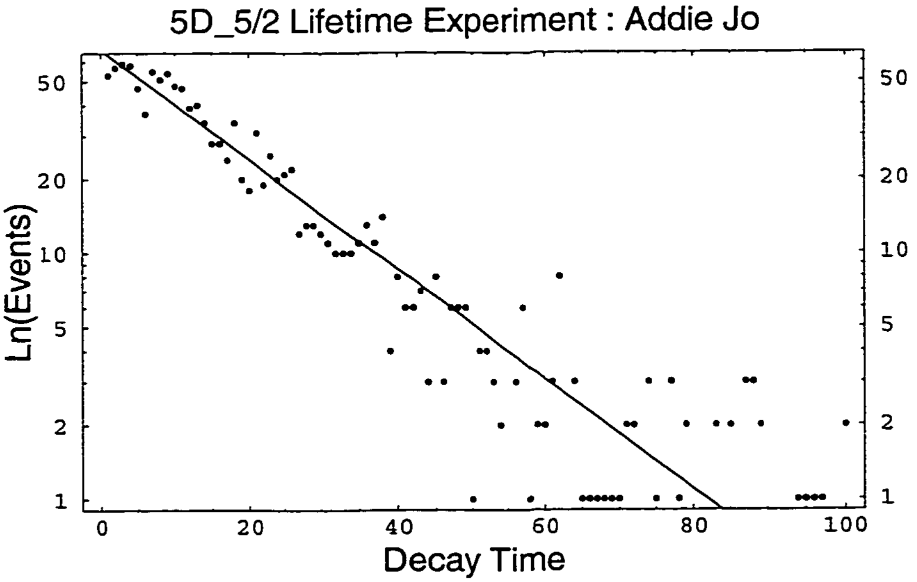

Figure 6.8: Log plot of the data used to determine the lifetime of the $5D_{5/2}$ state. The decay time is in seconds. This plot uses the same data shown in Figure 6.7.

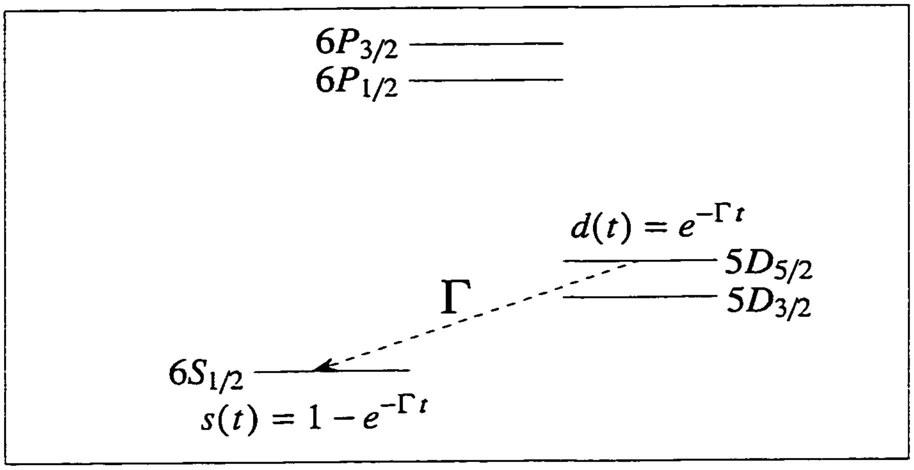

Figure 6.9: Energy-level diagram showing the allowed process in the decay of the $5D_{5/2}$ state.

A histogram of the individual measured lifetimes for one experiment consisting of several hundred trials is plotted in Figure 6.7. Anticipating an exponential relationship, we also plot the data in a logarithmic plot in Figure 6.8.

The probability as a function of time for an ion prepared in the $5D_{5/2}$ state to remain there is given by

$$D_{5/2}(t) = e^{-\Gamma t}, \tag{6.18}$$

where Γ is the decay rate related to the lifetime τ according to $\tau = 1/\Gamma$. This process is illustrated in the energy-level diagram in Figure 6.9. The data in the histogram are fit to an exponential function of the form

$$N(t, t + \Delta t) = \frac{N_0}{\tau} e^{-t/\tau} \Delta t, \tag{6.19}$$

where $N(t, t + \Delta t)$ is the number of shelving events in a time bin of width Δt. From this two-parameter fit, a lifetime of $\tau = 19.4 \pm 0.6$ s is found with $N_0 = 1313$ events. This result compares well to the actual number of observations $N = 1252$ and the mean lifetime $\langle t \rangle = 19.2$ s.

Table 6.2: Table of determinations of the lifetime of the $5D_{5/2}$ state. N is the actual number of observations and τ is the lifetime determined from a fit of the exponential function. The values vary widely and are generally shorter than other published measurements. These results lead to a consideration of possible lifetime shortening effects.

File	Ion	N	$\tau \pm \tau/\sqrt{N}$ (s)
96120503	Addie Jo	1252	19.4±0.6
96121701	Dan	548	6.8 ± 0.3
96121803	Dan	136	10.4± 0.9
96122206	Emma	200	28.8±2.0

A table of $5D_{5/2}$ lifetime results found using the analysis above on independent data sets is shown in Table 6.2. The first row contains the data just discussed. The results range widely from 6.8 s to 28.8 s. Also the lifetimes are generally shorter than expected from other reported lifetime results [Nag]. These inconsistent results suggest that other time-varying environmental conditions are affecting the stability of the state.

Collisional quenching, nonresonant coupling, and resonant 614-nm excitation out of the $5D_{5/2}$ state are other processes that could affect the measurement of this lifetime, as illustrated in Figure 6.10. Collisions are due to residual background gases. The most likely sources of nonresonant and resonant excitation light are the two lasers that are applied to the ion during the entire measurement cycle. We therefore write the total decay rate out of the $5D_{5/2}$ state as

$$\Gamma = \Gamma_0 + AP + BP_{\text{red}} + CP_{\text{blue}}, \tag{6.20}$$

where Γ_0 is the natural decay rate, P is the pressure in the vacuum chamber, and P_{red} and P_{blue} are the respective laser powers. The coefficients A, B, and C are unknown

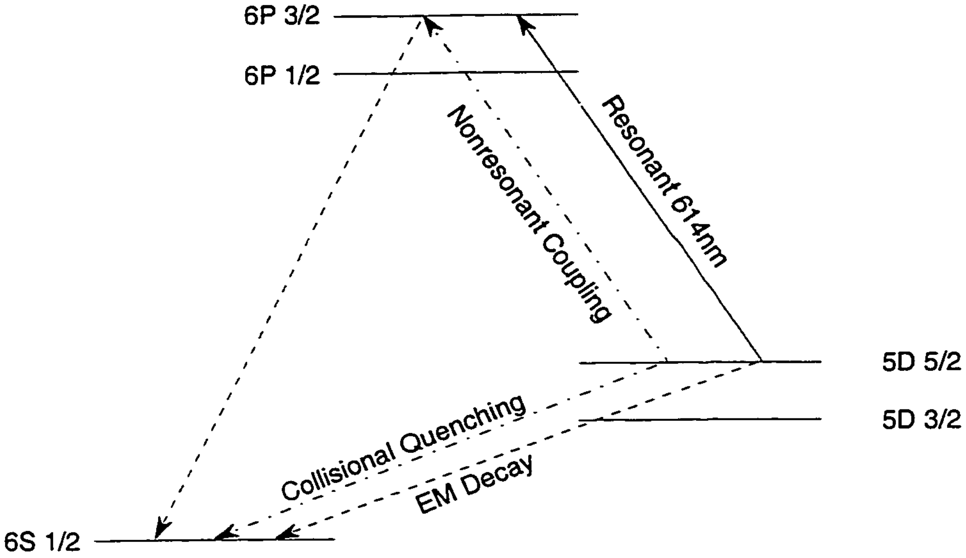

Figure 6.10: Processes possibly involved in shortening the lifetime of the $5D_{5/2}$ state.

factors that carry the necessary units.

We anticipate that we cannot leave the red and blue lasers unblocked continually to watch for the ion to decay from the $5D_{5/2}$ state. Instead, we prepare the ion in the $5D_{5/2}$ state, then block all light sources and wait in the dark for a specified time interval. The lasers are unblocked to learn if the ion had decayed sometime during the wait time interval. This measurement cycle in shown in Figure 6.14.

First, we independently explore the broadening effects of the red laser on the overall linewidth of the $5D_{5/2}$ state by applying only the red laser light during the wait time interval of the measurement cycle, as indicated in Figure 6.11. The power of the red laser is varied with a linear attenuator, since plenty of excess red laser power was available. At each red-laser power level, the $5D_{5/2}$ lifetime and corresponding linewidth are determined. These results are plotted in Figure 6.12. A generally linear relationship between the linewidth and the power is found. A fit of Equation 6.20 to

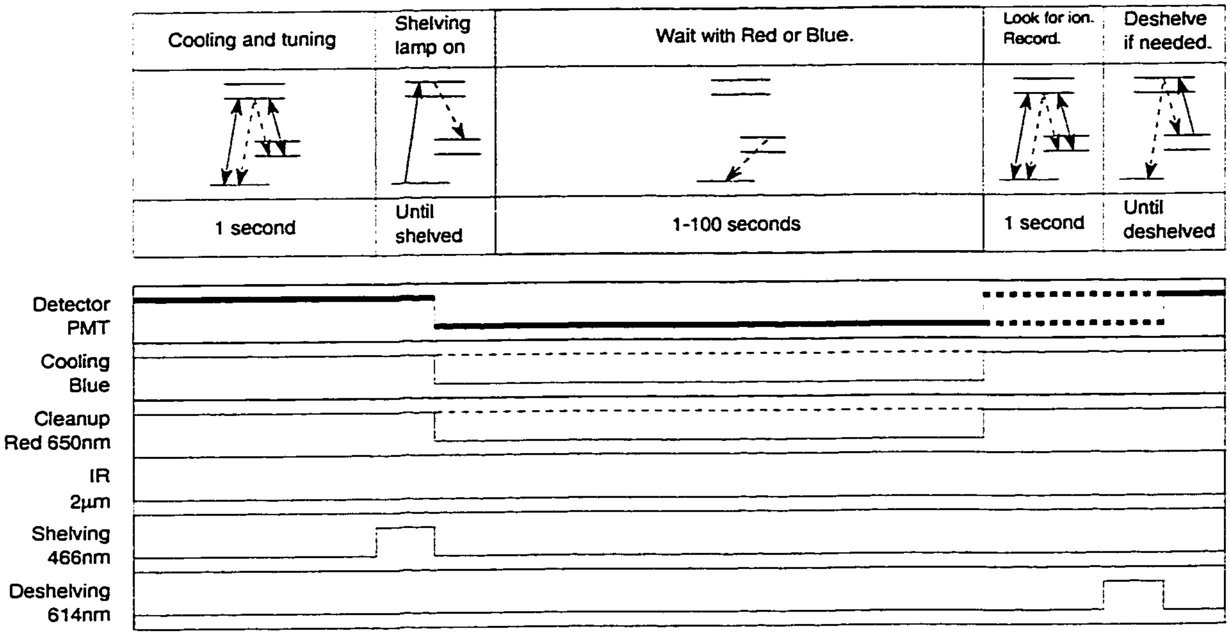

Figure 6.11: Measurement sequence used to explore resonant and nonresonant coupling effects on the lifetime of the $5D_{5/2}$ state.

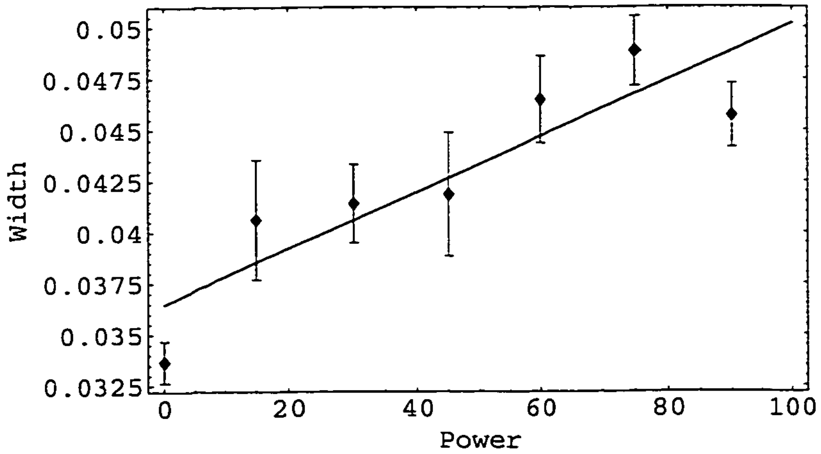

Figure 6.12: Plot of the effects of the red laser that shortens the lifetime of the $5D_{5/2}$ state. The decay width or rate in s^{-1} is plotted versus the power in μW of the red laser light. The power is measured outside the vacuum system and is an overestimate of the red power at the ion. A clear linear relationship fits the data, as expected.

Table 6.3: Table of data used to determine how the lifetime of the $5D_{5/2}$ state is affected by the red and blue laser light. A plot of these data are in Figure 6.13. All P's refer to the measured shelving probability.

Wait time (s)	N	P_{de}	P	P_b	P_r	P_{br}
5	600	0.94	0.76±0.02	0.77±0.02	0.65±0.02	0.84±0.01
10	801	0.88	0.62±0.02	0.62 ±0.02	0.42 ±0.02	0.40±0.02
20	486	0.90	0.47±0.02	0.40±0.02	0.17±0.02	0.16±0.02
40	800	0.94	0.22 ±0.01	0.18 ±0.01	0.04±0.01	0.04±0.01
Lifetime			29.7 ±1.1 s	23.5 ±0.9 s	11.3±0.4 s	11.0±0.4 s

the plot allows us to estimate the coefficient B from the slope of the fit line. The result is $B \approx 0.14$ (s·mW)$^{-1}$. The inverse of the y-intercept gives an estimate of the lifetime contributions due to all other sources; $(\Gamma_0 + AP + CP_{\mathrm{blue}})^{-1}$=27.4 s.

We did not perform a similar experiment with the blue laser because we cannot vary the blue laser power without affecting the ion signal itself.

Subsequent experiments to explore the linewidth broadening effects of the red and blue lasers were made using the same measurement cycle in Figure 6.11, with the red laser only, the blue laser only, the blue and red lasers, or no lasers applied during the wait time interval. These results are plotted in Figure 6.13. The lifetimes corresponding to fits to each curve are

$$\text{No blue/no red} \; : \; \tau = 29.7 \pm \; 1.1\text{s}, \tag{6.21}$$

$$\text{Blue} \; : \; \tau = 23.5 \pm \; 0.9\text{s}, \tag{6.22}$$

$$\text{Red} \; : \; \tau = 11.3 \pm \; 0.4\text{s}, \tag{6.23}$$

$$\text{Blue/red} \; : \; \tau = 11.0 \pm \; 0.4\text{s}. \tag{6.24}$$

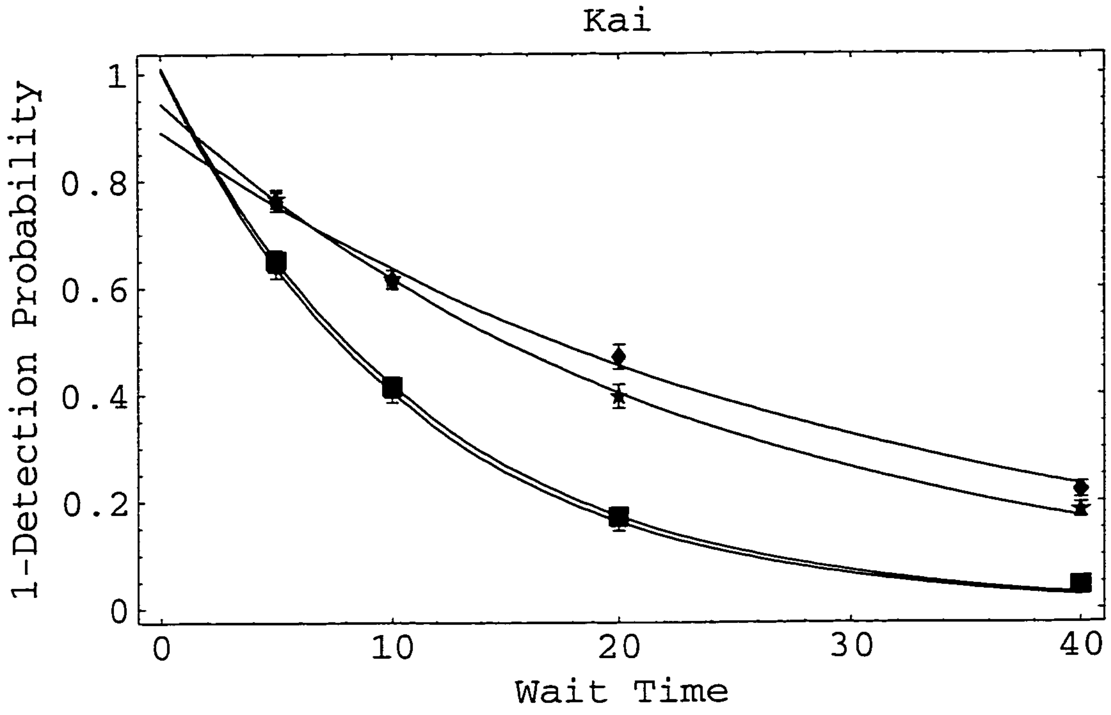

Figure 6.13: Plot of 1 - the detection probability versus the wait time interval in seconds, used to determine the effects of the red and blue lasers on the lifetime of the $5D_{5/2}$ state. Data taken with the red laser only unblocked are plotted with solid squares. Data taken with the blue laser only unblocked are plotted with stars. Data taken with all light sources blocked are plotted with solid diamonds. The data comprising the lowest curve correspond to the situation with both red and blue lasers unblocked. Data used to construct this plot and the resulting lifetimes are found in Table 6.3.

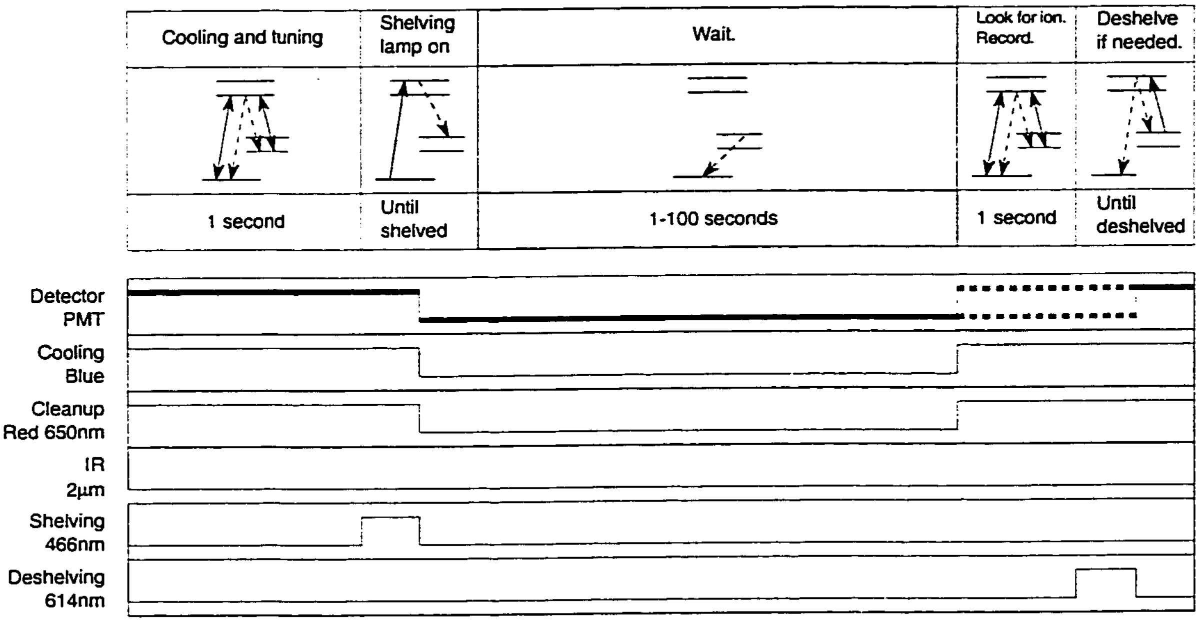

Figure 6.14: Final measurement sequence for the $5D_{5/2}$ lifetime.

We can see that the effect due to the blue laser on the $5D_{5/2}$ lifetime is significantly less. Using the lifetimes obtained from the fits and Equation 6.20, we can estimate $\Gamma = \Gamma_0 + AP$ at our pressure, BP_{red}, and CP_{blue};

$$\frac{1}{\Gamma} = 28.5 \text{ s}, \tag{6.25}$$

$$BP_{\mathrm{red}} = 0.052 \text{ s}^{-1}, \tag{6.26}$$

$$CP_{\mathrm{blue}} = 0.0058 \text{ s}^{-1}. \tag{6.27}$$

Pressure effects were not explored because we had no desire to change an already satisfactory vacuum level.

The ideal measurement cycle to determine the $5D_{5/2}$ lifetime requires the red and blue lasers to be fully blocked during the wait time interval, as shown in Figure 6.14.

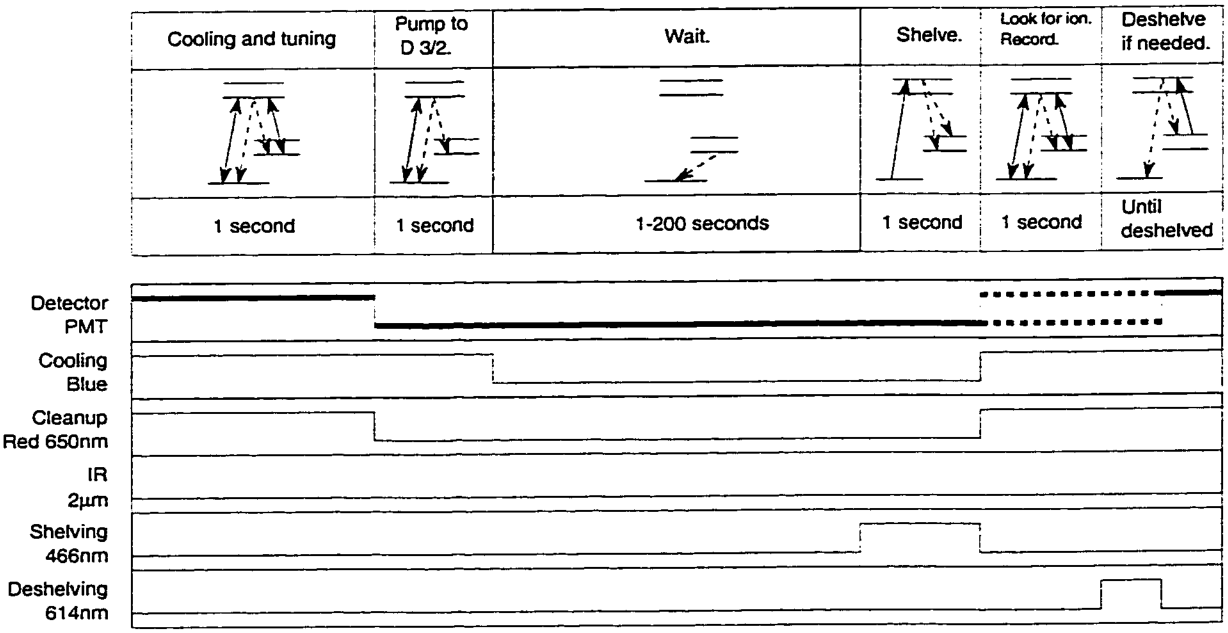

Figure 6.15: Measurement cycle for determining the $5D_{3/2}$ lifetime.

6.3.2 Lifetime of the $5D_{3/2}$ *state*

The measurement cycle for determining the lifetime of the $5D_{3/2}$ metastable excited state is shown in Figure 6.15. The ion is cooled and then prepared in the $5D_{3/2}$ state by blocking the red laser before blocking the blue laser. Then all light sources are blocked for a specified time interval. This interval is stepped for each repetition of the measurement cycle, up to 200 s, and eventually repeated. Next shelving light is applied to shelve the ion if it has already decayed out of the $5D_{3/2}$ state. This step might (1 time out of 10) put the ion back into the $5D_{3/2}$ state, which is taken into account by determining the maximum shelving probability during each experiment. Finally cooling lasers are applied to check if the ion is shelved, recording 1 or 0 for that wait time interval, and deshelving if necessary to prepare for the next measurement cycle.

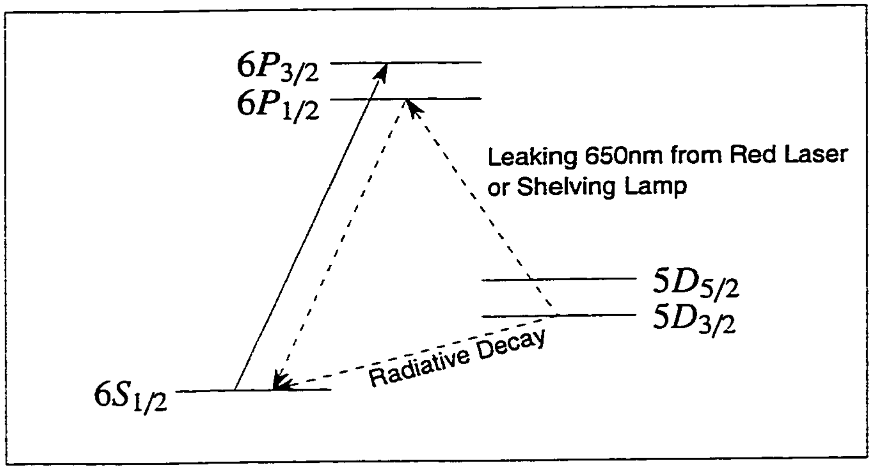

Figure 6.16: $5D_{3/2}$ lifetime-altering effects due to leaking resonant light. Leaking 650-nm light from the red laser would tend to shorten the lifetime.

Leaking red laser light and incompletely filtered and blocked lamp light during the wait time interval was found to alter the measured lifetime of the $5D_{3/2}$ state. These processes are shown in Figure 6.16. To measure and to account for the effect of the red laser, we cool the ion and then prepare it in the $5D_{3/2}$ state. Shelving light is then immediately applied. The ion would only be shelved here if a perturbation prematurely ejected it out of the $5D_{3/2}$ state. The final two steps check for the shelved ion and prepare (deshelve) the ion for the next measurement. Figure 6.17 shows this measurement cycle. An improved interference filter and more complete beam blocking for the shelving lamp and better beam blocking for the red laser significantly reduced these problems.

Having eliminated the leaking light, the ion can leave the $5D_{3/2}$ state only via natural radiative decay or perhaps through collisions with background gases. Collisions are ignored in the following analysis. The data are fit to an exponential function of the form

$$P = P_{\max}(1 - e^{-\frac{t}{\tau}}). \tag{6.28}$$

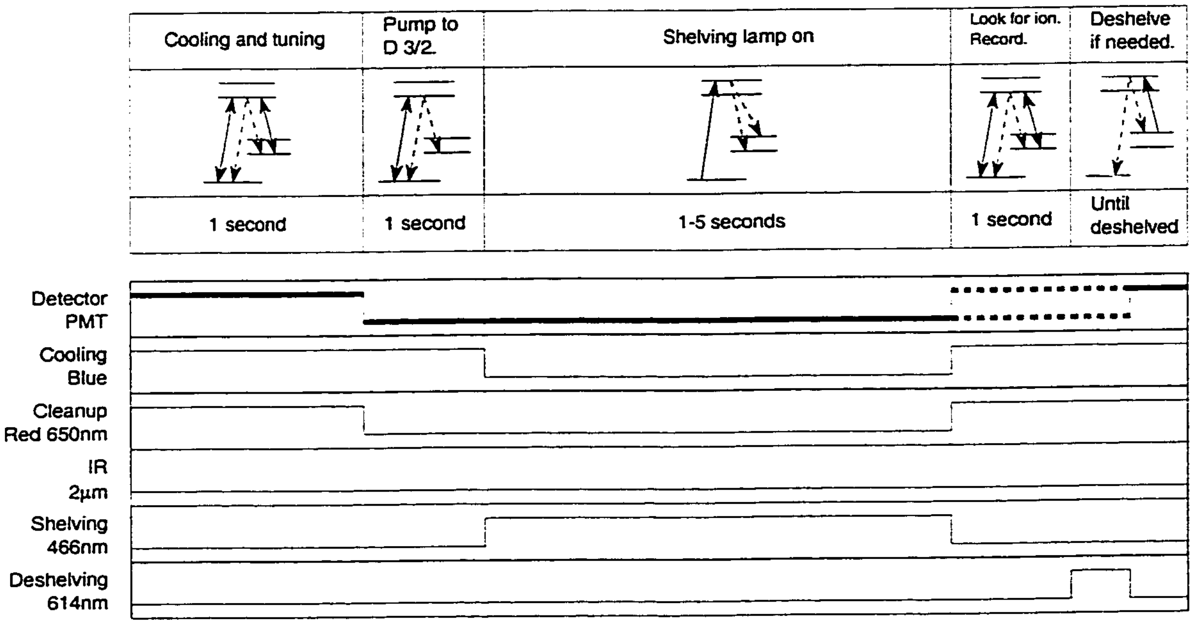

Figure 6.17: Measurement cycle to explore the effect on the $5D_{3/2}$ lifetime due to resonant light leaking into the system.

A best fit to the data yields $P_{\max} = 0.49$ and $\tau = 50.1 \pm 1.4$ s. These results are consistent with published results at similar operating vacuum pressures [YND97, KBKVW92]. A normalized plot of this data is shown in Figure 6.18.

6.3.3 Lifetime of the $6S_{1/2}$ *state*

Measurement of the ground-state lifetime, which should be very long, was an exercise in the search for perturbations in the system and an exploration of state-preparation methods. The measurement cycle is shown in Figure 6.19. After cooling and tuning, the ion is prepared in the ground state. All light sources are blocked for a specified time interval. At the end of this time interval, the ion should still be in the ground state and therefore shelved in the next step. In the final step, the cooling lasers look for the shelved ion, and the result of the search is recorded.

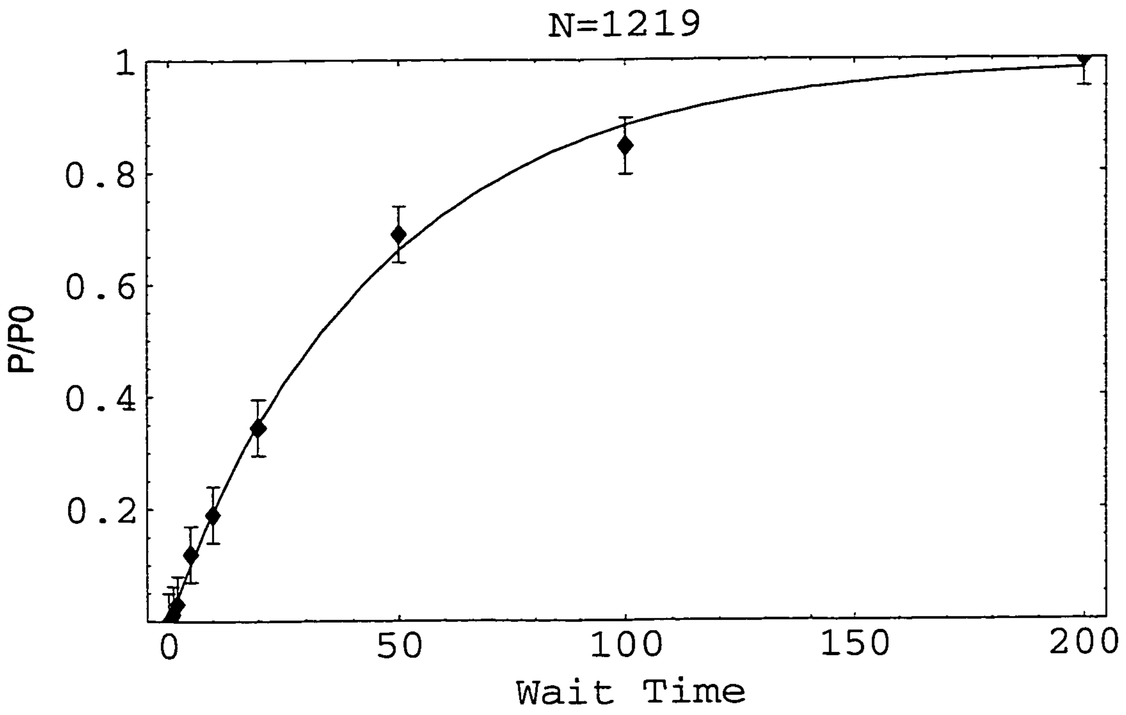

Figure 6.18: Normalized plot of $5D_{3/2}$ lifetime data. Recall that if the ion is shelved, then the ion did decay out of the $5D_{3/2}$ level during the wait time interval. The result of a fit of the function in Equation 6.2 is a lifetime of $\tau = 50.1 \pm 1.4$ s, which is consistent with published results at similar operating vacuum pressures.

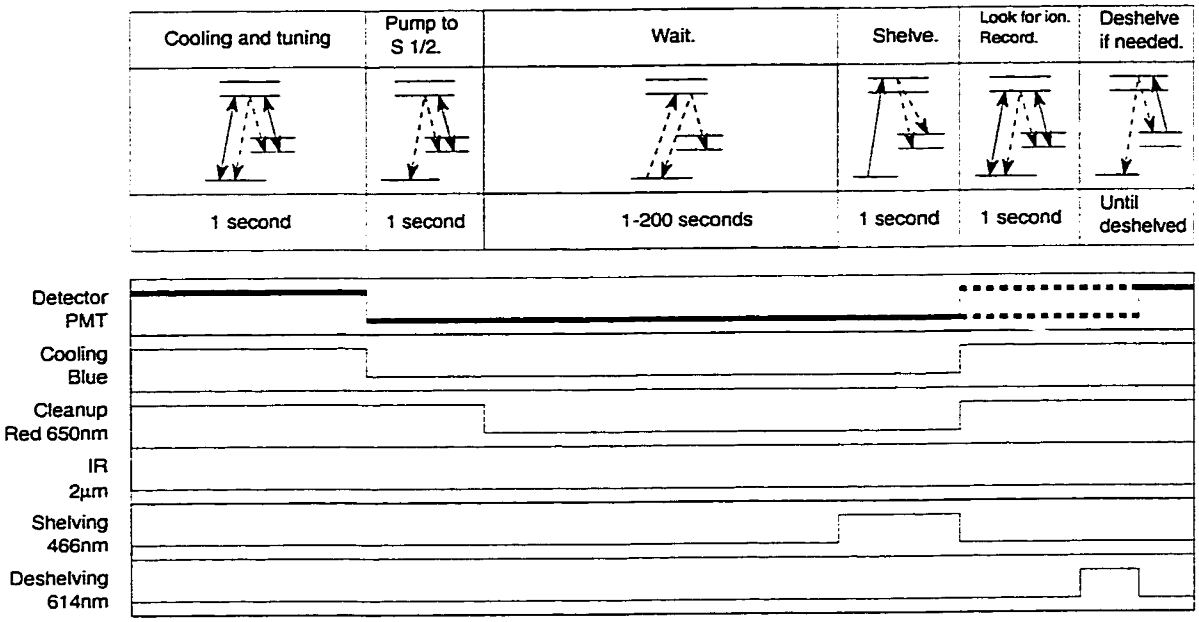

Figure 6.19: Measurement cycle used to explore the ground-state lifetime.

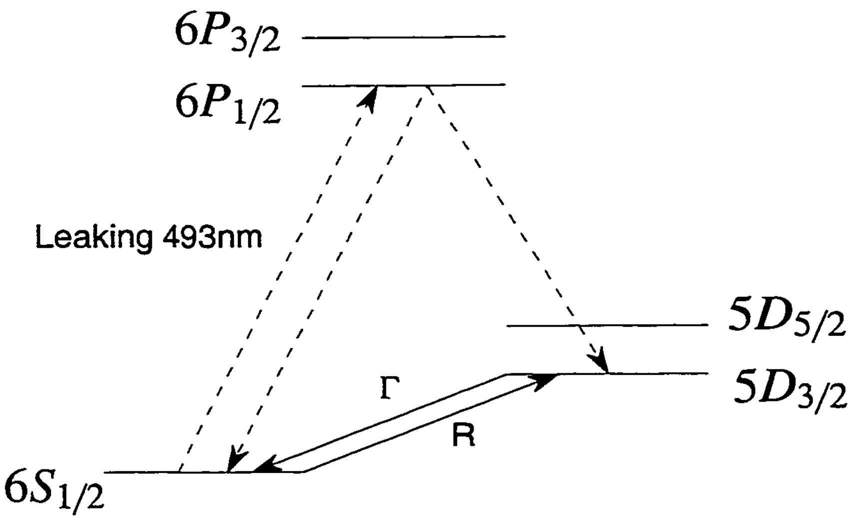

Figure 6.20: Processes affecting measurement of the ground-state lifetime. R is the transition rate between the ground and $5D_{3/2}$ states, and Γ is the natural decay rate out of the upper state. The dotted lines show the effect of resonant blue light leaking into the system.

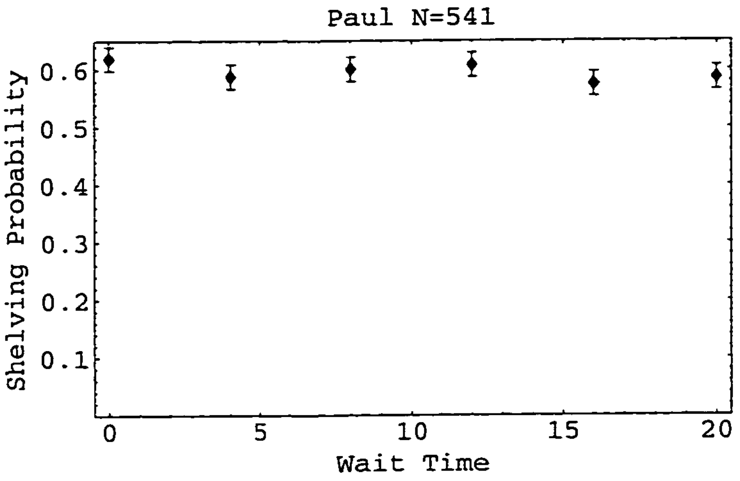

Figure 6.21: Shelving probability versus the wait time interval in seconds used to explore the ground-state lifetime. These data were taken after eliminating the leaking blue light.

If blue light is leaking into the trap during the wait time interval, the ion will be stuck in the $5D_{3/2}$ level, from which it cannot be shelved in the next step, as shown in Figure 6.20. This leaking light, which was found to exist, shortened the lifetime and decreased the maximum shelving probability. A plot of the shelving probability would quickly fall to zero after about 5 s. It was very important to completely enclose the blue-laser beam line because this light seemed to work its way into the trap after reflecting off the table.

Typical data plotted as the shelving probability versus the wait time interval is shown in Figure 6.21. These data were taken after enclosing the blue beam. The probability to be in the ground state is constant (at the maximum shelving probability) for all wait time intervals attempted.

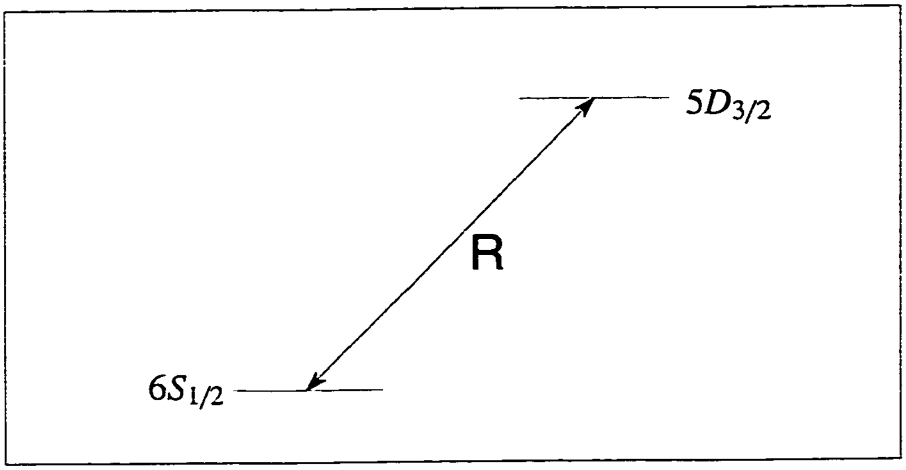

Figure 6.22: Process of driving the quadrupole transition, where R is the transition rate.

6.4 2-μm quadrupole transition

The transition between the $6S_{1/2}$ ground state and the $5D_{3/2}$ excited state is a highly forbidden electric-quadrupole transition. It is therefore expected to have a much slower transition rate than the electric-dipole allowed transitions.

Figure 6.22 contains a barium energy-level diagram and illustrates the process under consideration. The probability as a function of time to be in the ground state with unpolarized infrared laser radiation applied to the ion is given by

$$S_{1/2}(t) = e^{-Rt} + \frac{g_l}{g_l + g_u}(1 - e^{-Rt}) = \frac{1}{3} + \frac{2}{3}e^{-Rt}, \tag{6.29}$$

where R is the transition rate and g_l, g_u are the lower and upper state degeneracies.

The measurement cycle for this experiment is shown in Figure 6.23. After cooling and tuning, the ion is prepared in the ground state by blocking the blue laser just before blocking the red laser. With both cooling lasers blocked, the 2-μm laser is applied to the ion for a specified time interval between 1-30 s in an attempt to drive the quadrupole transition from the ground state to the $5D_{3/2}$ state. Then the 2-μm

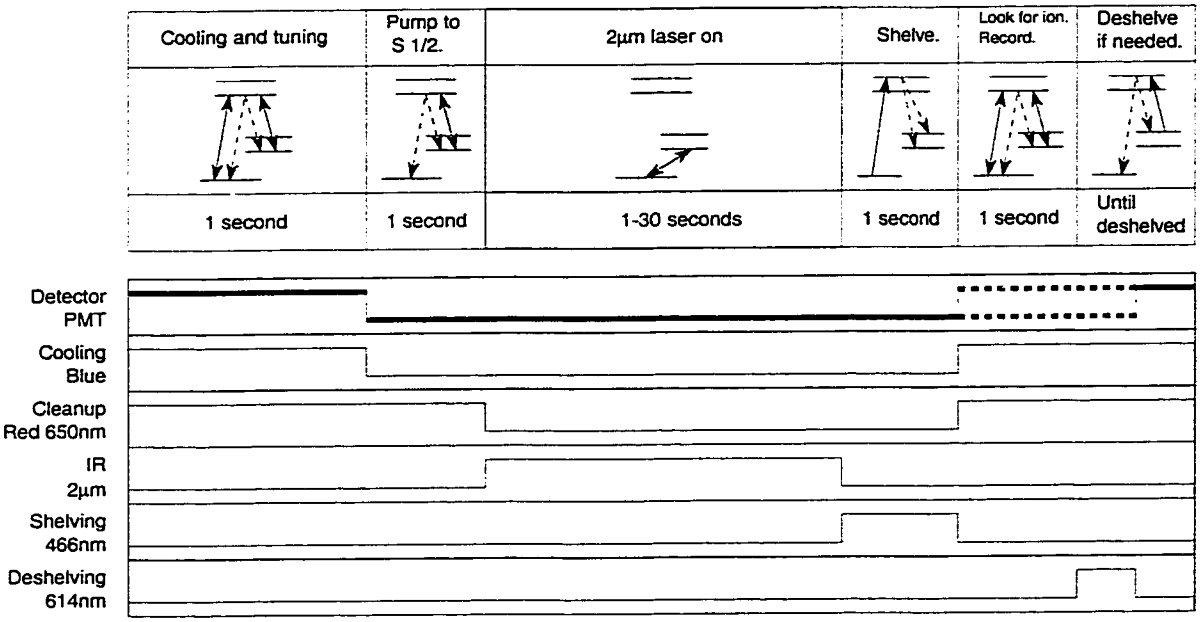

Figure 6.23: Measurement cycle used to determine the 2-μm quadrupole transition rate.

laser light is blocked, and shelving is used to verify if the transition to the $5D_{3/2}$ state was made.

The 2-μm infrared laser used in these experiments was not locked but tuned to 2.051760 μm (vacuum) with a wavemeter (no resonant reference available) that read reliably to six digits. The width of the 2-μm laser free running was measured to be less than 10 MHz. Because we were unable to precisely tune and control this laser, we broadened the laser by scanning it continuously over GHz ranges and at Hz rates that were varied. Focusing and aiming the laser into the trap was also difficult and approximate. Once we verified that we could drive this slow transition, we varied the sweep rates and ranges of the frequency and the aim and focus of the beam into the trap to search for increased transition rates. This was a tedious process, and we ended at a transition rate of $R = 4.9$ s^{-1}, which can surely be improved with

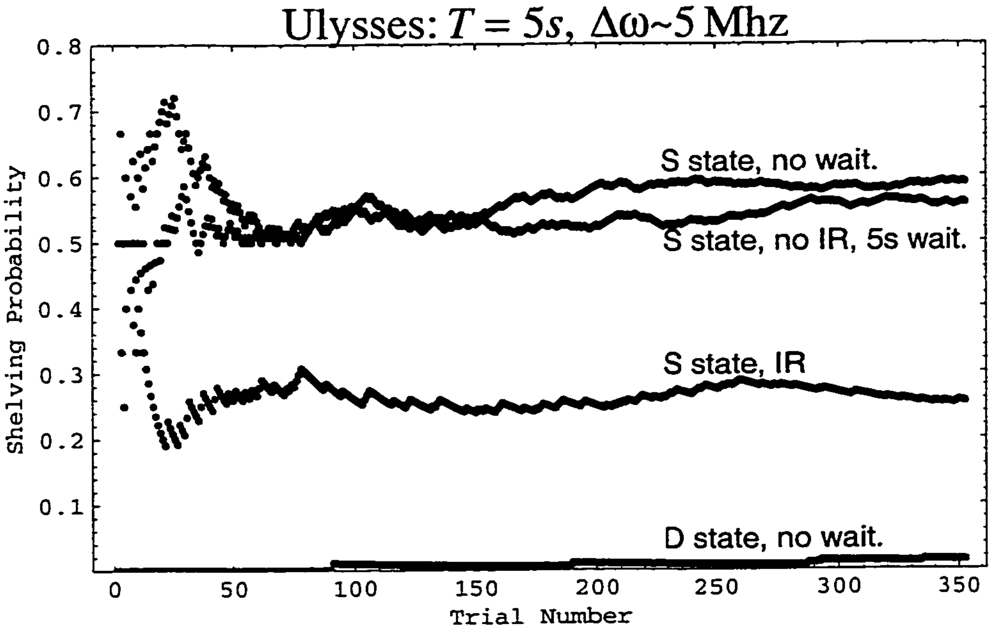

Figure 6.24: Shelving probability data used to see the quadrupole transition.

more persistence and a stable, locked, and better focused and aimed laser beam. The important point here is that we observed the quadrupole transition with our laser. There was no reason to continue attempts to boost the transition rate with this laser system because we had immediate plans to lock the laser as described in Section 4.7.2.

We can estimate theoretically the expected transition rate based on the laser power. The transition rate can be written as the product of the flux density of resonant photons $n_{\gamma \text{ flux}}$ and the transition cross section σ. The photon flux density can be written in more detail in terms of the 2-μm laser power,

$$n_{\gamma \text{ flux}} = \frac{\text{power}}{\text{area}} \frac{1}{\text{energy per } 2 - \mu\text{m photon}}. \tag{6.30}$$

Using reasonable values, we find

$$n_{\gamma \text{ flux}} \approx \frac{5 \text{ mW}}{\pi (1 \text{ mm})^2} \frac{1}{0.6 \text{ eV}} \approx 2 \times 10^{10} \frac{\text{photons}}{\mu\text{m}^2 \cdot \text{s}}. \tag{6.31}$$

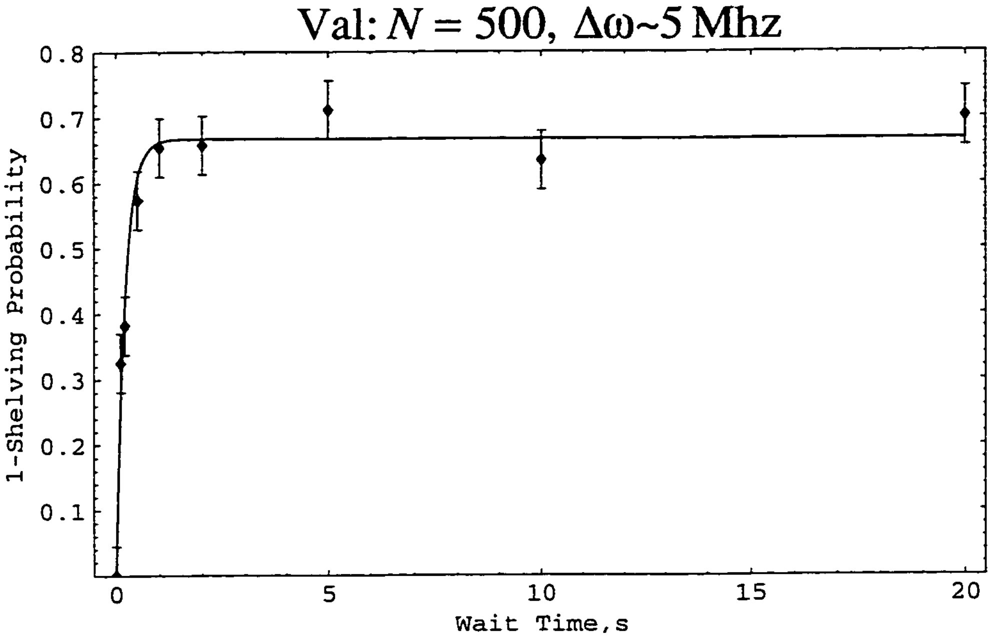

Figure 6.25: Cumulative shelving probability data for various wait time intervals used to determine the quadrupole transition rate. The result for these data is $R = 4.9\ \mathrm{s}^{-1}$.

The transition cross section can be written in terms of the transition and laser linewidths, as follows:

$$\sigma = \frac{\lambda^2}{2\pi}\frac{\Delta\nu_{\text{transition}}}{\Delta\nu_{\text{laser}}}, \tag{6.32}$$

where $\Delta\nu_{\text{transition}} = 1/(2\pi\tau_{\text{natural}})$ and the laser linewidth is taken to be the broadened value of $(2\pi)0.5$ GHz. With these values, we estimate σ to be

$$\sigma \approx \frac{(2.05\ \mu\text{m})^2}{2\pi}\frac{1/(50\ \text{s})}{(2\pi)5\ \text{MHz}} \approx 4 \times 10^{-10}\mu\text{m}^2. \tag{6.33}$$

The resulting product is an estimate of the transition rate;

$$R \approx n_{\gamma\ \text{flux}}\sigma \approx 8\ \text{s}^{-1}. \tag{6.34}$$

This result is reasonably consistent with the experimentally determined value, considering our lack of precise knowledge of the laser power and beam diameter.

6.5 Measurements in progress

Several experiments in progress at the completion of this thesis work have been completed as of this writing and others are still in progress. A few key steps necessary for the final PNC light shift measurement still remain to be explored. I list and briefly discuss these points in this section. More details will be found in the following thesis [Sch00].

6.5.1 Magnetic sublevel state selection

Optical pumping with polarized light is the conventional method used to alter the relative populations of the magnetic sublevels of a ground or metastable state from its thermal population distribution and is used to prepare the ion in specific magnetic sublevels of the ground or excited $5D$ states. These same techniques are used to detect the final spin state.

The cooling and/or clean-up laser beams are polarized using the voltage-controlled phase retarders described in Section 4.7. The voltage required to produce linearly polarized light is first roughly set by eye using a separate linear polarizer. Then a magnetic field large enough to overwhelm ambient fields is applied parallel to the laser-beam propagation direction. The voltage of the phase retarder is tuned higher than the linear setting until the ion signal dips maximally, indicating that the ion has been optically pumped out of the cooling cycle. This is one sense of circular polarization. This procedure is repeated to find the other sense of circularly polarized light at a voltage lower than the linear voltage setting. The ion signal can also be used to find more precisely the voltage setting for linear polarization. The magnetic field is applied perpendicular to the laser-beam propagation direction and the voltage is tuned for maximal optical pumping.

Imperfect polarizations and alignment between the applied magnetic field and the laser beams will limit the purity of the preparation and detection schemes. A clear difference in shelving probabilities from different spin states is the minimum necessary for a successful scheme. In general, a polarized 1.76-μm laser for direct shelving will increase the difference in shelving probabilities over the polarized lamp light used in the indirect shelving method. Use of carefully timed π pulses of 1.76-μm light will also improve these techniques.

6.5.2 Magnetic resonance experiments

Magnetic resonance techniques are used in this experiment to measure the splitting between the magnetic sublevels of the $5D$ and $6S$ states. The ion is optically pumped into one of the magnetic sublevels by polarized light, as described in the previous subsection. A radio-frequency magnetic field $\mathbf{B}_{\mathrm{RF}}$ that oscillates at an angular frequency ω_{RF} is then applied. Magnetic resonance transitions to another magnetic sublevel are driven when the frequency of this field matches the Larmor angular frequency ω_L corresponding to the energy splitting between the sublevels. If the magnitude of $\mathbf{B}_{\mathrm{RF}}$ is held constant while its frequency is swept over a range including or near ω_L, a magnetic resonance can be traced out by monitoring the spin-dependent shelving probability.

6.5.3 Spin state lifetimes

Spin state lifetimes have been measured in the $5D_{3/2}$ and $6S_{1/2}$ states. Measurement cycles are similar to those for full state lifetimes with the addition of appropriately polarized light during state preparation and detection and a weak, polarized probe beam applied just before the shelving step. Knowledge of the spin lifetimes is a more sensitive test for extraneous and fluctuating electric and magnetic fields that could couple the separated spin states. At magnetic fields of ~1 G, spin lifetimes in the $5D_{3/2}$ state are tens of seconds, as long as the $5D_{3/2}$ lifetimes. Measurements in the ground state yield at least 5 s spin lifetimes but are limited by magnetic field noise. Additional measurements at lower magnetic fields are planned.

6.5.4 Light shifts

Ordinary light shifts can be induced by intense, polarized light. The created shift between magnetic sublevels is then measured using the magnetic resonance techniques already described. Light shifts have been created and measured in the $5D$ states using a dye laser at 653 nm.

The next step is to create and measure light shifts in the ground state using the dye laser at 653 nm and then using polarized 2-μm laser light. These measurements could be used to measure the 2-μm electric field amplitude for calibration of the PNC light shift measurement. Ultimately, of course, similar techniques will be used to measure the PNC light shift.

6.5.5 Standing-wave system

The initial test of the stability of the relative position between the mirror and the ion will involve only the blue and red lasers. We shall look for evidence of pumping of the ion in the $5D_{3/2}$ state upon successful creation of a standing wave node of red light at the ion. Long-term stability of the optical node position will be studied along with effects of residual micromotion and stray fields on ion localization. Subsequent tests will utilize the 2-μm laser.

Chapter 7

CONCLUSIONS

The possibility of measuring atomic parity nonconservation in a single, trapped barium ion has been explored. I have discussed the possible accuracy range around 0.1% facilitated by the unique environment and high efficiency techniques of a single ion in an electric trap. I have outlined the possible new physics that may be revealed at this precision level, complementary to several high-energy experiments that also probe this interaction. I described the PNC observable in Ba^+ and outlined how it can be measured. I described the apparatus that was built to trap barium and to make the proposed PNC measurement. I have also discussed the techniques that have been developed to make preliminary measurements that will lead to the PNC measurement in Ba^+. I presented the results of several measurements that have established our understanding of the system and the developed techniques. I discussed several classes of anticipated systematic errors, including strategies for eliminating or minimizing them.

A second atomic PNC measurement with precision at the few tenths of a percent level would complement the 1999 Cs result that has already attained this accuracy. We are further motivated by the fact that our measurement could confirm or dispute the new physics that the Cs result appears to suggest.

BIBLIOGRAPHY

[A+86] H. Abramowicz et al. *Phys. Rev. Lett.*, 57:298, 1986.

[ABD66] A. Ashkin, G. D. Boyd, and J. M. Dziedzic. Resonant optical second harmonic generation and mixing. *IEEE J. of Quantum Electron.*, QE-2:109–124, 1966.

[B+90] A. Blondel et al. *Zeit. Phys. C*, 45:361, 1990.

[BB74a] M. A. Bouchiat and C. Bouchiat. *J. Phys. (Paris)*, 35:899–927, 1974.

[BB74b] M. A. Bouchiat and C. C. Bouchiat. Weak neutral currents in atomic physics. *Phys. Lett.*, 48B:111–114, 1974.

[BB75] M. A. Bouchiat and C. C. Bouchiat. *J. Phys. (Paris)*, 36:493–509, 1975.

[BBK+84] G. N. Birich, Yu. V. Bogdanov, S. I. Kanorskii, I. I. Sobel'man, V. N. Sorokin, I. I. Struk, and E. A. Yukov. Nonconservation of parity in atomic bismuth. *Sov. Phys. JETP*, 60:442–449, 1984.

[BDCZ93] Dmitry Budker, David DeMille, Eugene D. Commins, and Max S. Zolotorev. Investigation of nearly degenerate opposite parity states in atomic dysprosium. *Phys. Rev. Lett.*, 70:3019–3022, 1993.

[BFN+93] Norman P. Barnes, Elizabeth D. Filer, Felipe L. Naranjo, Waldo J. Rodriguez, and Milan R. Kokta. Spectroscopic and lasing properties of Ho:Tm:LuAG. *Opt. Lett.*, 18:708–710, 1993.

[BGP84] M. A. Bouchiat, J. Guena, and L. Pottier. New observation of a parity violation in cesium. *Phys. Lett.*, 134B:463–468, 1984.

[BJS90] S. A. Blundell, W. R. Johnson, and J. Saperstein. High-accuracy calculation of the $6s_{1/2} \rightarrow 7s_{1/2}$ parity-nonconserving transition in atomic cesium and implications for the Standard Model. *Phys. Rev. Lett.*, 65:1411–1414, 1990.

[BJS92] S. A. Blundell, W. R. Johnson, and J. Saperstein. *Phys. Rev. D*, 45:1602, 1992.

[Bur95] Eric A. Burt. *Demonstration of Trapped Single Laser Cooled Indium Ions.* PhD thesis, University of Washington, 1995.

[BW99] S. C. Bennett and C. E. Wieman. Measurement of the $6S \rightarrow 7S$ transition polarizability in atomic cesium and an improved test of the Standard Model. *Phys. Rev. Lett.*, 82:2484–2487, 1999.

[BZ79] L. M. Barkov and M. S. Zolotorev. Parity violation in atomic bismuth. *Phys. Lett. B*, 85:308–313, 1979.

[BZ80] L. M. Barkov and M. S. Zolotorev. Parity nonconservation in bismuth atoms and neutral weak-interaction currents. *Sov. Phys. JEPT*, 52:360–369, 1980.

[Col83a] UA1 Collaboration. Experimental observation of isolated large transverse energy electrons with associated missing energy at $\sqrt{s} = 540$ GeV. *Phys. Lett.*, 122B:103–116, 1983.

[Col83b] UA1 Collaboration. Experimental observation of lepton pairs of invariant mass around 95 GeV/c^2 at the CERN SPS Collider. *Phys. Lett.*, 126B:398–410, 1983.

[Col83c] UA2 Collaboration. Evidence for $Z^0 \rightarrow e^+e^-$ at the CERN $\bar{p}p$ Collider. *Phys. Lett.*, 129:130–140, 1983.

[Col96] SLD Collaboration. Presented by D. Su at XXVIII International Conference on High Energy Physics, Warsaw, July 25-31, 1996.

[D0] D0 Collaboration. Fermilab report FERMILAB-PUB-97-059E, March 1997.

[DBCZ94] D. DeMille, D. Budker, E. Commins, and M. Zolotorev. *Particle Astrophysics, Atomic Physics, and Gravitation*, page 339. World Scientific, Singapore, 1994.

[DC85] Persis S. Drell and Eugene D. Commins. Parity nonconservation in atomic thallium. *Phys. Rev. A*, 32:2196–2210, 1985.

[DDS89] T. W. Donnelly, J. Dubach, and Ingo Sick. Isospin dependences in parity-violating electron scattering. *Nucl. Phys. A*, 503:589–631, 1989.

[DeM95] David DeMille. Parity nonconservation in the $6s^2\ {}^1S_0 \rightarrow 6s5d^3D_1$ transition in atomic ytterbium. *Phys. Rev. Lett.*, 74:4165–4168, 1995.

[DFK86] V. A. Dzuba, V. V. Flambaum, and I. B. Khriplovich. Enhancement of P- and T-nonconserving effects in rare-earth atoms. *Z. Phys. D*, 1:243–245, 1986.

[DFS89] V. A. Dzuba, V. V. Flambaum, and O. P. Sushkov. Summation of the high orders of perturbation theory for the parity nonconserving E1-amplitude of the 6s-7s transition in the caesium atom. *Phys. Lett. A*, 141:147–153, 1989.

[DFSS87] V. A. Dzuba, V. V. Flambaum, P. G. Silvestrov, and O. P. Sushkov. Calculation of parity non-conservation in thallium. *J. Phys. B*, 20:3297–3311, 1987.

[DFSS88] V. A. Dzuba, V. V. Flambaum, P. G. Silvestrov, and O. P. Sushkov. Relativistic many-body calculations of parity nonconservation in lead and bismuth atoms. *Europhys. Lett.*, 7:413, 1988.

[DGS96] G. Degrassi, P. Gambino, and A. Sirlin. LALN e-Print Archive, hep-ph/9611363, 1996.

[Dun96] R. W. Dunford. Parity nonconservation in high-Z heliumlike ions. *Phys. Rev. A*, 54:3820–3823, 1996.

[EPBN95] N. H. Edwards, S. J. Phipp, P. E. G. Baird, and S. Nakayama. Precise measurement of parity nonconserving optical rotation in atomic thallium. *Phys. Rev. Lett.*, 74:2654–2657, 1995.

[Est89] L. Esterowitz. Diode pumped holmium, thulium and erbium lasers between 2 and 3 μm operating cw at room temperature. *SPIE*, 1104:216–224, 1989.

[FHPW61] P. A. Franken, A. E. Hill, C. W. Peters, and G. Weinreich. Generation of optical harmonics. *Phys. Rev. Lett.*, 7:118–119, 1961.

[For99] E. N. Fortson. The Seattle experiments with atomic vapors and single atomic ions. In Bernard Frois and Marie-Anne Bouchiat, editors, *Parity Violation in Atoms and Polarized Electron Scattering*, pages 244–259. World Scientific, 1999.

[FPW90] E. N. Fortson, Y. Pang, and L. Wilets. Nuclear structure effects in atomic parity nonconservation. *Phys. Rev. Lett.*, 65:2857–2860, 1990.

[Gla61] S. L. Glashow. *Nucl. Phys.*, 22:579, 1961.

[H+73] F. J. Haser et al. Observation of neutrino-like interactions without muon or electron in the Gargamelle neutrino experiment. *Phys. Lett.*, 46B:138–140, 1973.

[HAL+81] J. H. Hollister, G. R. Apperson, L. L. Lewis, T. P. Emmons, T. G. Vold, and E. N. Fortson. Measurement of parity nonconservation in atomic bismuth. *Phys. Rev. Lett.*, 46:643–646, 1981.

[HC80] T. W. Hansch and V. Couillaud. Laser frequency stabilization by polarization spectroscopy of a reflecting reference cavity. *Opt. Commun.*, 35:441–445, 1980.

[HS75] T. W. Hansch and A. C. Schawlow. Cooling of gases by laser radiation. *Opt. Commun.*, 13:68–69, 1975.

[KBKVW92] C. Knab-Bernardini, H. Knab, F. Vedel, and G. Werth. Experimental lifetime of the metastable $5D_{3/2}$ state in Ba^+. *Z. Phys. D*, 24:339–342, 1992.

[KBZ92] J. A. Keszenheimer, E. J. Balboni, and J. J. Zayhowski. Phase locking of 1.32-μm microchip lasers through the use of pump-diode modulation. *Opt. Lett.*, 17(9):649–651, 1992.

[KDS93] Grady J. Koch, John P. Deyst, and Mark E. Storm. Single-frequency lasing of monolithic Ho,Tm:YLF. *Opt. Lett.*, 18(15):1235–1237, 1993.

[Koc] Grady J. Koch. Private communication, 1997.

[KPF96] M. G. Kozlov, S. G. Porsev, and V. V. Flambaum. Manifestation of the nuclear anapole moment in the $M1$ transitions in bismuth. *J. Phys. B: At. Mol. Opt. Phys.*, 29:689–697, 1996.

[LDL$^+$] LEP Collaborations ALEPH, DELPHI, L3, OPAL, LEP Electroweak Working Group, and SLD Heavy Flavor Group. CERN report CERN-PPE/96-183. December 6, 1996.

[LS94] B. W. Lynn and P. G. H. Sandars. Electroweak radiative corrections to atomic parity non-conservation. *J. Phys. B*, 27:1469–1488, 1994.

[LY56] T. D. Lee and C. N. Yang. Question of parity conservation in weak interactions. *Phys. Rev.*, 104:254–258, 1956.

[M$^+$98] K. S. McFarland et al. A precision measurement of electroweak parameters in neutrino-nucleon scattering. *Eur. Phys. J.*, C1:509–513, 1998.

[Maj62] Fouad George Major. *The Orientation of Electrodynamically Contained He^4 Ions.* PhD thesis, University of Washington, 1962.

[Mar] Peter Markowitz. Private communication, 1998.

[Mar97] Peter Markowitz. Prospects for a measurement of the neutron radius. Second International Symposium on Symmetries in Subatomic Physics, 1997.

[MR90] William J. Marciano and Jonathon L. Rosner. Atomic parity violation as a probe of new physics. *Phys. Rev. Lett.*, 65:2963–2966, 1990.

[MR92] William J. Marciano and Jonathon L. Rosner. *Phys. Rev. Lett.*, 68:898E, 1992.

[MSD95] Swati Malhotra, Angom D. Singh, and B. P. Das. Relativistic configuration-interaction analysis of parity nonconservation in Ba^+. *Phys. Rev. A*, 51:2665–2667, 1995.

[MSH78] W. C. Martin, R. Salubas, and L. Hagan. *Atomic Energy Levels–The Rare Earth Elements*. National Bureau of Standards, Washington D.C., 1978.

[MVM$^+$93] D. M. Meekhof, P. Vetter, P. K. Majumder, S. K. Lamoreaux, and E. N. Fortson. High-precision measurement of parity nonconserving optical rotation in atomic lead. *Phys. Rev. Lett.*, 71:3442–3445, 1993.

[MZW$^+$91] M. J. D. Macpherson, K. P. Zetie, R. B. Warrington, D. N. Stacey, and J. P. Hoare. Precise measurement of parity nonconserving optical rotation at 876 nm in atomic bismuth. *Phys. Rev. Lett.*, 67:2784–2787, 1991.

[Nag] Warren Nagourney. Private communication, 1999.

[Nag98] Warren Nagourney. Artwork taken from a poster by the author, 1998.

[NHTD80] W. Neuhauser, M. Hohenstatt, P. E. Toschek, and H. Dehmelt. Localized visible Ba^+ mono-ion oscillator. *Phys. Rev. A*, 22:1137–1140, 1980.

[PEBN96] S. J. Phipp, N. H. Edwards, P. E. G. Baird, and S. Nakayama. A measurement of parity non-conserving optical rotation in atomic lead. *J. Phys. B*, 29:1861–1869, 1996.

[Pes] Michael E. Peskin. Beyond the Standard Model. To appear in the proceedings of the 1996 European School of High-Energy Physics.

[PFW92] S. J. Pollock, E. N. Fortson, and L. Wilets. Atomic parity nonconservation: Electroweak parameters and nuclear structure. *Phys. Rev. C*, 46:2587–2600, 1992.

[PT92] Michael E. Peskin and Tatsu Takeuchi. Estimation of oblique electroweak corrections. *Phys. Rev. D*, 46:381–409, 1992.

[RM97] M. J. Ramsey-Musolf. New physics at low-energy PV. In Roger Carlini and Michael J. Ramsey-Musolf, editors, *Future Directions in Parity Violation, Fifth Annual JLAB (CEBAF)/INT Workshop*, pages 442–449. University of Washington Institute for Nuclear Theory, 1997.

[Ros96] Jonathon L. Rosner. Impact of atomic parity violation experiments on precision electroweak physics. *Phys. Rev. D*, 53:2724–2728, 1996.

[Ros98] Jonathon L. Rosner. New developments in precision electroweak physics. *Comments on Nucl. Part. Phys.*, 22:205–221, 1998.

[Ros99] Jonathon L. Rosner. Atomic parity violation and precision electroweak physics - An updated analysis. LALN e-Print Archive hep-ph and submitted to *Phys. Rev. D.*, 1999.

[Sal68] A. Salam. In N. Svartholm, editor, *Proceedings of the Eighth Nobel Symposium on Elementary Particle Theory*, page 367, Stockholm, 1968. Almqvist and Wicksell, Publishers.

[San90] P. G. H. Sandars. A reappraisal of atomic parity non-conservation. *J. Phys. B*, 23:L655–L658, 1990.

[Sch00] Mike Schacht. PhD thesis, University of Washington, 2000.

[SDJ98] M. S. Safronova, A. Derevianko, and W. R. Johnson. Relativistic many-body calculations of energy levels, hyperfine constants, and transition rates for atoms and ions with one valence electron. In *Sixteenth International Conference on Atomic Physics*, pages 176–177, 1998.

[Sto] Mark E. Storm. Private communication, 1997.

[TDHP+97] R. C. Thompson, K. Dholakia, J-L. Hernandez-Pozos, G. Zs. K. Horvath, J. Rink, and D. M. Segal. Spectroscopy and quantum optics with ion traps. *Physica Scripta*, T72:24–33, 1997.

[Tip] P. Tipton. Plenary talk. XXVIII International Conference on High Energy Physics, Warsaw, July 25-31, 1996.

[VMM+95] P. A. Vetter, D. M. Meekhof, P. K. Majumder, S. K. Lamoreaux, and E. N. Fortson. Precise test of electroweak theory from a new measurement of parity nonconservation in atomic thallium. *Phys. Rev. Lett.*, 74:2658–2661, 1995.

[WAH⁺57] C. S. Wu, E. Ambler, R. W. Hayward, D. D. Hoppes, and R. P. Hudson. Experimental test of parity conservation in beta decay. *Phys. Rev.*, 105:1413–1415, 1957.

[WBC⁺97] C. S. Wood, S. C. Bennett, D. Cho, B. P. Masterson, J. L. Roberts, C. E. Tanner, and C. E. Wieman. Measurement of parity nonconservation and an anapole moment in cesium. *Science*, 275:1759–1763, 1997.

[WD75] D. J. Wineland and H. G. Dehmelt. Proposed $10^{14}\delta\nu < \nu$ laser fluorescence spectroscopy on Tl^+ mono-ion oscillator III. *Bull. Am. Phys. Soc.*, 20:637, 1975.

[Wei67] Steven Weinberg. A model of leptons. *Phys. Rev. Lett.*, 19:1264–1266, 1967.

[Wer85] G. Werth. Trapped ions. *Contemp. Phys.*, 26(3):241–256, 1985.

[WI79] D. J. Wineland and W. Itano. *Phys. Rev. A*, 20:1521, 1979.

[WTS93] R. B. Warrington, C. D. Thompson, and D. N. Stacey. A new measurement of parity-non-conserving optical rotation at 648 nm in atomic bismuth. *Europhys. Lett.*, 24:641–646, 1993.

[YN95] N. Yu and W. Nagourney. Analysis of Paul-Straubel trap and its variations. *J. Appl. Phys.*, 77:3623–3630, 1995.

[YND91] N. Yu, W. Nagourney, and H. Dehmelt. Demonstration of new Paul-Straubel trap for trapping single ions. *J. Appl. Phys.*, 69:3779–381, 1991.

[YND97] N. Yu, W. Nagourney, and H. Dehmelt. Radiative lifetime measurement of the Ba^+ metastable $D_{3/2}$ state. *Phys. Rev. Lett.*, 78:4898–4901, 1997.

[ZB97] M. Zolotorev and D. Budker. Parity nonconservation in relativistic hydrogenic ions. *Phys. Rev. Lett.*, 78:4717–4720, 1997.

[Zel59] Ya. B. Zel'dovich. Parity nonconservation in the first order in the weak-interaction constant in electron scattering and other effects. *Sov. Phys. JETP*, 9:682L–683L, 1959.

[ZK92] J. J. Zayhowski and J. A. Keszenheimer. Frequency tuning of microchip lasers using pump-power modulation. *IEEE J. Quantum Electron.*, 28(4):1118–1122, 1992.

Appendix A

SCHEMATICS

This appendix contains a couple of the circuit schematics designed for use in the barium ion trap.

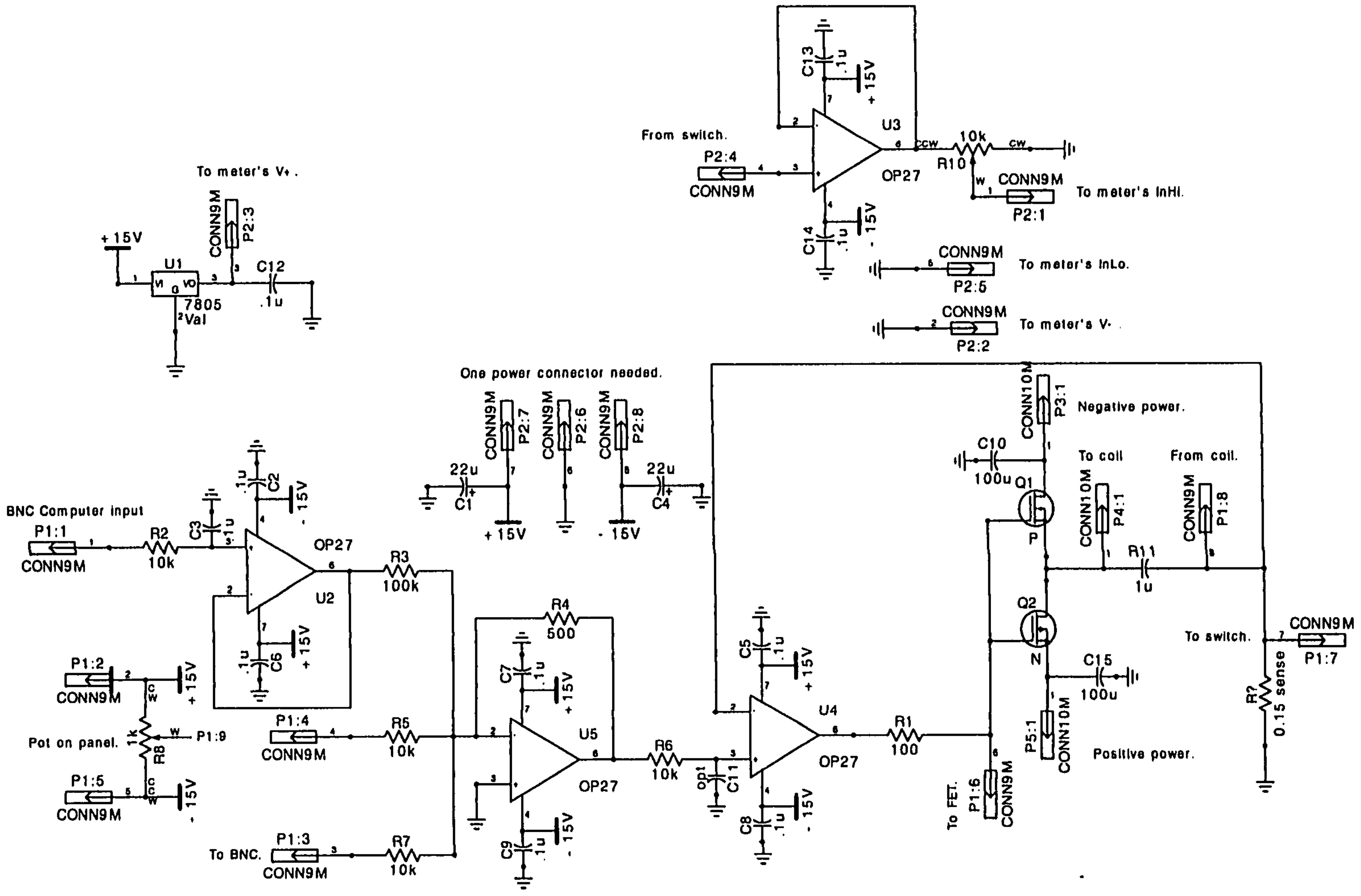

Figure A.1: Schematic diagram of the circuit used for the regulated bipolar high current supply used to drive the magnetic field coils. Grounding is very important to keep noise out of the current output. Substantial heat sinking for the MOSFETs is also important.

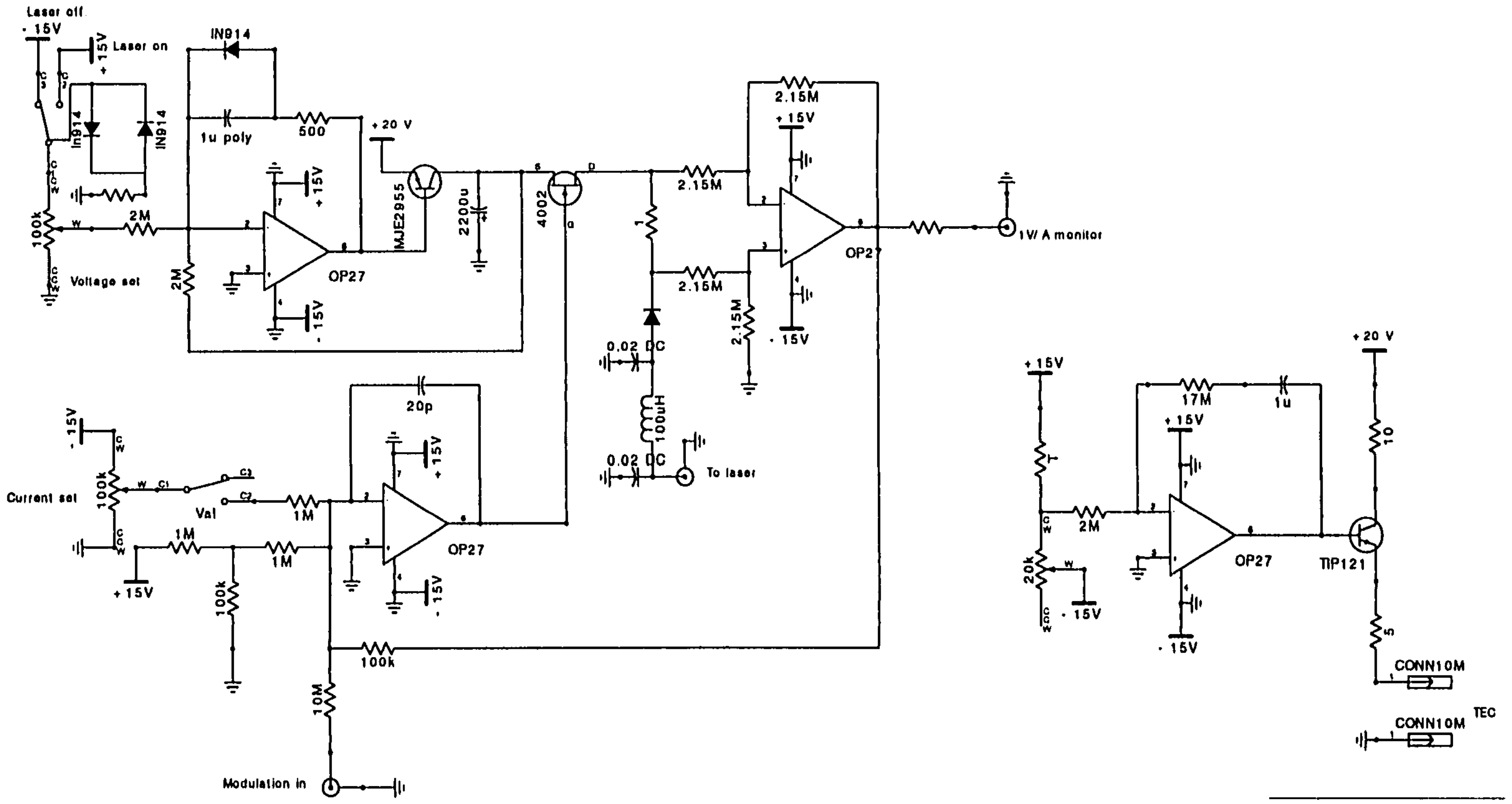

Figure A.2: Circuit schematic of the 2-μm pump and red laser controllers. This circuit was designed by Steve Lamoreaux.

VITA

Kristi Rae Gayle Hendrickson was born June 4, 1969, in Fargo, North Dakota, to Marianne Margaret and Herman Robert Hendrickson. She attended high school in Sauk Centre, Minnesota, graduating as the salutatorian and vice president of the 1987 class. She earned her bachelor of arts degree in physics from Lawrence University in Appleton, Wisconsin, in 1991, graduating cum laude. She began graduate study at the University of Washington in Seattle, Washington, in 1991, completing her Master of Science degree in 1994 and her Ph.D. in 1999. She is currently assistant professor of physics at the University of Puget Sound in Tacoma, Washington.